Spring 2024

Dynamic Soil-Structure Response and Failure of Wood Utility Poles Under Hurricane-Force Wind and Non-Linear Cable Loads

Ramani Ayakannu
Old Dominion University, RAMANI.AYAKANNU@GMAIL.COM

DYNAMIC SOIL-STRUCTURE RESPONSE AND FAILURE OF WOOD UTILITY POLES UNDER HURRICANE-FORCE WIND AND NON-LINEAR CABLE LOADS

by

Ramani Ayakannu, MS, PE

B. Tech (Civil) December 1983, National Institute of Technology, Warangal, India
M.S (Civil) December 1989, South Dakota School of Mines and Technology, South Dakota.

A Dissertation Submitted to the Faculty of
Old Dominion University in Partial Fulfillment of the
Requirements for the Degree of

DOCTOR OF PHILOSOPHY

CIVIL and ENVIRONMENTAL ENGINEERING

OLD DOMINION UNIVERSITY
May 2024

Approved by:

Zia Razzaq (Director)

Shahin N. Ameri (Member)

Mojtaba B. Sirjani Member)

Herish Hussein (Member)

ABSTRACT

DYNAMIC SOIL-STRUCTURE RESPONSE AND FAILURE OF WOOD UTILITY POLES UNDER HURRICANE-FORCE WIND AND NON-LINEAR CABLE LOADS

Ramani Ayakannu, MS, PE
Old Dominion University, 2024
Director: Dr. Zia Razzaq

This dissertation presents the outcome of a study of the dynamic soil-structure interaction response of tapered wood utility poles embedded in various foundation soils subject to quasi-static and dynamic wind loads. The study includes the effects of nonlinear soil behavior with varying quantities of moisture and nonlinear cable tension loads on a class H1 wood pole. The natural frequency response of the pole is determined using a finite element formulation. The dynamic response in the presence of wind-induced forcing function is studied using a SAP2000 finite element scheme with wind speeds up to 220 mph. The natural frequency of the wood pole increased nine-fold with a tuned mass damper with mass and stiffness ratios of 0.15 and 10, respectively. Wood pole breakage occurs when the wind speed is more than 160 mph in the plane of the cable for clayey soils if the embedment depth is more than 5.5 ft. pole breakage does not occur for wind speeds up to 120 mph in sandy soils. The theoretical models formulated predict the critical wind speeds and embedment depths beyond which catastrophic pole rupture and excessive ground displacements occur. Results from a one-fifth scale experimental fixed base test model of a class H1 pole provided the natural frequency and damping ratio. The experimental results agreed well with those predicted using the finite element analysis. The current wood pole design standards based on static analysis do not consider the dynamic response of the poles, causing pole failures and service disruptions.

ACKNOWLEDGMENTS

First, I would like to thank my mentor and guide, Dr. Zia Razzaq, whose support and encouragement were crucial motivators for my progress toward my aspirations to complete the PhD program. This journey of mine would not be possible without my wife, Dr. Shyama Nair, whose support, patience, and tolerance through this process made it easier for me to balance my time between regular office work, family, and this Ph.D. program. Finally, thanks to my mom, who made my journey possible.

NOMENCLATURE

a	Acceleration
$A(x)$	Cross Sectional Area
$A_{E,Z}$	Elastic Modulus of Soil
ASCE	American Society Of Civil Engineers
C	Element or System Damping Matrix
DSSIR	Dynamic Soil Structure Interaction Response
F	Element of System Forcing Function Matrix
$f(t)$	Forcing Function
FEA	Finite Element Analysis
FRP	Fiber Reinforced Poly
g	Gravitational Constant
h	Finite Element length or size
$I(x)$	Cross Sectional Area
K	Element or System Stiffness Matrix
$m(x)$	Mass Per Unit Length
mph	Miles Per Hour
pcf	Pounds Per Cubic Feet
R	Radius of Curvature
s, S	Length of Cable
T	Cable Tension
T_0	Initial Cable Tension
TMD	Tuned Mass Damper

v	Velocity
w	Weight Of Cable
α	Mass Proportional Constant
β	Stiffness Proportional Constant
γ_{soil}	Density Of Soil
γ_{wood}	Density Of Wood Species
ξ	Damping Co-efficient for element or System
ϕ	Curvature of a given function
ω	Circular Frequency of Element or System

TABLE OF CONTENTS

LIST OF TABLES

LIST OF FIGURES

CHAPTER I

1 INTRODUCTION

1.1 Background

Strong winds and hurricanes in various parts of the world have resulted in the collapse of utility poles, disrupting electrical and communication distribution systems and creating hazardous conditions for the public. This study is prompted by the severe damages observed to utility structures, mainly wood utility poles, during Hurricane Maria in Puerto Rico on September 19, 2017, and Hurricane Katrina that hit New Orleans in 2005. The death toll due to Hurricane Maria and Katrina was estimated at 3000, and 1200 deaths, respectively.

The damage to the utilities resulted in several weeks of electricity service interruptions. There has been a renewed interest in studying the failure of utility structures due to hurricane-force winds and water damage and improving on the current design standards and codes to minimize these failures. The failure of wood utility poles is more common compared to steel and concrete poles.

To capture the predicted soil-structure interaction dynamic response of the pole, a SAP2000 dynamic finite element model is created. The foundation soil stiffness is characterized using a series of ‘soil springs’ below the ground level with damping. The properties of the soil springs vary with the properties of foundation soils and depths. Three types of foundation soils are considered: sandy, clayey, and granite (rock).

The experimental and SAP2000 results are validated compared to the results from a MATLAB code.

1.2 Literature Review

Much research has been conducted to understand better the behavior of poles embedded in soil and subject to wind loading. Some of the relevant research is listed in this section.

Wood pole design has been evolving over the last 80 years. Brent et al. [1] studied this evolution in the design philosophy in their journal publication “Are wood poles getting weaker?”. This paper follows the evolution of wood pole design over the last 80 years, and an example is used to demonstrate how the relative safety factor has increased. A brief review of the changes in the National Electrical Safety Code [2] strength requirements from 1927 to 2007 shows how little it has changed. Technological advances in calculators, computers, and computer software make it possible to analyze complex problems. Once simplified to facilitate computation, equations are expanded to include previously ignored components. However, the NESC has yet to adopt and incorporate these changes, resulting in more conservative designs.

Utility poles are made of other materials like Fiber-Reinforced Polymer (FRP), steel, or concrete [3-5]. The earliest FRP poles were manufactured and installed in 1954 by Gar Wood Industries [6]. The advantages and disadvantages of steel poles were studied by B. Lacoursiere [7]. In the publication “Steel Utility Poles: Advantages and Disadvantages,” Lacoursiere demonstrated that steel poles have more predictable behavior and effectively withstand design forces.

Utility poles are typically subjected to Wind, cables, and ground motion lateral loads. However, the buckling strength is an important mechanical property. This was investigated by A. B. Peabody and J.W.Wekezer [8] in the journal “Buckling strength of wood poles using Finite Element.” The Eigen values were solved for various geometric and boundary conditions. It was found that there was good agreement with Euler’s formula.

An essential dynamic property of wood poles is the damping ratio. Farhang Ostadan, Nan Deng, and Jose M. Roesset [9] described the method of estimating the damping rations in their publication “Estimating Total System Damping for Soil-Structure Interaction Systems.” The damping ratio is a complex interplay of materials damping and radiation damping in a dynamic solution. Using three methods, they studied the damping ratios for 5%, 10%, 15%, and 20%. The three methods used were half-bandwidth, the inverse of the peak, and the damping ratio method. It was found that the response from an impulse load applied to the Soil Structure Interaction (SSI) model yielded an accurate estimate of the system damping.

The Substation design guide standard, ASCE 113, provides guidelines for the design of structures within an electric substation. A guide to using the standard was provided by Leon Kemper [10] titled “ASCE Guide for Design of Substation Structures”. In this article, the author outlines the current recommended practices used by engineers in the USA. However, dynamic soil structure interaction response (DSSIR) is only referenced as optional but not mandated.

ASCE Manuals and Reports on Engineering Practice No. 141, titled “Wood Pole Structures for Electrical Transmission Line” [11], is the prevailing recommended practice

design guide for designing wood utility poles. This manual provides recommended design parameters that engineers are currently using. Static analysis is extensively promoted with design tables and recommended allowable stress values. Soil Structure Interaction is referenced as an advanced method of analysis and accepted as an alternate method of analysis and design. Other important design parameters, such as the influence of the moisture content on the soil spring constants, are not adequately emphasized.

The National Electric Safety Code [7] [12] provides guidelines for the safety design and supporting structures of all electrical equipment. The code covers public and private sites, including homes, buildings and structures, power generation, and industrial substations. Public safety through design was the primary goal of this code.

The age of the wood specimen affects its physical and mechanical properties. Shafieezadeh et al. [13] studied the effect of age on the fragility curves of utility poles that rely on age-dependent probabilistic capacity models and wind-induced demand models. This study shows that the decay process in wood may increase the fragility of the poles significantly and would be a significant component in the risk assessment of power grid and distribution networks against hurricanes and strong winds.

The seismic response of wood utility poles in seismically active areas needs further studies and research. Siringoringo et al. [14] studied the seismic performance of light poles on elevated highway bridges. They studied the effect of the bridge's natural frequency on the amplification of the existing light poles. The study found that response amplification occurred when the bridge's natural frequency was within the light pole's fundamental frequency.

Poles are classified based on the ANSI 05.1-2022 standard. Additional information on the poles shown is included in Appendix 6.7. The tables in Appendix 6.7 have information on the physical dimensions, tip diameter, base diameter, estimated tip load, base bending moment, and embed depths.

The North American Wood Pole Council is the governing body that provides guidelines for standardizing wood pole design. The recommended fiber strengths and Modulus of Elasticity are listed in Technical Bulletin No. 18-D-203 [15]. Wood Pole design considerations, procedures, and guidelines are provided in Technical Bulletin No. 17-D-202 [16]. The recommended wood pole design methodology is a fundamental static analysis of the pole for wind and cable tensions. The Soil Structure Interaction (SS1) is generally not considered.

A utility wood pole and soil interaction is a complex three-dimensional problem. The methodology to characterize the interaction between soil and an embedded pole titled Modelling Soil Behavior With Simple Springs, Part 1 and Part 2, is presented by Bohnhoff [17]. The method proposed by Bohnhoff is adopted to compute the soil stiffnesses.

Vortex-induced vibration is a complex phenomenon that involves the interaction of wind turbulence and the structures. This phenomenon is observed in cantilever-type structures such as transmission poles and utility structures. Quarib [18] presented his findings from a three-phase dead-end structure study. The Strouhal and Reynolds numbers for fluid flow around a structural element are important parameters that will govern the resonance response of a cantilever-type structure. The critical velocity of the wind can be calculated based on the Strouhal number, the natural frequency of the structure, the

hydraulic diameter, and the Reynolds number. The study assumed that the poles are fixed at the base and does not include the effect of the soil structure interaction on the dynamic response.

Vortex-induced vibration occurs in a wide range of transmission line structures. Daryl Boggs [19] in his publication titled " Challenges in Design and Mitigation of Wind-induced Vibration for Slender Steel Pole Transmission Structures," studied several types of electrical transmission line structures and considered several types of mitigation methods, including increasing the stiffness, filling the inside of the steel structures with sand, or weak slurry, the addition of tuned mass dampers, and spoiling of vortices using vanes or helical strakes. Daryl Boggs also emphasized the need to consider fatigue and dynamic analysis due to the many cyclic loads an electric transmission line structure is subjected to.

Various types of foundations are provided for electric transmission line structures. These can be direct embedment of the structures, as in the care of cantilever poles, or conventional foundations such as spread footings or piles foundations. Kulhawy presented the various types of foundations used for electric transmission line structures, and Hirany in the publication titles "Foundation Engineering for Transmission Line Structures" [20]. A general discussion of the design of the foundations is outlined in this presentation. The foundation loads from the electric transmission line structure is obtained by analyzing the structure with a fixed a fixed base. The reactions at the base are used to design the appropriate foundations.

The Modulus of Elasticity of wood is an import factor that affects the performance of the wood utility poles. There are many wood species used as wood utility poles. The North American Wood Pole Council [21] published a guideline for the mean values of the modulus of elasticity of various wood species based on numerous research and experimental data. The modulus of elasticity recommended in [21] are mean values and hence have a an upper and lower bound values.

A guideline on the loading of an electric transmission line structure is given in the "Guidelines for Electrical Transmission Line Structure" [22]. This standard provides general information on the loads acting on an electric transmission line structure. Various types of loads, such as wind, cable, ice, and earthquake, are presented in the standard. Appendix G of this standard provides information on force coefficients on pole structures based on wind tunnel test data.

Much research has been done to predict the embedment depth of the poles in various types of soil. Many engineers use the "10% of length of pole + 2 feet" as a general practice for sandy and clayey soils. This method is often called ROT, that is, Rule of Thumb. An improved method is proposed by Gajan and McNames [23] in their publication titled "Improved Design of Embedment Depths for Transmission Pole Foundations Subject to Lateral Loading." Broms and Flemming et al. suggested the passive earth pressure method to compute the embedment depths for classes H1, H2, and H3. They considered short and long piles in the study. Short piles are those with a ratio embedment depth to diameter greater than 10. The proposed methods are compared with PLS-Caisson software and the ROT method. The study found that the embedment depths using the ROT method

overestimated the embedment depths by ± 60%. The improved method agreed well with PLS-Caisson software. The lateral loads considered are static loads applied at the top of the pole. No dynamic loads were considered in this study.

Based on the literature reviews, the proposed research has not previously been published in the literature.

1.3 Problem Statement

Presented herein is the study of the Dynamic Soil Structure Interaction Response (DSSIR) of Wood Utility Poles embedded in sandy, clayey soils and rock subjected to static and dynamic wind loads, including the effects of cables at the top of the pole. The dynamic response of the wood poles subject to time history wind loads applied to the poles at resonance frequencies is also studied.

The test specimen's stiffness, Young's Modulus (E), damping ratio, and natural frequencies are obtained experimentally. The test specimen's natural frequency is compared to the theoretically computed natural frequencies for validation.

A $1/5^{th}$ scale test pole of a class H1 wood utility pole is used for the experimentation. The test poles are 4ft 0in and 6ft 0 inch long. The top and bottom diameters of the class H1 are 8.7 inches and 14.1 inches, respectively. The test pole's scaled top and base diameters are approximately 1-1/2 and 2-1/2 inches, respectively.

1.3.1 Effect of Cable Force on Poles

Cable elements at the top of the poles have the following effect on the response of the pole:

- It reduces the natural frequencies of the Pole-Cable system. The reduction in natural frequencies is due to the non-linear load-displacement characteristics and mass of the cable.
- The displacements at the top of the pole in the cable forces' positive and negative directions are different and non-linear. The cable tension increases with displacement along the negative direction and decreases with displacements in the positive direction. An example of the non-linear behavior of the cable is shown in Figure 2-5

A sketch of a wood utility pole with a cable is shown in Figure 1-1, and Figure 1-2. The nodes and nodal springs for pole embedment in the soil are shown in Figure 1-3.

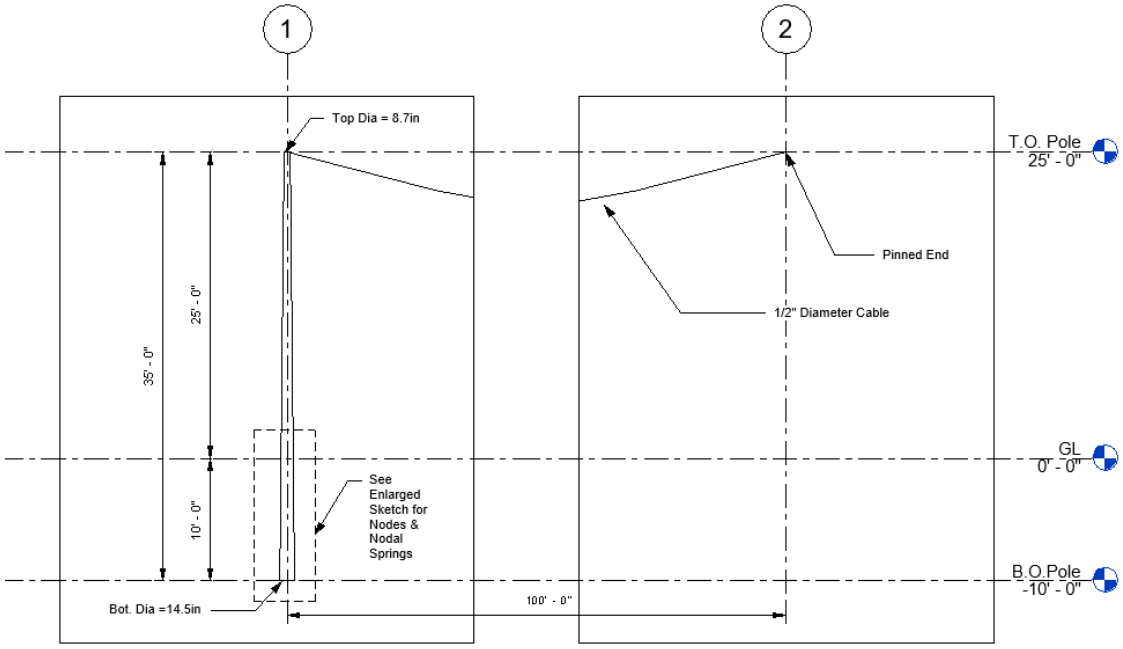

Figure 1-1. Class H1 Wood Pole with Cable

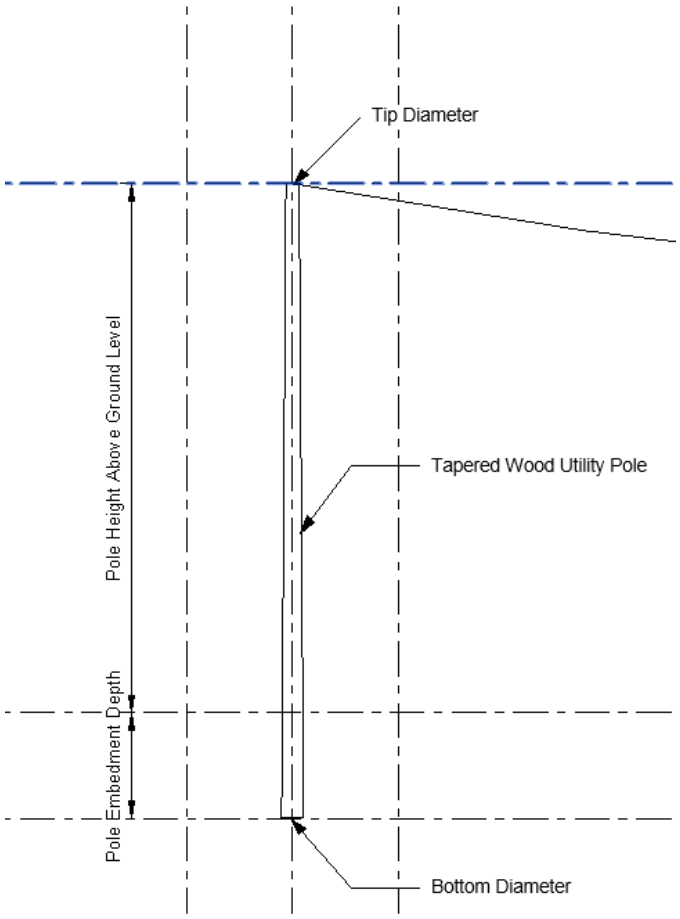

Figure 1-2. Enlarged View of Class H1 Wood Utility Pole

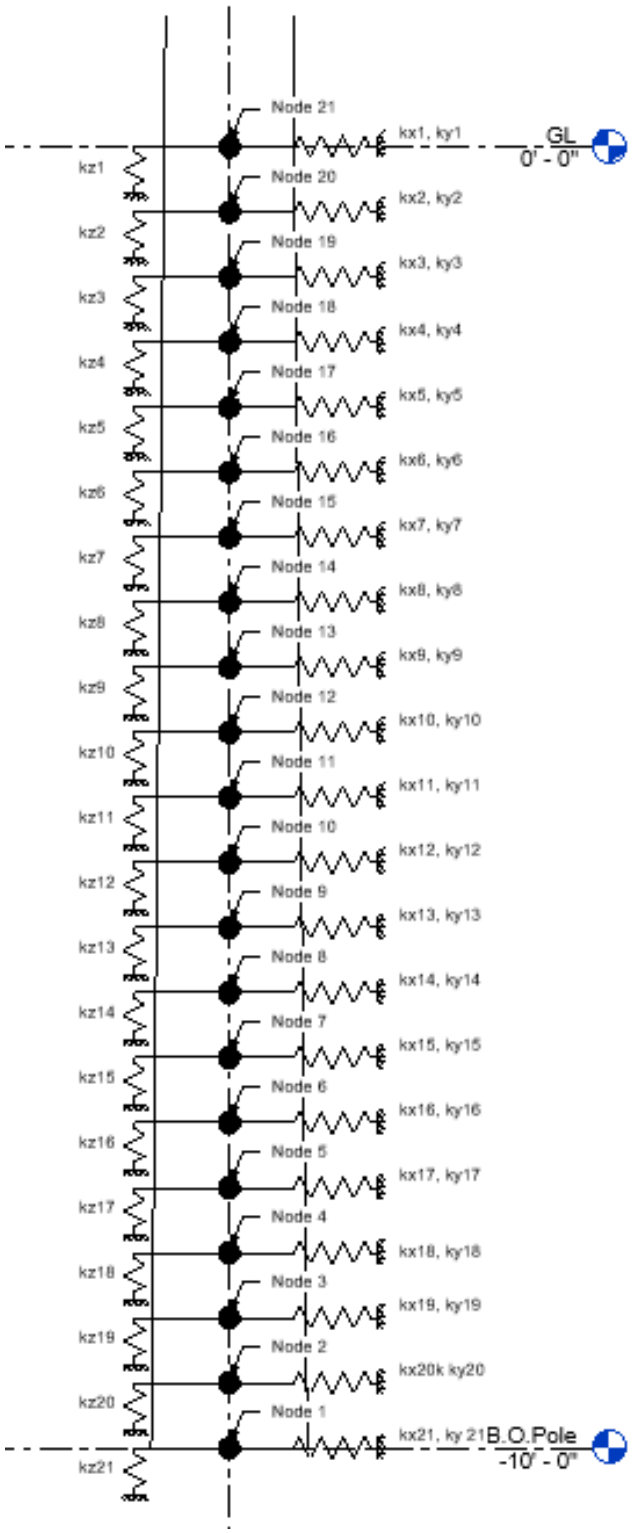

Figure 1-3. Nodes and Nodal Spring Definitions for Class H1 Wood Pole

A nodal spacing of 6 inches was selected to capture the soil behavior. The nodal springs represent the load-displacement characteristics of the soil in the X-, Y-, and Z-directions at a specified depth. The X-direction is the axis along the length of the spring element. The load-displacement characteristics can be linear or non-linear. Linear soil springs are used to study the dynamic response of the test and class H1 poles. Prediction of pole failures based on the ground and pole tip displacements are studied using non-linear springs.

1.3.2 Soil Structure Interaction

Soil Structure Interaction, or SSI, is the phenomenon by which a structure's behavior is influenced by the nature of the soil in which the structure is embedded. Soil Structure Interaction has two primary effects on the response of a structural system, namely:

- The structure’s dynamic response is altered. Since the stiffness of the soil is generally smaller than the structure, the natural frequency reduces. The dynamic responses of wood poles with and without cables in various types of soils (Sandy, Clayey, and rock) are the primary focus of this study.
- There is an increase in the system damping from the effects of the soil. The impact of the soil damping is not part of this study.

1.3.3 Effect of Moisture on the Soil Stiffness

Moisture in sandy and clayey soils reduces the soil's stiffness properties. Generally, rock does not absorb water; hence, its stiffness is unaltered. This study used 15%, 30%,

50%, and 75% soil stiffness reductions to study the dynamic responses. Site-specific geotechnical investigations will provide in-situ soil parameters to calculate soil stiffness and stiffness reduction rates due to moisture. Sandy and clayey soils with high seasonable water tables or rain variations will see significant variations in soil stiffness. Rock generally does not absorb moisture; hence, stiffness reductions are not considered in this study.

The main components of the proposed research involve:

1. Test frame to support the test poles, as shown in **Error! Reference source not found.**.
    a. Accelerometers are mounted at the top of the test poles.
2. Accelerometers at the top of the pole record the data on a Personal Computer. The accelerations at the top of the test poles are measured as described in section 2.1.
3. Compute the test poles' dynamic properties (damping ratio, stiffness, and natural frequencies) from the measured tests.
4. Compute the test specimen's Young's Modulus (E) value by conducting a load displacement experiment.
5. Develop a Finite Element model for the mass, stiffness matrix, damping, forcing function, and soil springs matrices by solving the Fourth Order differential equation of motion, including the soil's effect.
6. Determine the theoretical dynamic properties of the test pole using:
    a. SAP2000 Structural Analysis Software. SAP2000 uses the lumped mass approach.
    b. MATLAB Code using consistent mass and stiffness matrices.

7. Study the experimentally and theoretically obtained dynamic properties of the test poles.
8. Study the theoretical dynamic response of a class H1 pole embedded in clayey, sandy soils and rock at various depths, subject to static and dynamic wind loads, including cable tension effects. The cable used in the study is a ½" diameter, 100 ft long cable attached to the top of the poles and pinned at the far end.
9. Study the dynamic response of the class H1 pole at resonance conditions.
10. Study the effect of a Tuned Mass Damper mounted at the top of the class H1 pole.

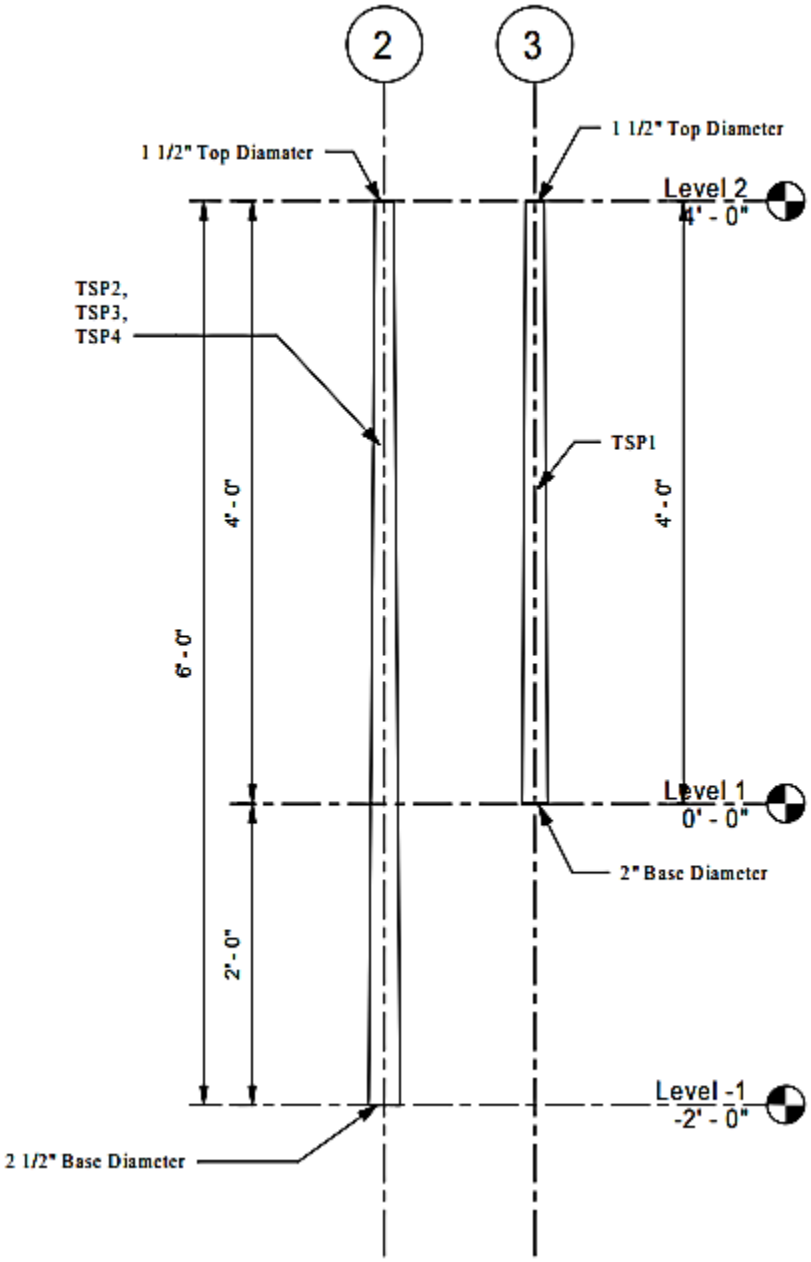

Figure 1-4. Test Pole Dimensions

1.4 Objective and Scope

The primary objective of the proposed study is to investigate the Dynamic Soil Structure Interaction Response (DSSIR) of wood utility poles embedded in sandy and clayey soils and rock subject to wind loads in the presence of cable forces at the top of the pole. The natural frequency response of the poles embedded in soil are then compared with a fixed base. The dynamic response at resonance conditions is also investigated. The static and dynamic response of the class H1 pole are studied. The effect of the non-linear soil springs is considered to predict pole failure criteria.

The test results from the test poles are compared with theoretical results using SAP2000 and MATLAB code. The study will also highlight the potential errors or discrepancies in the wood utility pole analysis and design currently adopted by engineers.

1.5 Assumptions and Conditions

1. The displacements are in the X- or Y- and Z-axis only.
2. The displacements are measured at the top of the pole for the test poles.
3. For the theoretical study, wind exposure category D is chosen to simulate exposure to coastal wind.
4. The wind loads are computed based on ASCE 7-16.

CHAPTER II

2 EXPERIMENTAL STUDY

2.1 Experimental Setup

This section discusses the experimental setup to determine the natural frequency and damping ratios of the test specimen. Figure 6-1 and Figure 6-2 show drawings of the steel test frame, and Figure 6-3 is a picture of the test frame. The test frame comprises 2 1/2” x 2-1/2” x 3/16” steel angles and bolted connections using ½” diameter bolts.

2.2 Test Scheme

The test poles were tested to determine the natural frequency, damping ratio, and Young’s Modulus of the wood species. The span of the cable element used was approximately 25’ 0” and ¼” in diameter for cable load-displacement characteristics.

2.3 Test Specimen Material Properties

This test was performed to document the physical dimensions and weights of the test specimen. These measured values will be input parameters for further calculations and analysis. The measured physical properties of the test specimens are shown in Table 2-1 and Table 2-2. The properties of the cable used in this test program are shown in Table 2-3.

2.3.1 Dynamic Response Pull Test

This test was performed to determine the dynamic response of the test pole for various initial displacements. The initial displacement was gradually increased until the pole's failure or the experimental setup's limits were reached.

2.3.2 Dynamic Response Pull Test No. 1

The 6’ 0” test pole (Test Specimen TP1) was cut to 4’ 0” at the base to fit in the frame. The test pole is shown in Figure 6-5. Movement at the base was observed during the test, but the test was continued, noting the base connection movement. The test was stopped after the test specimen was displaced to 3.39 inches.

This test No. 1 (Test Specimen TP1) was then repeated since significant movement at the base was observed. The base assembly was modified to ensure a fixed base condition. The wireless accelerometer was securely attached to the top of the pole and connected to the receiver and computer. The pole was tested for displacements up to 4.93 inches; however, the test specimen did not exhibit any signs of cracks or fractures.

2.3.3 Dynamic Response Pull Test No.2.

Test Specimen TP1 used in test No. 1, was reused in this test No. 2. The wireless accelerometer was securely installed on the top of the pole and connected to the receiver and computer. The specimen was displaced up to 7.25 inches, but there was no sign of cracks or fractures.

2.3.4 Dynamic Response Pull Test No. 3

The test specimen, TP2, was installed in the frame with a new connection detail shown in Figure 2-1 below:

Figure 2-1. Test No. 3 and Fixed Base Connection Detail

The bottom of the pole was in contact with the floor and secured against the base of the steel frames to prevent any movements. The wireless accelerometer was securely attached to the top of the test pole and connected to the receiver and computer to record the accelerations. The pole failed at a displacement of 4.98 inches.

2.3.5 Cable Pull Test

This test was conducted to study the load-displacement characteristics of the cable. The primary goal is to understand the non-linear nature of the cable load-displacement behavior, and agreement with the theoretical values.

2.3.6 Properties of Test Pole

The weight and dimensions of the pole were measured using a digital gage. The results of the measured dimensions and weight are shown in Table 2-1 below.

Table 2-1: Measured Pole Dimensions and Weights

Test Pole Number	Top Diameter [in]	Bottom Diameter [in]	Length [ft]	Measured Weight [lbf]	Volume [ft^3]	Unit Weight [pcf]
TP1	1.463	1.95	4.00	2.190	0.064	34.46
TP2	1.497	2.37	6.02	3.890	0.122	31.86
TP3	1.460	2.37	6.00	3.630	0.120	30.25
TP4	1.493	2.39	6.03	3.980	0.124	32.09
Average	1.48	2.37				32.16

The average tip diameter of the test poles is 1.48 inches. The average base diameter for the 6’ 0” test poles is 2.37 inches. The average unit weight of the wood specimen used is 32.16 pounds per cubic foot (pcf).

Table 2-2: Section Properties of Test Poles

Test Pole Number	Tip Area [in^2]	Base Area [in^2]	Moment of Inertia at Tip [in^4]	Moment of Inertia at Base [in^4]	Section Modulus at Tip [in^3]	Section Modulus at [in^3]
TP1	1.682	2.997	0.225	0.715	0.308	0.732
TP2	1.759	4.412	0.246	1.549	0.329	1.307
TP3	1.674	4.424	0.223	1.557	0.306	1.312
TP4	1.751	4.486	0.244	1.602	0.327	1.340

The calculated section properties of the test specimens, TP1, TP2, TP3, and TP4 are shown Table 2-2. These computed values will be used to determine the dynamic responses of the test specimen.

2.4 Test Specimen Wood Species

The test poles are made from the Western Red Cedar species. [Western Red Cedar] also called western arborvitae, giant arborvitae, or Pacific red cedar, is an ornamental and timber evergreen conifer of the cypress family (Cupressaceae), native to the Pacific coast of North America.

Western red cedars and shrubs and shrubs are pyramidal. The trees may grow up to 60 meters (about 200 feet) tall and 6 meters in circumference. The cinnamon-red or brownish outer bark is relatively thin, fissured, and scaly, shredding in regular flakes, while the inner bark is fibrous. Short, horizontal, or slightly drooping branches bear dense branchlet systems in flattened sprays that appear bright green beneath. Pictures of these wood species are shown in Figure 6-11 and Figure 6-12.

2.5 Cable Tension Test

Two (2) cable lengths of 27’ 7” and 31’ 9” were used to study the load-displacement characteristics of the cable. Table 2-3 shows cable spans and the measure weights. Cable tensions are computed based on the measured weights.

Table 2-3: Measured Weight of Cable

	Length of Cable			Weight of Cable	
S. No	[ft]	[in]	Ft (decimal)	Total Weight [lbf]	Weight per linear feet [plf]
1	27	7	27.583	3.24	0.117
2	31	9	31.750	3.89	0.123

Table 2-4 and Table 2-5 show the measured cable tensions for various longitudinal displacements. The plot of cable displacements vs cable tension is shown in Figure 2-2, Figure 2-3, and Figure 2-4.

Table 2-4: Measured Cable Tension and Displacements for Cable Profile 1

Test Cable Profile 1						
	Span (ft)			Displacement at support (in)	sag (in)	tension(lbs.)
S. No	ft	in				
1	25	4.00	3.76	0.00	18.250	7.41
2			3.70	-0.06	17.750	7.68
3			3.38	-0.38	16.500	8.48
4			3.00	-0.76	15.000	9.52
5			2.51	-1.25	12.500	12.16
6			2.44	-1.32	11.875	13.11
7			2.20	-1.56	10.375	16.24
8			1.86	-1.90	8.175	24.77
9	24	10.50	1.12	0.00	30.000	4.27
10			1.34	0.22	30.500	4.26
11			1.65	0.53	30.750	4.26
12			2.05	0.93	31.750	4.06
13			2.88	1.76	34.750	3.83
14			3.91	2.79	35.375	3.68

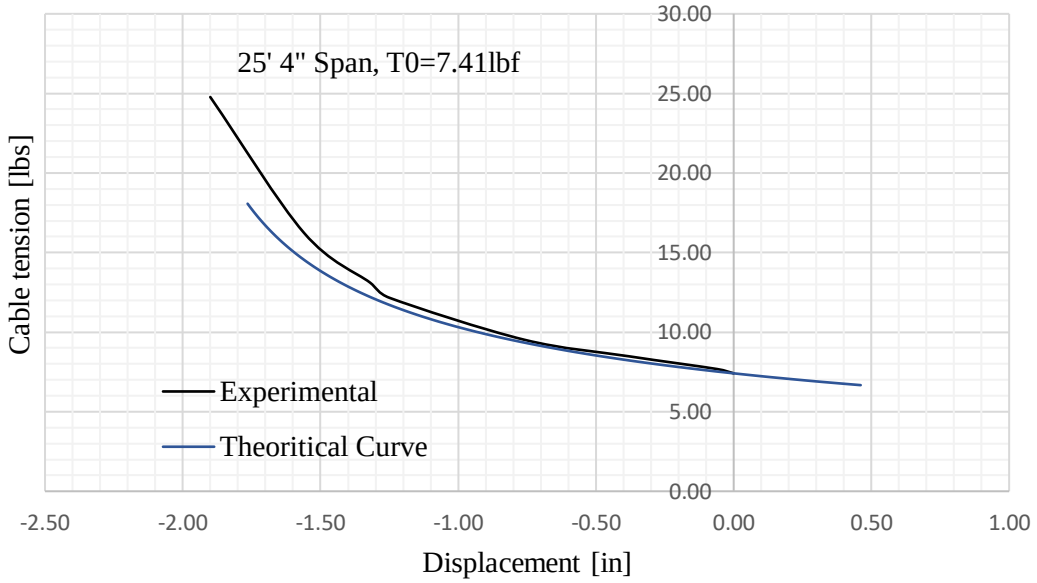

Figure 2-2. Graph of Cable Tension Vs. Displacement (+x) for 25’ 4” Cable Span

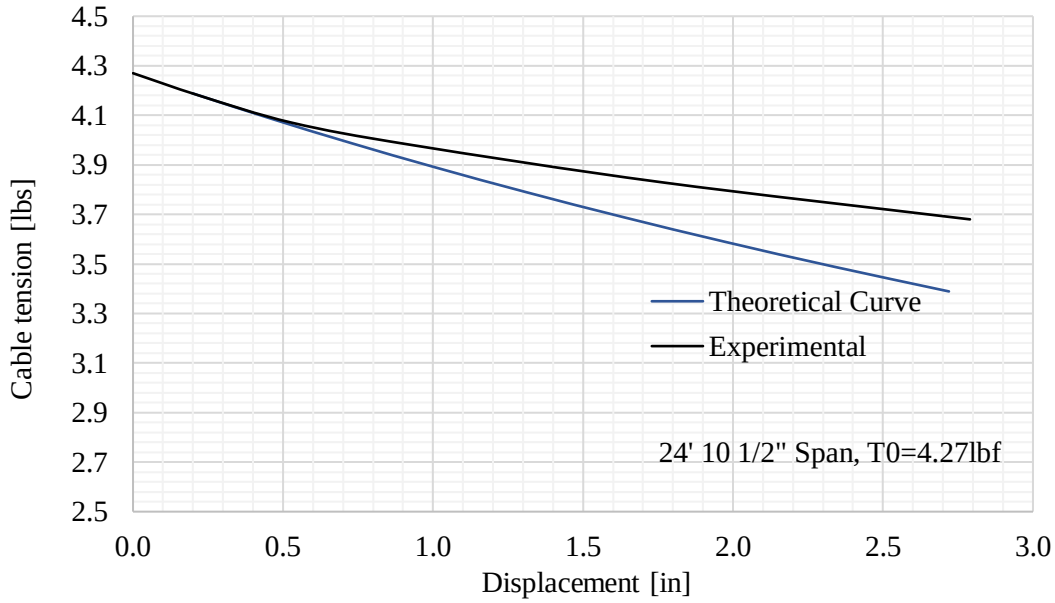

Figure 2-3. Graph of Cable Tension Vs. Displacement (-x) for 24' 10 1/2" Cable Span

Table 2-5: Measured Cable Tension and Displacement for Cable Profile 2

Test Cable Profile 2						
	Span (ft.)			Displacement at support (in)	Sag (in)	Tension (lbf)
S. No	ft	in				
1	31	7.50	1.90	0.00	12.500	19.92
2			2.21	0.22	14.250	15.97
3			2.62	0.53	16.625	13.47
4			2.88	0.94	17.750	11.50
5			3.27	1.20	20.250	10.69
6			3.88	1.59	22.250	9.48

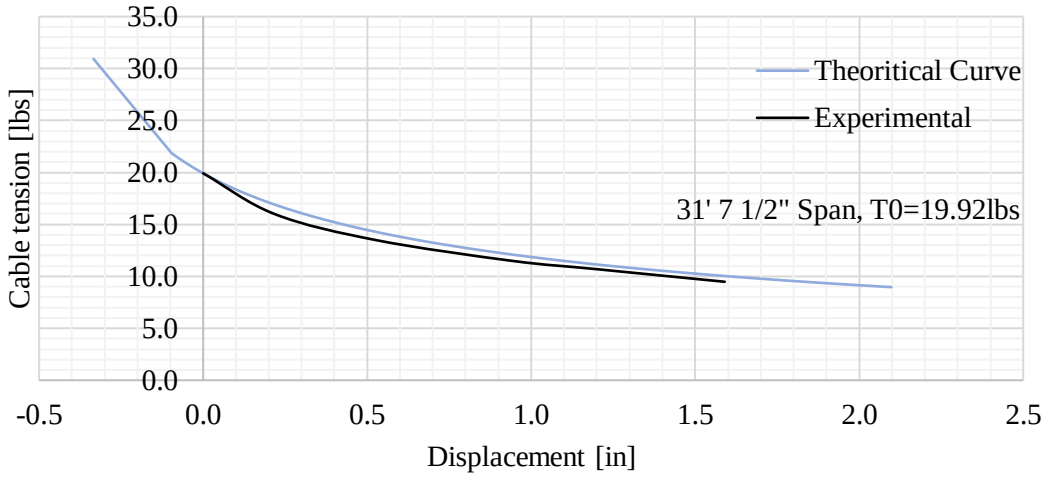

Figure 2-4. Graph of Cable Tension Vs. Displacement (-x) for 31' 7 1/2" Cable Span

From Figure 2-2, Figure 2-3, and Figure 2-4, it can be concluded that there is a reasonably good agreement, within experimental errors, between the experimentally measured and theoretical load-displacement curves.

2.6 Theoretical Load Displacement Curve of 7mm (1/4”) Diameter Cable.

The theoretical load-displacement curve for a 7mm cable is shown in Figure 2-5. The graph plotted for a positive displacement of about 3.28 inches and a negative displacement of 1.12”. The corresponding cable force is 9.96 lbs. and 99.57 lbs., respectively. The non-linear nature of the cable profile is evident.

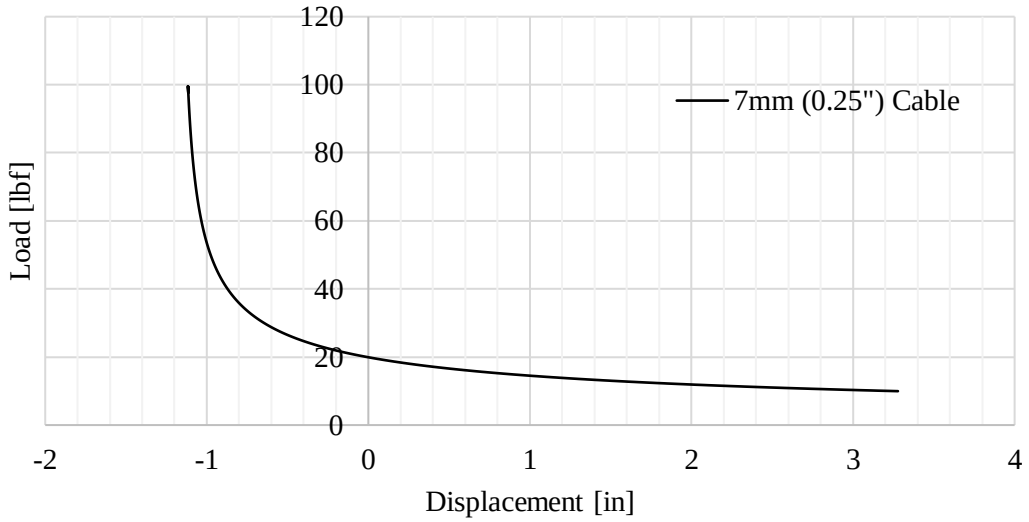

Figure 2-5. Theoretical Load Displacement Curve for 7mm Cable

2.7 Determination of Young's Modulus of Wood Specimen

A simple static pull test was conducted to estimate the Young's Modulus of the wood test specimen. The applied load and corresponding displacement values are shown in Table 2-6. In the table, the experimental and calibrated are shown.

Table 2-6: Static Load-Displacement Test Data

No.	Displacement [in]	Load [lbf]	Experimental Young's Modulus [ksi]	Calibrated Applied Load [lbf]	Calibrated Young's Modulus [ksi]	Variation
1	0.72	26.77	3550	26.33	3435	3%
2	0.82	29.28	3450	30.14	3435	0%
3	0.83	30.91	3535	30.52	3435	3%
4	0.94	34.89	3535	34.71	3435	3%
5	1.11	41.06	3535	41.19	3435	3%
6	1.19	45.23	3590	44.24	3435	4%
7	1.25	46.64	3590	46.53	3435	4%
8	1.41	49.98	3390	52.62	3435	-1%
9	1.47	52.99	3450	54.91	3435	0%
10	1.63	67.67	3950	61.00	3435	13%
11	1.88	68.02	3450	70.53	3435	0%

A plot of the experimental load-displacement curve is shown in **Error! Reference source not found.**. A linear interpolation curve is also inserted in the figure to predict the

trend of the experimental data. The load-displacement curve was plotted using only valid data. The load was then calibrated based on the equation of the trend curve.

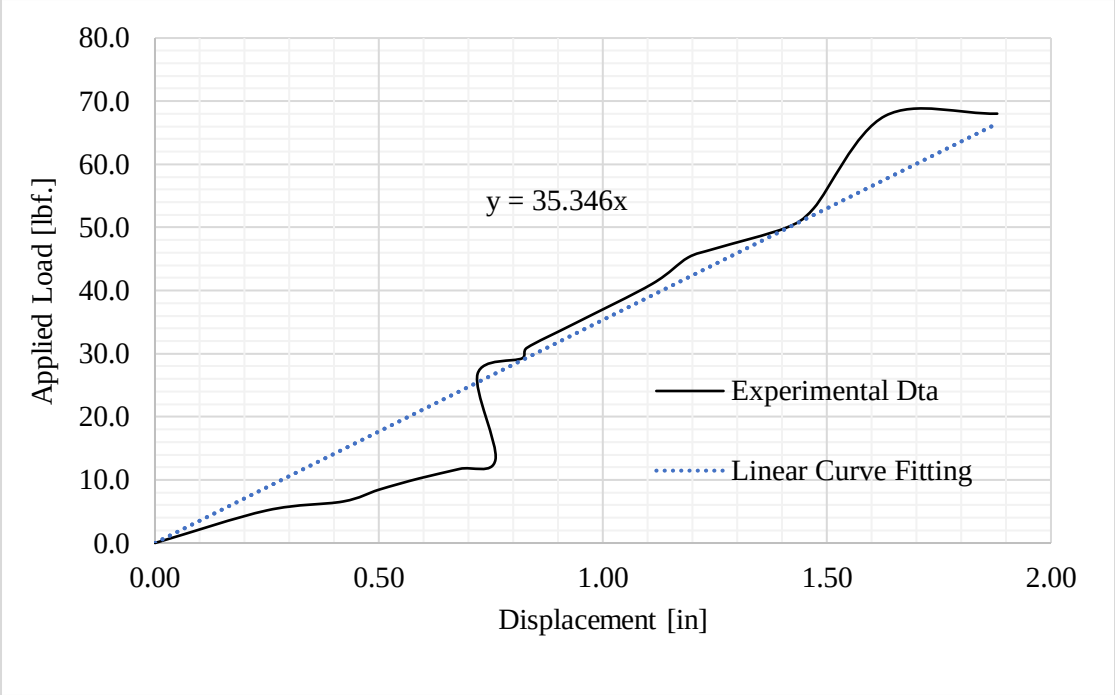

Figure 2-6. Load Displacement for Test Pole

The Young's modulus was calculated using a MATLAB code based on the Finite Element consistent mass and stiffness formulation for a tapered test specimen with inputs from the load-displacement experimental data.

The estimated value of Young's Modulus based on the calibrated loads is approximately 3535 ksi and is within the range of published values for the Cedar Wood species. This value will be used for all computations in this study. Based on the

experimentally obtained Young's modulus, the stiffness of the test pole is computed. The computed stiffness of the test pole is 0.0377 kip/in (37.7 lbs./in).

2.8 Static Pull Test Number 1

The static pull test is conducted to calculate the test specimen's natural frequencies and damping ratios.

Figure 2-7. Fixed Base Condition -Option 1 Base Connection

The computed dynamic properties are shown in Table 2-7. Figure 2-7 shows the base connection. The base connection had significant movements during the test. The base connection movement raised concerns about the validity of the test results. The test pole was secured to the base plate assembly to ensure no movement in the base during the test, and to simulate a fixed base. The natural frequency was calculated using a Fast Fourier Transform (FFT) in MATLAB code for each test data. The damping ratio was calculated by curve fitting a theoretical curve over the experimental data.

Table 2-7: Dynamic Properties for Test No. 1

S. No	Period, [sec]	Natural Frequency [Hz]	Damping Ratio [%]
1	0.050	20.125	1.804
2	0.043	23.295	1.133
3	0.048	20.825	2.678
4	0.050	19.973	2.154
5	0.046	21.512	1.214
6	0.046	21.540	8.226
Average	0.047	21.212	2.868

This test's mean natural period and frequency were 0.047s and 21.212Hz, respectively. The mean estimated damping ratio was 2.868%.

2.9 Static Pull Test Number 2

The previous Pull Test Number 1 was repeated because of concerns of the base movements during the test. The base connection was secured properly with additional

shims to prevent movement., and the test repeated. The natural frequencies, periods, and damping ratios are computed from the acceleration records. The calculated periods, natural frequencies, and damping ratios are shown in Table 2-8.

Table 2-8: Dynamic Properties for Test No. 2

S. No	Period, [sec]	Natural Frequency [Hz]	Damping Ratio [%]
1	0.047	21.294	1.106
2	0.046	21.514	0.517
3	0.044	22.899	1.156
4	0.046	21.645	0.588
Mean	0.046	21.614	1.021

The mean natural period and frequency were estimated at 0.046s and 21.613Hz, respectively. The mean calculated damping ratio was 1.021% for this 2nd test.

2.10 Static Pull Test Number 3

Test pole 2 (TSP 2) was used for this test. The properties of the test pole, TSP 2, are shown in Table 2-1. The accelerations were recorded for various initial displacements. A MATLAB code was developed to analysis the data for Periods, Natural frequencies, and damping ratios. The result of the analysis is summarized in Table 2-9.

Table 2-9: Dynamic Properties of Test Pole for Experiment Number 3

Test No.	Period, [sec]	Natural Frequency [Hz]	Damping Ratio [%]
1	0.048	20.736	1.288
2	0.056	17.861	0.731
3	0.050	20.200	0.796
4	0.042	23.877	1.041
5	0.048	20.842	1.577
6	0.046	21.646	1.090
7	0.046	21.779	0.975
8	0.044	22.550	0.594
9	0.044	22.709	1.058
Average	**0.047**	**21.355**	**1.017**

The average natural period and frequency is 0.047s and 21.355 Hz. The estimated average damping ratio was 1.01% for this 3rd test.

2.11 Bending Stress of Test Specimen

A static pull test was done to determine the bending stress, and stiffness of the test specimen. The test specimen broke when the displacement at the top of the pole reached 4.98 inches. The failure load corresponding to failure displacement and test specimen bending stiffness is 0.188 kip (187.8 lbs.). The bending stress at failure was calculated to be 2.214 ksi for the test specimen.

CHAPTER III

3 THEORETICAL ANALYSIS

When a flexible chain or rope is loosely hung between two fixed points, it hangs in a curve that looks a little like a parabola, but in fact is not quite a parabola; it is a curve called a catenary, which is a word derived from the Latin catena, a chain. There are many types of electric utility cables such as ABC, All Aluminum Conductor, All Aluminum Alloy Conductor, Aluminum Conductor Steel-Reinforced etc. Electric utility cables typically have a code word named after birds, like Turkey, Swan, Swanate, Sparroe, to name a few. Each code word has a specific sizes kcmil or AWG. kcmil stands for thousands of circular mils. AWG stands for American Wire Gauge. Each cable code word has a specific wire size, weight, rated strength, ampacity and electric resistance.

3.1 Geometric Properties of Cable Profile

This section presents the theoretical derivation of the mathematical equations that describe the behavior of cable elements.

Utility poles form the backbone of electrical infrastructure in the U.S. These utility poles support overhead power distribution lines to distribute power throughout the country. Power lines are typically attached and located at the top of the pole. They carry the electric power and deliver high-voltage electricity from a nearby substation to the transformer, which then lowers the voltage for everyday use by customers.

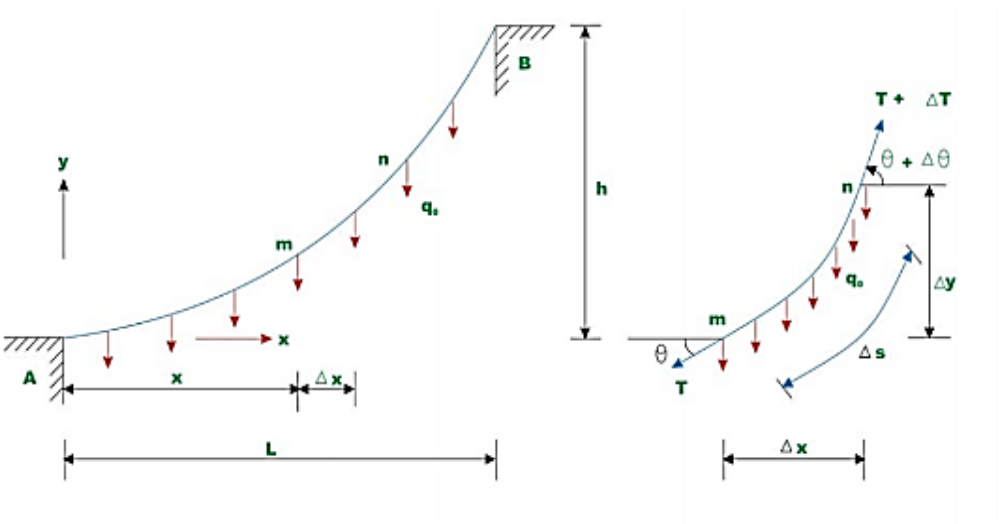

Figure 3-1. Cable Profile and Notations

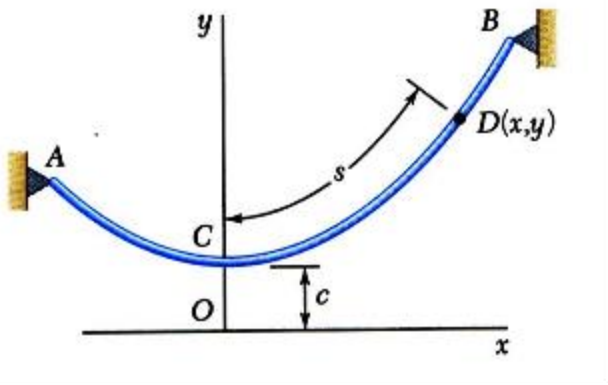

Figure 3-2. Cable Supported at Unequal Elevations.

Utility poles are also used to support communication cables. In many situations, utility poles support both electric power, and communication cables. Communication cables are often lighter, and smaller in diameter, hence the cable tension from these cables is much smaller than electric cables.

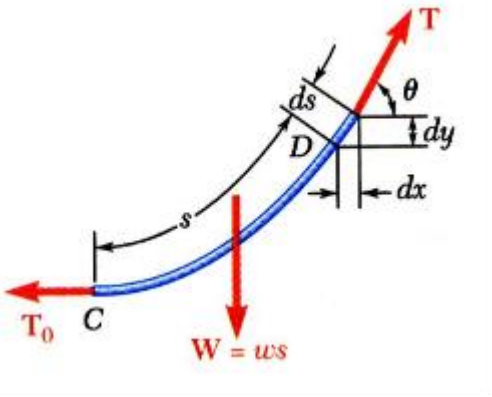

Figure 3-3. Segment of Cable

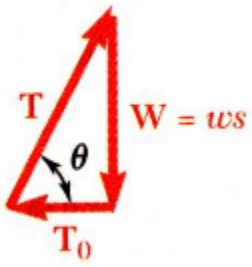

Figure 3-4. Static Equilibrium of Forces

Figure 3-1, Figure 3-2, Figure 3-3, and Figure 3-4 show a cable profile with the relevant notations and dimensions for analyzing a cable element.

L or l = the distance from the low point of a cable to support along the X-axis.

T = tension in cable at any given point

T_0 = tension in cable at the low point of the curve

w = weight of cable per unit length

S = length of cable

The rate of change of angle of direction from points m to n is given by $\frac{\delta s}{\delta \theta}$

Takings limits

$$\lim_{\delta s \to o} \frac{\delta \theta}{\delta s} = \frac{d\theta}{ds} \quad (1)$$

where, $\frac{d\theta}{ds}$ is the curvature if a curve at a given point.

Also, the arc length, ds, is given by

$$ds = R \cdot d\theta \quad (2)$$

Rearranging equation (2)

$$\frac{d\theta}{ds} = \frac{1}{R} \quad (3)$$

Where R is the radius of curvature

From Figure 3-3,

$$\frac{dy}{dx} = \tan(\theta) \tag{4}$$

Differentiating with respect to s

$$\frac{d}{ds}\left(\frac{dy}{dx}\right) = \frac{d}{dx}\tan(\theta) \tag{5}$$

Equation (5) can be rewritten as follows

$$\frac{d}{dx}\left(\frac{dy}{dx}\right)\frac{dx}{ds} = \frac{d}{d\theta}\tan(\theta)\frac{d}{ds}\theta \tag{6}$$

Equation (6) reduces to

$$\frac{d^2}{dx^2}y.\cos\theta = sec^2(\theta).\frac{1}{R} \tag{7}$$

Rearranging equation (7)

$$\frac{d^2}{dx^2}y.\cos(\theta) = \frac{sec^2(\theta)}{\cos(\theta)}.\frac{1}{R} \tag{8}$$

$$\frac{d^2}{dx^2}y.\cos(\theta) = \sec^3\theta\,.\frac{1}{R} \tag{9}$$

From trigonometric identity,

$$\sec^2\theta = 1 + \tan^2\theta \tag{10}$$

Substituting equation (10) into Equation (9)

$$\frac{d^2}{dx^2}y = (1 + \tan^2\theta)^{\frac{3}{2}}.\frac{1}{R} \quad (11)$$

Substituting equation (4) into Equation (11)

$$\frac{d^2}{dx^2}y = (1 + \left(\frac{dy}{dx}^2\right))^{\frac{3}{2}}.\frac{1}{R} \quad (12)$$

(12) to get the equation for curvature, R

Rearranging equation

$$R = \frac{(1 + \left(\left(\frac{dy}{dx}\right)^2\right))^{\frac{3}{2}}}{\frac{d^2}{dx^2}y} \quad (13)$$

Rearranging equation (12), the equation for the curvature of a curve is obtained

$$\phi = \frac{\frac{d^2}{dx^2}y}{(1+\left(\frac{dy}{dx}\right)^2)^{\frac{3}{2}}} \quad (14)$$

where ϕ is the curvature of a curve

3.2 Length of a Cable Profile

The arc length of a small segment of a curve is given by

$$\delta s = R.\delta\theta \quad (15)$$

Rearranging equation (15)

$$\frac{1}{R} = \frac{\delta\theta}{\delta s} \quad (16)$$

Taking limits on both sides

$$\lim_{\delta S \to 0} \frac{\delta\theta}{\delta s} = \frac{d\theta}{ds} \tag{17}$$

Therefore,

$$\frac{d\theta}{ds} = \frac{1}{R} \tag{18}$$

Form trigonometry, the following expressions,

$$\frac{dy}{dx} = \tan\theta \tag{19}$$

$$\frac{dy}{ds} = \sin\theta \tag{20}$$

$$\frac{dx}{ds} = \cos\theta \tag{21}$$

Now, using the Pythagorean theorem,

$$(ds)^2 = (dx)^2 + (dy)^2 \tag{22}$$

Dividing equation (22) by $(dx)^2$ to get

$$\left(\frac{ds}{dx}\right)^2 = \left(\frac{dx}{dx}\right)^2 + \left(\frac{dy}{dx}\right)^2 \tag{23}$$

$$\left(\frac{ds}{dx}\right)^2 = 1 + \left(\frac{dy}{dx}\right)^2 \tag{24}$$

$$\frac{ds}{dx} = \sqrt{\left(1 + \left(\frac{dy}{dx}\right)^2\right)} \tag{25}$$

$$ds = \sqrt{\left(1 + \left(\frac{dy}{dx}\right)^2\right).dx} \tag{26}$$

Equation (26) is integrated to get the length of a curve between any two given points,

$$\int_0^l ds = \int_0^l \sqrt{\left(1 + \left(\frac{dy}{dx}\right)^2\right).dx} \tag{27}$$

$$s = \int_0^l \sqrt{\left(1 + \left(\frac{dy}{dx}\right)^2\right).dx} \tag{28}$$

where s is the length of the curve.

3.3 Cable Force

Figure 3-1, and Figure 3-4, shows the forces in a segment of a cable,

$$\sum Fx = 0 \tag{29}$$

$$-T_0 + T.cos(\theta) = 0 \tag{30}$$

$$T = \frac{T_0}{cos(\theta)} \tag{31}$$

$$\sum Fy = 0 \tag{32}$$

$$-ws + T.sin(\theta) = 0 \tag{33}$$

$$ws = T.sin(\theta) \tag{34}$$

$$s = \frac{T}{w}.sin(\theta) \tag{35}$$

Substituting equation (31) into equation (35)

$$s = \frac{T_0}{cos(\theta).w}.sin(\theta) \tag{36}$$

$$s = \frac{T_0}{w}.tan(\theta) \tag{37}$$

Substituting equation (19) into equation (37)

$$s = \frac{T_0}{w}.\frac{dy}{dx} \tag{38}$$

Let,

$$c = \frac{T_0}{w} \tag{39}$$

where c is a constant

Therefore, equation (38) simplifies to:

$$s = c.\frac{dy}{dx} \tag{40}$$

Differentiating equation (40) with respect to x to get

$$\frac{ds}{dx} = c.\frac{d}{dx}\left(\frac{dy}{dx}\right) \tag{41}$$

Let $\rho = \frac{dy}{dx}$

$$\frac{ds}{dx} = c.\frac{d}{dx}(\rho) \tag{42}$$

Substituting equation (25) into equation (42) and rearranging to get

$$\sqrt{(1 + (\rho)^2)} = c.\frac{d}{dx}(\rho) \tag{43}$$

Rearranging equation (43)

$$dx = \frac{c}{\sqrt{(1 + (\rho)^2)}}d\rho \tag{44}$$

Integrating both sides of equation (44)

$$\int dx = \int \frac{c}{\sqrt{(1 + (\rho)^2)}}d\rho \tag{45}$$

$$x = c_1 + c.\sinh^{-1}\rho \tag{46}$$

where, c_1 is a constant of integration.

Applying boundary conditions to find c_1

$x = 0$

$\frac{d\rho}{dy} = 0$

$c_1 + \sinh^{-1}(0) = 0$

Therefore,

$c_1 = 0$

Therefore, equation (46) reduces to:

$$x = c.\sinh^{-1}\rho \tag{47}$$

Rearranging Equation (47)

$$\frac{x}{c} = \sinh^{-1}\rho \tag{48}$$

$$\rho = \sinh\frac{x}{c} \tag{49}$$

Substitute $\rho = \frac{dy}{dx}$ into equation (49) to get

$$\frac{dy}{dx} = \sinh\frac{x}{c} \tag{50}$$

$$dy = \sinh\frac{x}{c}\ dx \tag{51}$$

Integrating equation (51)

$$\int dy = \int \sinh\frac{x}{c}\ dx \tag{52}$$

$$y = c.\cosh\left(\frac{x}{c}\right) \tag{53}$$

Equation (53) is the equation of a catenary or cable.

Substituting for $c = \frac{T_0}{w}$

$$y = \frac{T_0}{w}.\cosh\left(\frac{x}{c}\right) \tag{54}$$

3.4 Length of Curve

To obtain an expression for the length of a curve, we differentiate equation (53)

$$\frac{dy}{dx} = \frac{d}{dx}(c.\cosh\left(\frac{x}{c}\right)) \tag{55}$$

$$\frac{dy}{dx} = \sinh\left(\frac{x}{c}\right)) \tag{56}$$

Substituting $\frac{dy}{dx} = \sinh\left(\frac{x}{c}\right))$ into equation (28) and integrating for half the length because of symmetry:

$$s = \int_0^l \sqrt{\left(1 + \left(\sinh\left(\frac{x}{c}\right)^2\right).dx} \tag{57}$$

$$s = \int_0^l \cosh\left(\frac{x}{c}\right) dx \tag{58}$$

Equation (58) reduces to:

$$s = c.\sinh\left(\frac{l}{c}\right) \tag{59}$$

Substituting the expression for c into equation (59) to get,

$$s = \frac{T_0}{w}.\sinh\left(\frac{l}{\frac{T_0}{w}}\right) \tag{60}$$

The equation for the length of the curve is given by equation (61)

$$s = \frac{T_0}{w}.\sinh\left(\frac{w.l}{T_0}\right) \tag{61}$$

3.5 Sag in Cable

In Figure 3-1, the sag in a cable is defined as the vertical distance between the lowest point on the cable profile (or origin) and the support,

$$sag = y - c \tag{62}$$

$$sag = c.\cosh\left(\frac{l}{c}\right) - c \tag{63}$$

$$sag = c.\cosh\left(\frac{l}{c}\right) - c \tag{64}$$

$$sag = c.(\cosh\left(\frac{l}{c}\right) - 1) \tag{65}$$

$$sag = \frac{T_0}{w}.(\cosh\left(\frac{l}{\frac{T_0}{w}}\right) - 1) \tag{66}$$

$$sag = \frac{T_0}{w}.(\cosh\left(\frac{w.l}{T_0}\right) - 1) \tag{67}$$

A cable profile can also be expressed as an expansion series.

Equation (53) is shown below, can be expressed as an infinite series as shown in equation (69),

$$y = c \cdot \cosh\left(\frac{x}{c}\right)$$

$$y = c.(1 + \frac{1}{2!}.\left(\frac{x}{c}\right)^2 + \frac{1}{4!}.\left(\frac{x}{c}\right)^4 + \cdots \frac{1}{n!}.\left(\frac{x}{c}\right)^n \quad (68)$$

For a cable profile $\frac{x}{c}$ is typically less than 1, hence $\frac{1}{4!}.\left(\frac{x}{c}\right)^4$ and higher orders can be neglected.

Equation (68) reduces to:

$$y = c.\left(1 + \frac{1}{2!}.\left(\frac{x}{c}\right)^2\right) \quad (69)$$

Sag in a cable profile is given by,

$$sag = y - c \quad (70)$$

Substituting (69) into (70) to get

$$sag = c.\left(1 + \frac{1}{2!}.\left(\frac{x}{c}\right)^2\right) - c \quad (71)$$

Equation (71) is simplified as follows

$$sag = c + \frac{c}{2}.\left(\frac{x}{c}\right)^2 - c \quad (72)$$

$$sag = \frac{c}{2}.\left(\frac{x}{c}\right)^2 \tag{73}$$

$$sag = \frac{\frac{T_0}{w}}{2}.\left(\frac{x}{\frac{T_0}{w}}\right)^2 \tag{74}$$

Substituting $x = l$ to get

$$sag = \frac{w.l^2}{2.T_0} \tag{75}$$

Equation (75) is the simplified equation for a sag in one-half of a cable element.

In the case of poles with a cable attached at the top, it is necessary to determine the cable's tension for a given pole displacement. This change is displacement will result in a corresponding change in the cable tension.

Equations (54) and (61) are non-linear equations; the solution is typically by trial and error for a given value of change in displacement at the top of a pole.

3.6 Numerical Example

A numerical example is provided in this section to illustrate the behavior of the cable for displacements of the top of the pole. Consider a cable of span 100ft between two supports. The weight of the cable is 1.5 plf, with an initial cable tension of 1.0 kip.

3.6.1 Solution Process

The cable length will remain the same irrespective of the pole deflection. Hence, the span will change by the value of the pole displacement; thus, the tension in the cable will change correspondingly. The cable tension is calculated by trial and error. The calculated values of cable tension for various pole displacements are shown in Table 3-1.

$$l = 100ft$$

$$\omega = 1.5plf$$

Where l is the distance from the low point of the cable profile to the support, w is the weight per unit length of the cable.

Table 3-1: Table of Computed Displacement and Cable Tension

No.	Displacement [in]	Cable Tension [kip]	Sag [ft]
1	-12	0.515	14.552.
2	-6	0.65	11.531
3	-5	0.685	10.956
4	-4	0.725	10.352
5	-3	0.772	9.713
6	-2.5	0.8	9.379
7	-2	0.83	9.033
8	-1.5	0.865	8.674
9	-1	0.904	8.3
10	-0.5	0.948	7.91
11	0	1	7.5
12	0.5	1.061	7.068
13	1	1.135	6.608
14	1.5	1.226	6.115
15	2	1.344	5.58
16	2.5	1.503	4.989
17	3	1.736	4.32
18	3.5	2.125	3.529
19	4	3	2.5
20	4.25	4.223	1.775

Figure 3-5 shows the plot of the calculated cable tension and pole displacement. The figure shows that the cable tension displacement relationship of the chosen cable property is highly non-linear.

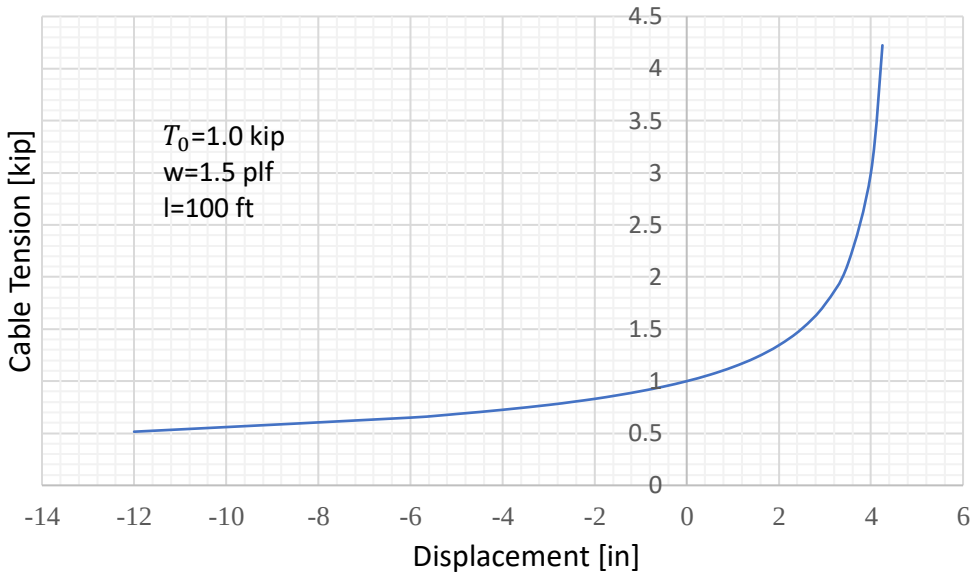

Figure 3-5. Graph of Cable Tension Vs. Displacement

The positive displacement increases the span of the cable and correspondingly increases the cable tension. Negative displacement, on the other hand, reduces the span and reduces the cable tension.

3.7 Properties of Tapered Pole

The diameter of a tapered pole at any point along its length is given by equation (76)**Error! Reference source not found.**

$$d(x) = d_b\left(1 - \frac{x}{l}\right) + \left(\frac{x}{l}\right)d_t \tag{76}$$

where,

$d(x)$ is the diameter of the pole at any given point along its length.

d_b is the diameter at the base of the pole.

d_t is the pole's diameter at the top or tip of the pole.

The second moment of Inertia of the pole cross section is given by Equation (77)

$$I(x) = \frac{\pi}{64} d(x)^4 \tag{77}$$

The cross-sectional area of the pole is given by Equation (78)

$$A(x) = \frac{\pi}{4} d(x)^2 \tag{78}$$

The weight of the pole section per unit length is given by,

$$w(x) = \frac{\pi}{4} d(x)^2 . \gamma_{wood} \tag{79}$$

where,

γ_{wood} is the density of the tapered pole wood species.

Similarly, the mass of the pole section per unit length is given by,

$$m(x) = w(x)/g \tag{80}$$

where,

g is the gravitational constant.

$m(x)$ is the mass per unit length.

3.8 Equation of Motion

The governing equation of motion of an element embedment in a layer of soil to include soil structure interaction is given by:

$$E.I(x)\frac{\partial^4 u}{\partial x^4} + m(x)\frac{\partial^2 u}{\partial t^2} + c_p\frac{\partial u}{\partial t} + c_s\frac{\partial u}{\partial t} + k_s u = f(t) \tag{81}$$

where,

u is the displacement.

E is the Young's modulus of the pole wood species

$I(x)$ is the moment of inertia od the pole section

$m(x)$ is the mass per unit length of the pole section

c_p is the damping co-efficient of the tapered wood pole

c_s is the damping co-efficient of the soil

k_s is the stiffness of the soil

$f(t)$ is any forcing function

The solution to equation (81) is performed using a finite element solution based on Galerkin's weighted average method.

$$w(x).(E.I(x)\frac{\partial^4 u}{\partial x^4} + m(x)\frac{\partial^2 u}{\partial t^2} + c_p\frac{\partial u}{\partial t} + c_s\frac{\partial u}{\partial t} + k_s u - f(t)dx) = 0 \tag{82}$$

where,

w(x) is the weighting function.

Integrating equation (82) by parts to get

$$\left[E.I(x).w(x).\frac{d^3u}{dx^3}\right]_0^l + \int_0^l (-1)\frac{d}{dx}w(x).\left(E.I(x)\frac{d^3u}{dx^3} + w(x).m(x)\frac{d^2u}{dt^2} + w(x).c_p\frac{du}{dt} + w(x)c_s\frac{du}{dt} + w(x)k_su - w(x)f(t)\right)dx = 0 \quad (83)$$

Integrating by parts again to get

$$\left[E.I(x).w(x).\frac{d^3u}{dx^3} + E.I(x)\frac{dw(x)}{dx}.\frac{d^2u}{dx^2}\right]_0^l + \int_0^l \frac{d^2}{dx^2}w(x).\left(E.I(x)\frac{d^3u}{dx^3} + \frac{d}{dx}w(x).m(x)\frac{d^2u}{\partial t^2} + w(x).c_p\frac{du}{\partial t} + w(x)c_s\frac{du}{dt} + w(x)k_su - w(x)f(t)\right)dx = 0 \quad (84)$$

$$\left[E.I(x)\left(w(x).\frac{d^3u}{dx^3}+\frac{dw(x)}{dx}.\frac{d^2u}{dx^2}\right)\right]_0^l$$

$$+\int_0^x (\left(\frac{d^2w(x)}{d_x^2}\right)\cdot E.I(x)\frac{d^2u}{dx^2}+\frac{d}{dx}w(x).m(x)\frac{d^2u}{\partial t^2}$$

$$+w(x).c_p\frac{du}{\partial t}+w(x)c_s\frac{du}{dt}+w(x)k_su-w(x)f(t))dx=0 \quad (85)$$

Equation

(85) will be solved by discretizing the pole into discrete elements. The highest order of the partial differential equation of motion is 4.

therefore,

$2m = 4$

which simplifies to

$m = 2$

Therefore, there are two (2) degrees of freedom for each node, and hence four (4) degrees of freedom per element. Each joint will have a vertical force component, shear force, and rotation.

Let the displacement be given by:

$$U(x,t) = g(x) \cdot u(t) \tag{86}$$

Equation (86) has both a dimension and time function.

let,

$$g(x) = a + b.x + c.x^2 + c.^3 \tag{87}$$

a, b, c, and d are constants to be evaluated.

Differentiating equation (87) to get

$$g'(x) = 0 + b + 2cx + 3\,\mathrm{d}x^2 \tag{88}$$

Equations (87) and (88) can be expressed in a matrix form,

$$\begin{bmatrix} y(x) \\ g'(x) \end{bmatrix} = \begin{bmatrix} 1 & x & x^2 & x^3 \\ 0 & 1 & 2x & 3x^2 \end{bmatrix} \begin{bmatrix} a \\ b \\ c \\ d \end{bmatrix} \tag{89}$$

Considering a beam element with n nodes and m elements, shown in Figure 3-6,

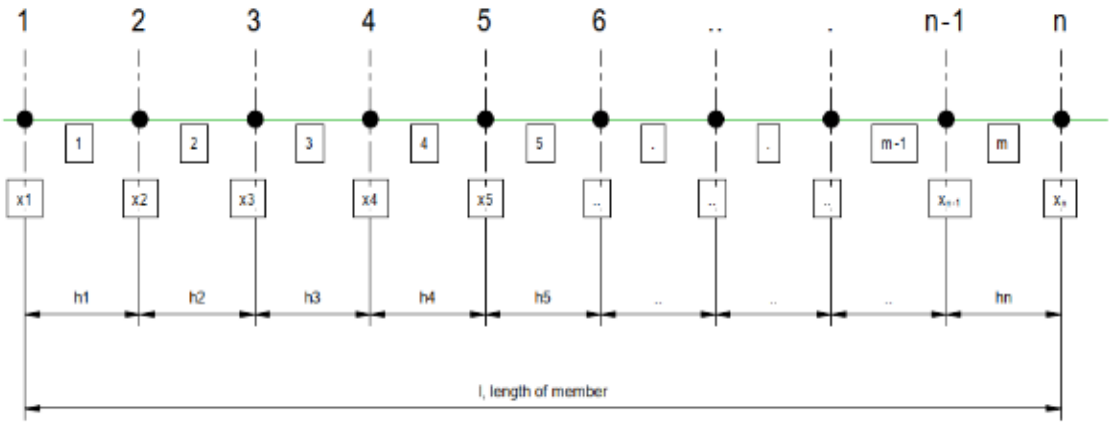

Figure 3-6. Member node and Elements

We shall define the nodal displacements and rotations as:

u_1 is nodal vertical displacement perpendicular to the element at node 1

u_2 is rotation at node 1

Similarly,

u_{n-1} is the nodal displacement at node (n-1)

u_n is rotation at node n

Applying equation (87) and (88) at nodes 1 and 2 to get,

$$u_1 = a + b.x_1 + c.x_1^2 + d.x_1^3$$

$$u_2 = 0 + b + 2.c.x_1 + 3.d.x_1^2$$

$$u_3 = a + b.x_2 + c.x_2^2 + d.x_2^3$$

$$u_4 = 0 + b + 2.c.x_2 + 3.d.x_2^2$$

The above four (4) equations can be rewritten in a matrix form,

$$\begin{bmatrix} u_1 \\ u_2 \\ u_3 \\ u_4 \end{bmatrix} = \begin{bmatrix} 1 & x_1 & x_1^2 & x_1^3 \\ 0 & 1 & 2.x_1 & 3.x_1^2 \\ 1 & x_2 & x_2^2 & x_2^3 \\ 0 & 1 & 2.x_2 & 3.x_2^2 \end{bmatrix} . \begin{bmatrix} a \\ b \\ c \\ d \end{bmatrix} \quad (90)$$

Solving for the constants a, b, c, and d,

$$\begin{bmatrix} a \\ b \\ c \\ d \end{bmatrix} = \begin{bmatrix} 1 & x_1 & x_1^2 & x_1^3 \\ 0 & 1 & 2.x_1 & 3.x_1^2 \\ 1 & x_2 & x_2^2 & x_2^3 \\ 0 & 1 & 2.x_2 & 3.x_2^2 \end{bmatrix}^{-1} . \begin{bmatrix} u_1 \\ u_2 \\ u_3 \\ u_4 \end{bmatrix} \quad (91)$$

Substituting equation (91) into equation

(89) to get

$$\begin{bmatrix} y(x) \\ g'(x) \end{bmatrix} = \begin{bmatrix} 1 & x & x^2 & x^3 \\ 0 & 1 & 2x & 3x^2 \end{bmatrix} \begin{bmatrix} 1 & x_1 & x_1^2 & x_1^3 \\ 0 & 1 & 2.x_1 & 3.x_1^2 \\ 1 & x_2 & x_2^2 & x_2^3 \\ 0 & 1 & 2.x_2 & 3.x_2^2 \end{bmatrix}^{-1} . \begin{bmatrix} u_1 \\ u_2 \\ u_3 \\ u_4 \end{bmatrix} \quad (92)$$

For a given element

$x_1 = 0$

$x_2 = h$

Hence, equation (92) becomes,

$$\begin{bmatrix} y(x) \\ g'(x) \end{bmatrix} = \begin{bmatrix} 1 & x & x^2 & x^3 \\ 0 & 1 & 2x & 3x^2 \end{bmatrix} \begin{bmatrix} 1 & 0 & 0 & 0 \\ 0 & 1 & 0 & 0 \\ 1 & h & h^2 & h^3 \\ 0 & 1 & 2.h & 3.h^2 \end{bmatrix}^{-1} . \begin{bmatrix} u_1 \\ u_2 \\ u_3 \\ u_4 \end{bmatrix} \quad (93)$$

$$\begin{bmatrix} y(x) \\ g'(x) \end{bmatrix} = [\phi_1 \quad \phi_2 \quad \phi_3 \quad \phi_4]. \begin{bmatrix} u_1 \\ u_2 \\ u_3 \\ u_4 \end{bmatrix} \quad (94)$$

$$\begin{bmatrix} \mathrm{u} \\ \theta \end{bmatrix} = [\phi_1 \quad \phi_2 \quad \phi_3 \quad \phi_4]. \begin{bmatrix} \mathrm{u}_1 \\ \mathrm{u}_2 \\ \mathrm{u}_3 \\ \mathrm{u}_4 \end{bmatrix} \quad (95)$$

where,

u is the displacement at any point along the length of the element

θ is the rotation at any point along the length of the element

h is the element size

$$[U] = \sum_{i=1}^{i=4} \emptyset_i \, . u_i \quad (96)$$

The solution of equation (96) gives the expressions for the shape functions. ϕ_1, ϕ_2, ϕ_3, and ϕ_4

$$[\phi] = \left[\frac{2x^3}{h^3} - \frac{3x^2}{h^2} + 1 \quad x - \frac{2x^2}{h} + \frac{x^3}{h^2} \quad \frac{3x^2}{h^2} - \frac{2x^3}{h^3} \quad \frac{x^3}{h^2} - \frac{x^2}{h}\right] \tag{97}$$

Therefore,

$$\phi_1 = \frac{2x^3}{h^3} - \frac{3x^2}{h^2} + 1 \tag{98}$$

$$\phi_2 = x - \frac{2x^2}{h} + \frac{x^3}{h^2} \tag{99}$$

$$\phi_3 = \frac{3x^2}{h^2} - \frac{2x^3}{h^3} \tag{100}$$

$$\phi_4 = \frac{x^3}{h^2} - \frac{x^2}{h} \tag{101}$$

The graphs for shape functions ϕ_1 and ϕ_3 are shown in Figure 3-7.

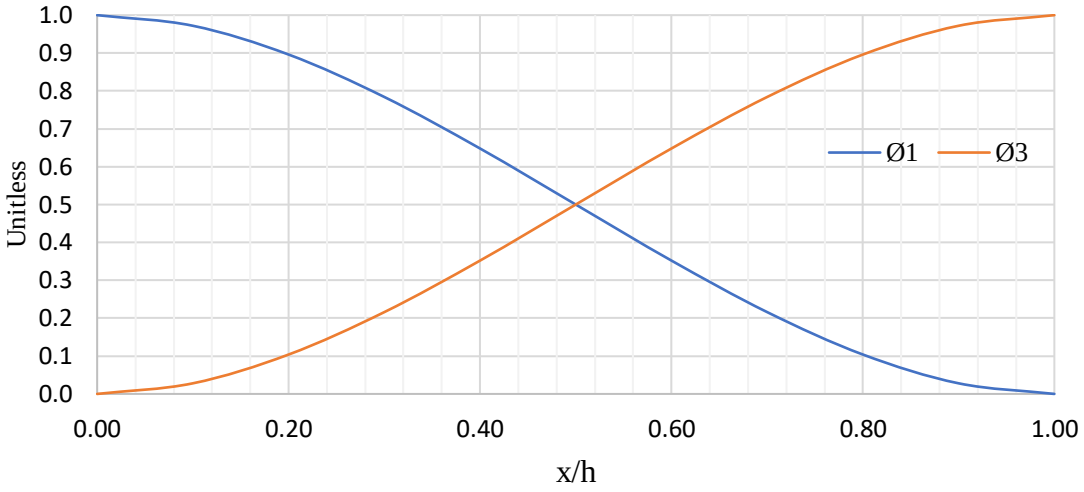

Figure 3-7. Graph for Shape Factors $\boldsymbol{\phi_1}$and $\boldsymbol{\phi_3}$

The graphs for the shape functions $\phi_2$and ϕ_4 are shown in Figure 3-8.

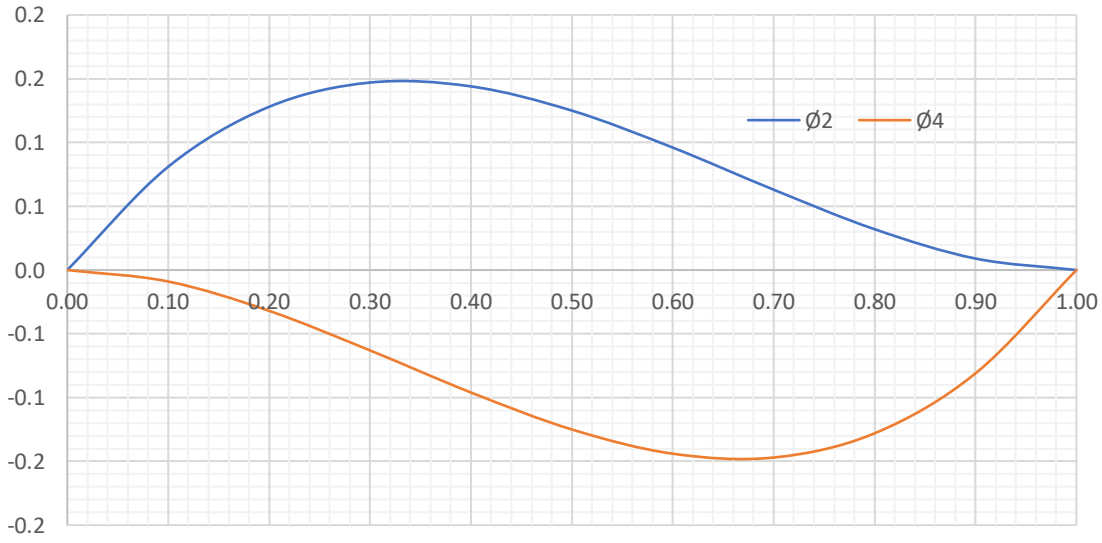

Figure 3-8. Graph for Shape Factors $\boldsymbol{\phi_2}$ and $\boldsymbol{\phi_4}$

`

3.9 Derivatives of Shape Functions

In this section, the derivatives of shape functions are discussed.

First derivatives of ϕ_1:

$$\phi'_1 = \frac{6.x^2}{h^3} - \frac{6.x}{h^2} \tag{102}$$

Where, ϕ'_1 is the first derivative of shape function.

Second derivatives of ϕ_1:

$$\phi''_1 = \frac{12.x}{h^3} - \frac{6}{h^2} \tag{103}$$

Third derivatives of ϕ_1:

$$\phi'''_1 = \frac{12}{h^3} \tag{104}$$

First derivatives of ϕ_2

$$\phi'_2 = \frac{3.x^2}{h^2} - \frac{4.x}{h} + 1 \tag{105}$$

Second derivatives of ϕ_2

$$\phi''_2 = \frac{6.x}{h^2} - \frac{4}{h} \tag{106}$$

Third derivatives of ϕ_2

$$\phi'''_2 = \frac{6}{h^2} \tag{107}$$

First derivative of ϕ_3:

$$\phi'_3 = \frac{6.x}{h^2} - \frac{6.x^2}{h^3} \tag{108}$$

Second derivative of ϕ_3:

$$\phi''_3 = \frac{6}{h^2} - \frac{12.x}{h^3} \tag{109}$$

Third derivative of ϕ_3:

$$\phi'''_3 = (-)\frac{12}{h^3} \tag{110}$$

First derivative of ϕ_3:

$$\phi'_4 = \frac{3.x^2}{h^2} - \frac{2.x}{h} \tag{111}$$

Second derivative of ϕ_4:

$$\phi''_4 = \frac{6.x}{h^2} - \frac{2}{h} \tag{112}$$

Third derivative of ϕ_4:

$$\phi'''_4 = \frac{6}{h^2} \tag{113}$$

Figure 3-9 shows the graph for $\boldsymbol{\phi'}_1$ and $\boldsymbol{\phi'}_3$. The values of $\boldsymbol{\phi'}_1$ and $\boldsymbol{\phi'}_3$at the nodal points are zero.

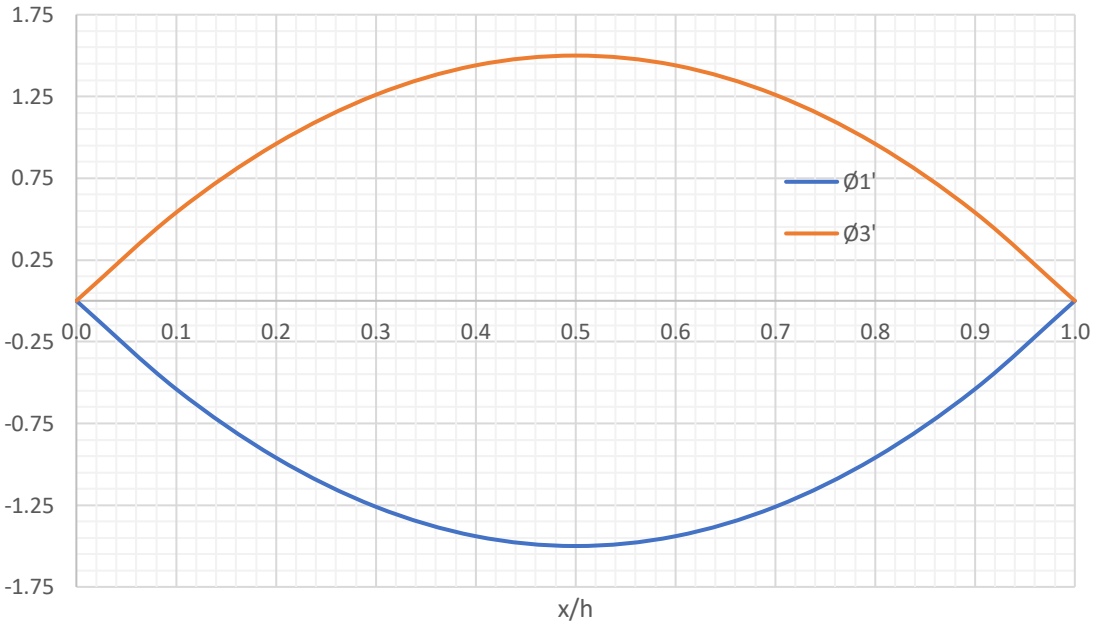

Figure 3-9. Graph of Shape Factors $\boldsymbol{\phi'}_1$ and $\boldsymbol{\phi'}_3$

Figure 3-10 shows the graph for $\boldsymbol{\phi'}_2$ and $\boldsymbol{\phi'}_4$. The values of $\boldsymbol{\phi'}_2$ at the nodal points are 1 and 0, respectively. The values at the nodal point for $\boldsymbol{\phi'}_4$ is 0 and 1.

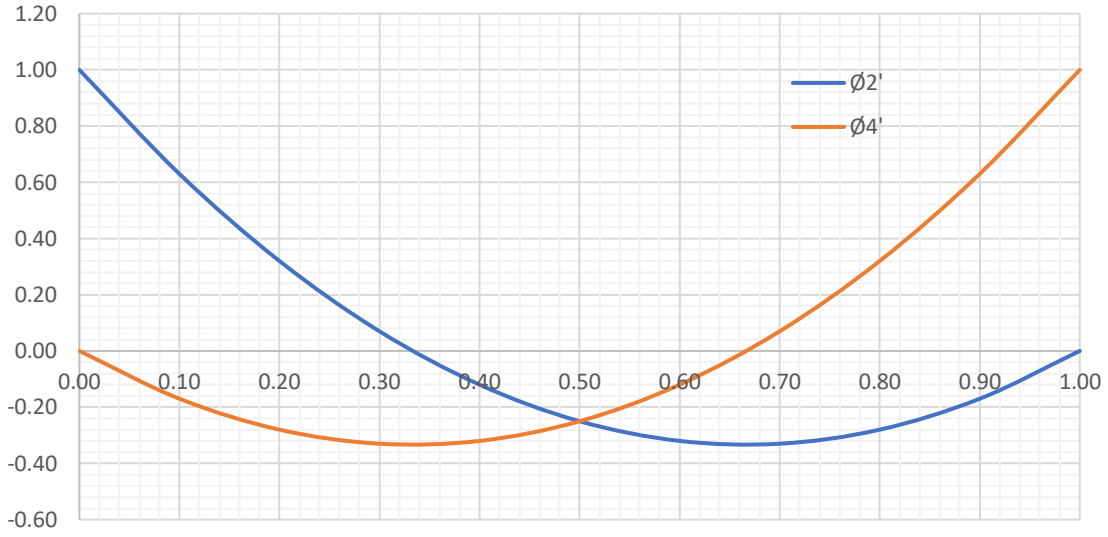

Figure 3-10. Graph of Shape Factors $\boldsymbol{\phi'}_2$ and $\boldsymbol{\phi'}_4$

Figure 3-11 shows the graph for the second derivatives of the shape functions ϕ''_1 and ϕ''_3. ϕ''_1 varies from 6 at the starting node and -6 at the ending node. Similarly, ϕ''_3 varies from -6 at the starting node to 6 at the ending node.

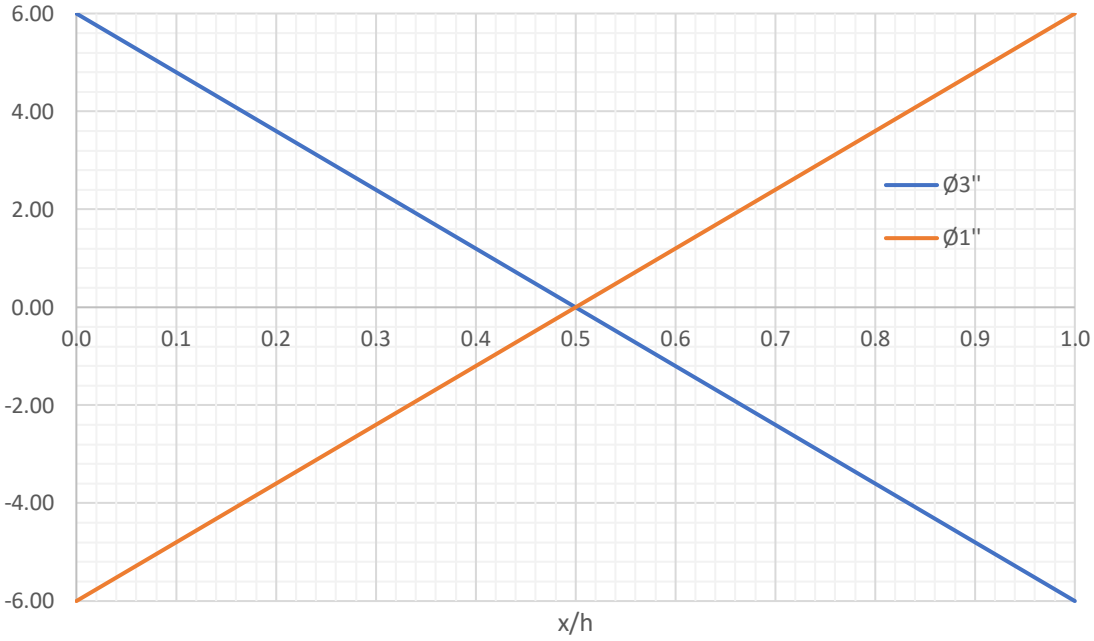

Figure 3-11. Graph of Shape Factors $\boldsymbol{\phi''_1}$ and $\boldsymbol{\phi''_3}$

Figure 3-12 shows the graph for the second derivatives of the shape functions ϕ''_2 and ϕ''_4. ϕ''_2varies linearly from -2 to +4 at the starting and ending nodes, respectively. While ϕ''_4 varies linearly from -4 to +2 at the start and end nodes, respectively.

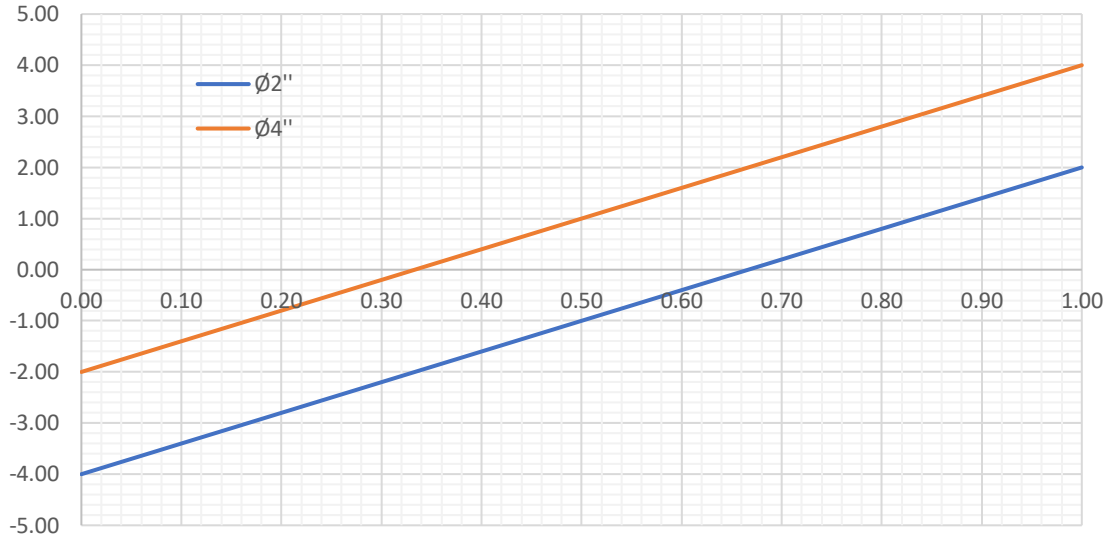

Figure 3-12. Graph of Shape Factors $\boldsymbol{\phi''}_{\mathbf{2}}$ and $\boldsymbol{\phi''}_{\mathbf{4}}$

Figure 3-13 shows the graph for the third derivatives of the shape functions ϕ'''_1 and ϕ'''_3 are constants with values of +12 and -12, respectively.

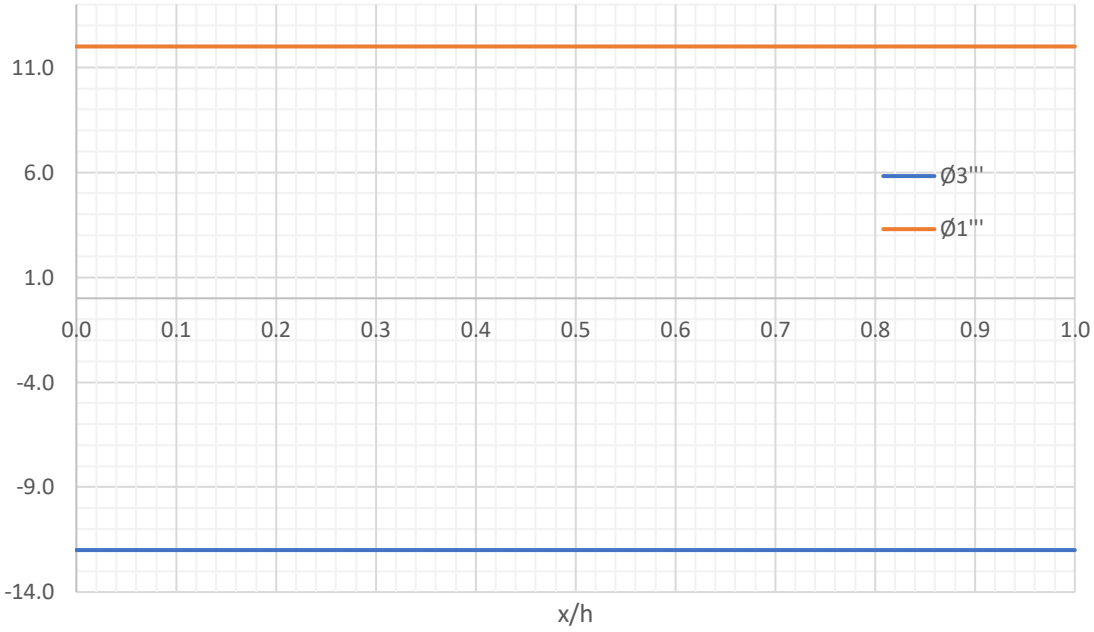

Figure 3-13. Graph of shape factors $\boldsymbol{\phi'''_1}$ and $\boldsymbol{\phi'''_3}$

Figure 3-14 shows the graph for the third derivative of the shape functions, $\boldsymbol{\phi'''_2}$ and $\boldsymbol{\phi'''_4}$ have constant values of 6.

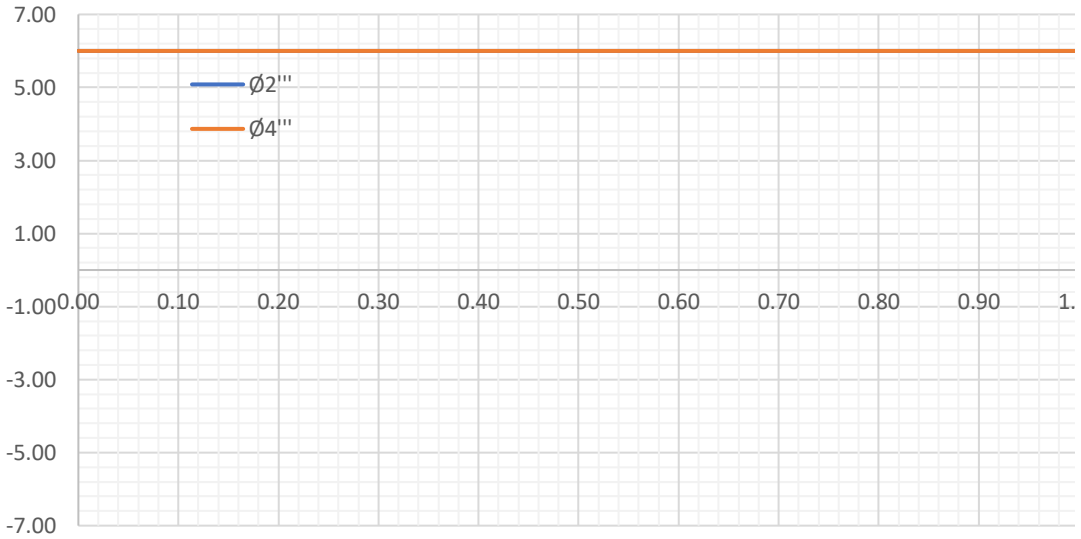

Figure 3-14. Graph of shape factors $\boldsymbol{\phi'''_2}$ and $\boldsymbol{\phi'''_4}$

3.10 Boundary Terms

In equation

(85), the boundary terms are further analyzed.

$$\left[E.I(x)\left(\frac{d^3u}{dx^3}+\frac{d^2u}{dx^2}\right)\right]_0^l \tag{114}$$

In equation (114), $\left[E.I(x)\left(\frac{d^3u}{dx^3}\right)\right]_0^l$ is the applied shear force at the boundary nodes and $\left[E.I(x)\left(\frac{d^2u}{dx^2}\right)\right]_0^l$ is the applied bending moment at the boundary nodes.

The applied joint forces are expressed form as:

$$F_{Jt}=\begin{bmatrix}F_{1v}\\F_{2m}\\F_{3v}\\F_{4m}\end{bmatrix} \tag{115}$$

Equation

(85) can be expressed as:

$$\int_0^l F dx=\int_{x1}^{x2}F_1dx+\int_{x2}^{x3}F_2dx+\cdots+\int_{xn-1}^{xn}F_ndx \tag{116}$$

Rewriting the above equation,

$$\int_0^l F dx = \sum_{i=1}^{m} F_i dx \tag{117}$$

where,

m is the number of elements

From equation

(85),

let,

$$K = \sum_{i=1}^{m} \left(\int_{xi}^{xj} \frac{d^2}{dx^2} w(x).E.I(x) \frac{d^2}{dx^2} u. \right) dx \tag{118}$$

where,

K is the stiffness matrix

$$M = \sum_{i=1}^{m} \left(\int_{xi}^{xj} \left(m(x).w(x).E.I(x) \frac{d^2}{dt^2} u(x,t) \right) dx \right) \tag{119}$$

where,

M is the mass matrix

$$C = \sum_{i=1}^{m} \left(\int_{xi}^{xj} \left(\left(c_p + c_s \right).w(x).E.I(x) \frac{d^2}{dx^2} u(x,t) \right) dx \right) \tag{120}$$

where,

C is the damping matrix

$$S = \sum_{i=1}^{m} \left(\int_{xi}^{xj} \left(\left(s(x) \right). w(x). u(x,t) \right) dx \right) \quad (121)$$

where,

S is the element soil spring matrix

$$F = \sum_{i=1}^{m} \left(\int_{xi}^{xj} \left(w(x). f(t) \right) dx \right) \quad (122)$$

where,

F is the applied element member force matrix

3.11 Member Properties

Let,

d_{pb} = diameter of pole at the base of the pole

d_{pt} = diameter of pole at tip of the pole

l_{pb} = length of the pole

3.12 Element Stiffness Matrix

In this section, the stiffness matrix for an element will be formulated. Equation (118) will be used to derive each element of the element matrix. The integral computation for the elements of the stiffness was performed using Mathcad.

$$k_{11} = E.I.\int_0^h \phi''_1.\phi''_1 dx = \frac{12}{h^3} \tag{123}$$

$$k_{12} = E.I.\int_0^h \phi''_1.\phi''_2 dx = \frac{6}{h^2} \tag{124}$$

$$k_{13} = E.I.\int_0^h \phi''_1.\phi''_3 dx = -\frac{12}{h^3} \tag{125}$$

$$k_{14} = E.I.\int_0^h \phi''_1.\phi''_4 dx = \frac{6}{h^2} \tag{126}$$

$$k_{21} = E.I.\int_0^h \phi''_2.\phi''_1 dx = \frac{12}{h^2} \tag{127}$$

$$k_{22} = E.I.\int_0^h \phi''_2.\phi''_2 dx = \frac{4}{h} \tag{128}$$

$$k_{23} = E.I.\int_0^h \phi''_2.\phi''_3 dx = -\frac{6}{h^2} \tag{129}$$

$$k_{24} = E.I.\int_0^h \phi''_2.\phi''_4 dx = \frac{2}{h} \tag{130}$$

$$k_{31} = E.I.\int_0^h \phi''_3.\phi''_1 dx = -\frac{12}{h^3} \quad (131)$$

$$k_{32} = E.I.\int_0^h \phi''_3.\phi''_2 dx = -\frac{6}{h^2} \quad (132)$$

$$k_{33} = E.I.\int_0^h \phi''_3.\phi''_3 dx = \frac{12}{h^3} \quad (133)$$

$$k_{34} = E.I.\int_0^h \phi''_3.\phi''_4 dx = -\frac{6}{h^2} \quad (134)$$

$$k_{41} = E.I.\int_0^h \phi''_4.\phi''_1 dx = \frac{6}{h^2} \quad (135)$$

$$k_{42} = E.I.\int_0^h \phi''_4.\phi''_2 dx = \frac{2}{h} \quad (136)$$

$$k_{43} = E.I.\int_0^h \phi''_4.\phi''_3 dx = \frac{6}{h^2} \quad (137)$$

$$k_{44} = E.I.\int_0^h \phi''_4.\phi''_4 dx = \frac{4}{h} \quad (138)$$

The element of the stiffness computed above in a matrix is shown below in equation (139).

$$K = E.I_{av}.\begin{bmatrix} k_{11} & k_{11} & k_{11} & k_{11} \\ k_{11} & k_{11} & k_{11} & k_{11} \\ k_{11} & k_{11} & k_{11} & k_{11} \\ k_{11} & k_{11} & k_{11} & k_{11} \end{bmatrix} \quad (139)$$

$$= \frac{E.I_{av}}{h^3}.\begin{bmatrix} 12 & 6h & -12 & 6h \\ 6h & 4h^2 & -6h & 2h^2 \\ -12 & -6h & 12 & -6h \\ 6h & 2h^2 & -6h & 4h^2 \end{bmatrix}$$

Equation (139) is called the consistent stiffness matrix since it is based on the shape functions for the corresponding displacements.

where,

I_{av} is the average 2nd moment of area of inertia of the pole section.

I_{av} is taken as the average value of the moment of inertia between a tapered section's top and bottom sections.

3.13 Element Mass Matrix

The elements of the mass matrix are computed using equation (119). As in the case of the element stiffness matrix, the integrals are evaluated using Mathcad.

$$m_{11} = m_{av}\int_0^h \phi_1.\phi_1 dx = \frac{13h}{35} \tag{140}$$

$$m_{12} = m_{av}\int_0^h \phi_1.\phi_2 dx = \frac{11h^2}{210} \tag{141}$$

$$m_{13} = m_{av}\int_0^h \phi_1.\phi_3 dx = \frac{9h}{70} \tag{142}$$

$$m_{14} = m_{av}\int_0^h \phi_1.\phi_4 dx = -\frac{13h^2}{420} \quad (143)$$

$$m_{21} = m_{av}\int_0^h \phi_2.\phi_1 dx = \frac{11h^2}{210} \quad (144)$$

$$m_{22} = m_{av}\int_0^h \phi_2.\phi_2 dx = \frac{h^3}{105} \quad (145)$$

$$m_{23} = m_{av}\int_0^h \phi_2.\phi_3 dx = \frac{13h^2}{420} \quad (146)$$

$$m_{24} = m_{av}\int_0^h \phi_2.\phi_4 dx = -\frac{h^3}{140} \quad (147)$$

$$m_{31} = m_{av}\int_0^h \phi_3.\phi_1 dx = \frac{9h}{70} \quad (148)$$

m_{32} (149)

$$= m_{av}\int_0^h \phi_3.\phi_2 dx$$

$$= \frac{13h^2}{140}$$

m_{33} (150)

$$= m_{av}\int_0^h \phi_3.\phi_3 dx$$

$$= \frac{13h}{35}$$

$$m_{34} = m_{av}\int_0^h \phi_3.\phi_4 dx = -\frac{11h^2}{210} \quad (151)$$

$$m_{41} = m_{av}\int_0^h \phi_4.\phi_1 dx = -\frac{13h^2}{420} \quad (152)$$

$$m_{42} = m_{av}\int_0^h \phi_4.\phi_2 dx = -\frac{h^3}{140} \quad (153)$$

$$m_{42} \quad (154)$$

$$= m_{av}\int_0^h \phi_4.\phi_2 dx$$

$$= \frac{h^3}{140}$$

$$m_{43} \quad (155)$$

$$= m_{av}\int_0^h \phi_4.\phi_3 dx$$

$$= -\frac{11h^2}{210}$$

$$m_{44} = m_{av}\int_0^h \phi_4.\phi_4 dx = \frac{h^3}{105} \quad (156)$$

Assembling the element mass matrices into a matrix form to get:

$$M = m_{av}.\begin{bmatrix} m_{11} & m_{12} & m_{13} & m_{14} \\ m_{21} & m_{22} & m_{23} & m_{24} \\ m_{31} & m_{32} & m_{33} & m_{34} \\ m_{41} & m_{42} & m_{43} & m_{44} \end{bmatrix} \quad (157)$$

$$= \frac{m_{av}h}{420} \cdot \begin{bmatrix} 156 & 22h & 54 & -13h \\ 22h & 4h^2 & 13h & -3h^2 \\ 54 & 13h & 156 & -22h \\ -13h & -3h & -22h & 4h^2 \end{bmatrix}$$

Equation (157) is also called the consistent mass matrix since it is based on the shape function for the corresponding displacements.

3.14 Damping Matrix

3.15 Consistent Damping Matrix

The elements of the damping matrix are computed using equation

(120). As in the case of the element stiffness matrix, the integrals are evaluated using Mathcad.

Note:

The derivation of the damping matrix is only a classical exercise since the damping matrix is dependent on the mass and stiff matrix. The damping matrix based on the mass and stiffness matrix will be derived in the next section.

$$c_{11} = c. \int_0^h \phi_1 . \phi_1 dx = \frac{13h}{35} \quad (158)$$

$$c_{12} = c. \int_0^h \phi_1 . \phi_2 dx = \frac{11h^2}{210} \quad (159$$

$$c_{13} = c.\int_0^h \phi_1.\phi_3 dx = \frac{9h}{70} \quad (160)$$

$$c_{14} = c.\int_0^h \phi_1.\phi_4 dx = -\frac{13h^2}{420} \quad (161)$$

$$c_{21} = c.\int_0^h \phi_2.\phi_1 dx = \frac{11h^2}{210} \quad (162)$$

$$c_{22} = c.\int_0^h \phi_2.\phi_2 dx = \frac{h^3}{105} \quad (163)$$

$$c_{23} = c.\int_0^h \phi_2.\phi_3 dx = \frac{13h^2}{420} \quad (164)$$

$$c_{24} = c.\int_0^h \phi_2.\phi_4 dx = -\frac{h^3}{140} \quad (165)$$

$$c_{31} = c.\int_0^h \phi_3.\phi_1 dx = \frac{9h}{70} \quad (166)$$

$$c_{32} = c.\int_0^h \phi_3.\phi_2 dx = \frac{13h^2}{420} \quad (167)$$

$$c_{33} = c.\int_0^h \phi_3.\phi_3 dx = \frac{13h}{35} \quad (168)$$

$$c_{34} = c.\int_0^h \phi_3.\phi_4 dx = -\frac{11h}{210} \tag{169}$$

$$c_{41} = c.\int_0^h \phi_4.\phi_1 dx = \frac{13h^2}{420} \tag{170}$$

$$c_{42} = c.\int_0^h \phi_4.\phi_2 dx = -\frac{h^3}{140} \tag{171}$$

$$c_{43} = c.\int_0^h \phi_4.\phi_3 dx = -\frac{11h^2}{210} \tag{172}$$

$$c_{44} = c.\int_0^h \phi_4.\phi_4 dx = \frac{h^4}{105} \tag{173}$$

Assembling the element-damping matrices into a matrix form

$$C = c.\begin{bmatrix} c_{11} & c_{12} & c_{13} & c_{14} \\ c_{21} & c_{22} & c_{23} & c_{24} \\ c_{31} & c_{32} & c_{33} & c_{34} \\ c_{41} & c_{42} & c_{43} & c_{44} \end{bmatrix} \tag{174}$$

$$= \frac{(c_p + c_s)h}{420}.\begin{bmatrix} 156 & 22h & 54 & -13h \\ 22h & 4h^2 & 13h & -3h^2 \\ 54 & 13h & 156 & -22h \\ -13h & -3h & -22h & 4h^2 \end{bmatrix}$$

where,

c_p is the damping co-efficient of the pole material.

and,

c_s is the damping co-efficient of the soil.

3.16 Raleigh's Damping

The damping in a structure is a function of mass and stiffness. Hence, the damping matrix will be formulated based on the following assumption,

$$[C] = \alpha.[M] + \beta.[K] \tag{175}$$

$$=[[M] \quad [K]] \begin{bmatrix} \alpha \\ \beta \end{bmatrix}$$

where,

$[C]$ is the damping matrix

$[K]$ is the stiffness matrix

α is the constant to be determined

β is a factor to be determined

$$c = \alpha m + \beta k \tag{176}$$

Substituting $c = 2\xi m\omega$ and $k = m\omega^2$ into equation (**Error! Reference source not found.**) to get

$$2\xi m\omega = \alpha m + \beta m\omega^2 \tag{177}$$

$$\xi = \frac{1}{2}\alpha 1\omega + \beta\omega \tag{178}$$

$$\xi_1 = \frac{1}{2}\left\{\alpha\frac{1}{\omega_1} + \beta\omega_1\right\}$$

In matrix form, equation (179) can be written as

$$\begin{bmatrix}\alpha\\ \beta\end{bmatrix} = 2\begin{bmatrix}\frac{1}{\omega_1} & \omega_1\\ \frac{1}{\omega_2} & \omega_2\end{bmatrix}^{-1}\begin{bmatrix}\xi_1\\ \xi_2\end{bmatrix} \tag{180}$$

Substituting equation (180) into (175),

$$\begin{bmatrix}\xi_1\\ \xi_2\end{bmatrix} = \frac{1}{2}\begin{bmatrix}\frac{1}{\omega_1} & \omega_1\\ \frac{1}{\omega_2} & \omega_2\end{bmatrix}\begin{bmatrix}\alpha\\ \beta\end{bmatrix} \tag{181}$$

Equation (182) will be used to formulate the damping matrix for a multi- degree of freedom systems or elements. Damping ratios vary depending on the wood species, age, physical dimensions, preservative treatment types, and pole conditions. Typical values of damping will range from 3% to 15%.

$$[C] = [[M] \quad [K]](2)\begin{bmatrix}\frac{1}{\omega_1} & \omega_1\\ \frac{1}{\omega_2} & \omega_2\end{bmatrix}^{-1}\begin{bmatrix}\xi_1\\ \xi_2\end{bmatrix} \tag{182}$$

3.17 Lateral Vertical Soil Spring Stiffness of Sandy, Clayey Soils, and Rock

In this section, the vertical and horizontal soil spring stiffnesses for soils and rock is discussed. The soil stiffness behavior will differ for cohesionless, cohesive soil, and rock since the pressure distribution depends on the soil type.

A method to compute the soil springs for clayey and sandy soil proposed by Bohnhoff [17] is used for this study. A typical load displacement curve is in Figure 3-15, reproduced from [17].

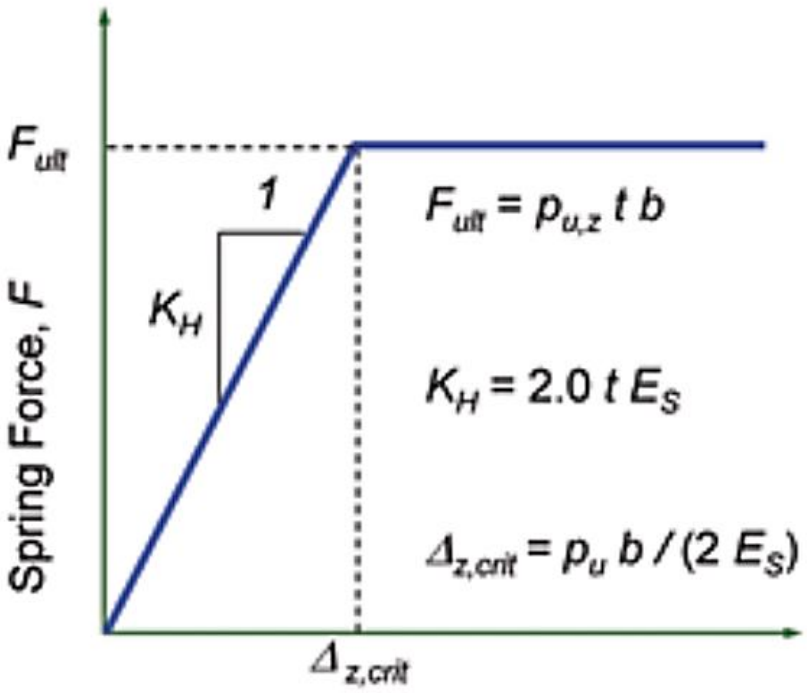

Figure 3-15. Load-Displacement Relationship for a Soil Spring

The inertial lateral stiffness, K_h of an individual soil spring is given by

$$K_h = 2.0\ t\ E_s \quad (183)$$

where

t is the thickness of the soil layer between the soil springs

E_s is the Young's Modulus of soil at depth z.

Es is constant with depths for clayey soils and varies linearly with depth for sandy soils.

Es value for sandy soils vary with depth, hence

where

$$E_{S,z} = A_z.z \quad (184)$$

$E_{S,z}$ = Es that is zero at ground level and increases linearly with depth z below grade.

A_z = increase in Young's Modulus per unit increase in depth z below ground.

z = depth below ground.

3.17.1 Soil Spring Ultimate Strength

The ultimate lateral load capacity of a soil spring is given by:

where

$$F_{ult} = p_{u,z}tb \quad (185)$$

F_{ult} = ultimate load capacity of a spring at depth z

$p_{u,z}$ = ultimate lateral soil resistance of soil at depth z

b = average width or diameter of pole at depth z

t = thickness of the soil layer, or spacing of the soil springs

for sandy soils,

$p_{u,z} = 3\sigma'_{v,z}K_p$

for clayey soils,

$p_{u,z} = 3S_U\left(1 + \frac{z}{2b}\right)\ for\ 0 < z < 4b$

$p_{u,z} = 9S_U \qquad for > 4b$

where

K_p = passive earth pressure co-efficient

$= \frac{1+sin\emptyset}{1-sin\emptyset}$

$\sigma'_{v,z}$ = effective vertical stress at depth z

$= \gamma z - u_z$

γ = moist unit weight of soil

u_z = pore water pressure at depth z

S_U = undrained soil shear strength for saturated clayey soil

3.17.2 Critical Soil Displacement

The load displacement curve is linear up the critical soil displacement, and plastic beyond the critical displacement. The critical displacement is given by

$$\Delta_{z,crit} = p_{u,z} tb \tag{186}$$

3.18 Vertical Spring Stiffness of Sandy, Clayey soils, and Rock

The vertical spring stiffness of soils is given by

$$K_z = (\frac{1}{3}) b\gamma z^2 \tag{187}$$

where

K_z = vertical spring stiffness [F/L]

b, γ, and z are defined in previous section 3.17.1

3.19 Soil Spring Stiffness Matrix

In section 3.17, the expressions for lateral and vertical soil springs were developed. In this section, the soil springs will be expressed in a matrix form for each element. A sketch of a linear spring is shown in Figure 3-16. The linear spring has one degree of freedom at each node. The rotational spring stiffness is ignored in this study.

The expression for the spring force-stiffness-displacement relationship for a soil spring element with a single degree of freedom is given by

$$(f_s) = \begin{bmatrix} k & -k \\ -k & k \end{bmatrix} \begin{pmatrix} x_1 \\ x_2 \end{pmatrix} \quad (188)$$

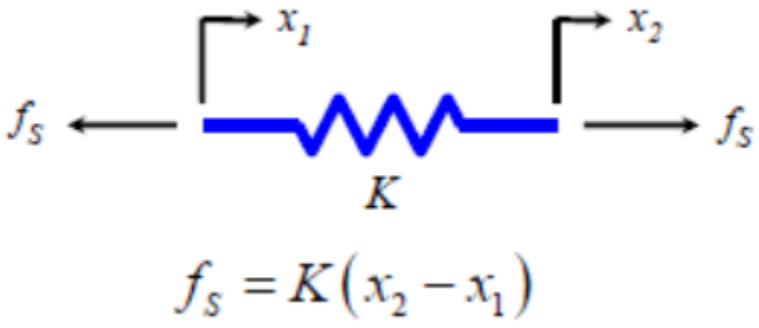

Figure 3-16. Sketch of Linear Spring

where

f_s = force in the spring [F]

x_1, x_2= axial displacement in the direction of force at the beginning and end nodes [L]

k = is the string constant [F/L]

The matrix for the spring element with 3-Degrees-of-freedom at each end, can be expressed as

$$(f_s) = [K_s](u) \quad (189)$$

$$(f_s) = \begin{bmatrix} k_x & 0 & 0 & -k_x & 0 & 0 \\ 0 & k_y & 0 & 0 & -k_y & 0 \\ 0 & 0 & k_z & 0 & 0 & 0 \\ -k_x & 0 & 0 & k_x & 0 & -k_z \\ 0 & -k_y & 0 & 0 & k_y & 0 \\ 0 & 0 & -k_z & 0 & 0 & k_z \end{bmatrix} \begin{pmatrix} u_1 \\ u_2 \\ u_3 \\ u_4 \\ u_5 \\ u_6 \end{pmatrix} \quad (190)$$

where

(f_s) = Spring force matrix

$[K_s]$ = Spring stiffness matrix

(u) = joint displacement matrix

In equations (189) and (190) $[K_s]$ is the nodal soil stiffness matrix for the soil.

3.20 Numerical Integration of Time History Test Records

This section presents the numerical procedure and technique to obtain velocity and displacements from test acceleration records.

let,

a1 and a2 be the acceleration at time t1 and t2 respectively.

We assume a linear variation of acceleration between the times t1 and t2. This can be expressed as:

$$a(t) = \mathrm{b0} + \mathrm{b1}.\,\mathrm{t} \tag{191}$$

Where b_0 and b_1 are arbitrary constants that need to be determined.

This equation can be expressed in a matrix form

$$a(t) = [1 \quad t].\begin{bmatrix} b0 \\ b1 \end{bmatrix} \tag{192}$$

Applying the known accelerations at times t1 and t2 to get

$$a1 = \mathrm{b0} + \mathrm{b1}.\,\mathrm{t1} \tag{193}$$

$$a2 = \mathrm{b0} + \mathrm{b1}.\,\mathrm{t2}$$

We solve the above two equations using matrices,

$$\begin{bmatrix} a_1 \\ a_2 \end{bmatrix} = \begin{bmatrix} 0 & t_1 \\ 0 & t \end{bmatrix} \begin{bmatrix} b_0 \\ b_1 \end{bmatrix} \tag{194}$$

Solving for b_0 and b_1 to get

$$\begin{bmatrix} b_0 \\ b_1 \end{bmatrix} = \begin{bmatrix} 0 & t_1 \\ 0 & t \end{bmatrix}^{-1} \begin{bmatrix} a_1 \\ a_2 \end{bmatrix} \tag{195}$$

Substituting equation (195) into equation (192) to get,

$$a(t) = \begin{bmatrix} 1 & t \end{bmatrix} \begin{bmatrix} 0 & t_1 \\ 0 & t \end{bmatrix}^{-1} \begin{bmatrix} a_1 \\ a_2 \end{bmatrix} \tag{196}$$

$$a(t) = \begin{bmatrix} (1 - \frac{t}{\Delta t}) & (\frac{t}{\Delta t}) \end{bmatrix} \begin{bmatrix} a_1 \\ a_2 \end{bmatrix} \tag{197}$$

$$a(t) = \begin{bmatrix} \emptyset_1 & \emptyset_2 \end{bmatrix} \begin{bmatrix} a_1 \\ a_2 \end{bmatrix} \tag{198}$$

$$a(t) = \emptyset_1 a_1 + \emptyset_2 a_2 \tag{199}$$

where,

$$\emptyset_1 = (1 - \frac{t}{\Delta t})$$

And,

$$\emptyset_2 = \frac{t}{\Delta t}$$

Similarly, the equation for velocity is,

$$v(t) = \emptyset_1 v_1 + \emptyset_2 v_2$$

3.20.1 Velocity

Similarly, the equation for acceleration is given by the rate of change of velocity with respect to time.

$$a = \frac{dv}{dt} \tag{200}$$

Rearranging the above equation to get

$$adt - dv = 0 \tag{201}$$

Substituting equation (197) into (201),

$$\left(1 - \frac{t}{\Delta t}\right) a_1 + \left(\frac{t}{\Delta t}\right) a_2 - dv = 0 \tag{202}$$

$$\int_0^{\Delta t} \left(1 - \frac{t}{\Delta t}\right) a_1 + \left(\frac{t}{\Delta t}\right) a_2 + \int_{v_1}^{v_2} dv = 0 \tag{203}$$

Solving equation (203) to get

$$v_2 - v_1 - \frac{\Delta t a_1}{2} - \frac{\Delta t a_2}{2} = 0 \tag{204}$$

$$v_2 = v_1 + \frac{\Delta t a_1}{2} + \frac{\Delta t a_2}{2} \tag{205}$$

The term $(a_1 + a_2)/2$ is the average acceleration, therefore, equation (205) becomes,

$$v_2 = v_1 + \frac{1}{2}(a_1 + a_2)\Delta t \tag{206}$$

3.21 Displacement

Velocity is the rate of change of distance with respect to time.

$$v = \frac{ds}{dt} \tag{207}$$

$$vdt - dv = 0 \tag{208}$$

Substituting the equation for v, we get

$$\left(1 - \frac{t}{\Delta t}\right) v_1 + \left(\frac{t}{\Delta t}\right) v_2 + \Delta t \left(\frac{a_1 + a_2}{2}\right) dt = ds \tag{209}$$

Rearranging and integrating equation (209),

Solving equation (210), we get

$$\int_0^{\Delta t}\left(1-\frac{t}{\Delta t}\right)v_1+\left(\frac{t}{\Delta t}\right)v_2+\Delta t\left(\frac{a_1+a_2}{2}\right)dt-\int_{s_1}^{s_2}ds=0 \tag{210}$$

$$s_2=s_1+\left(\frac{v_1+v_2}{2}\right)\Delta t+\ \Delta t^2\left(\frac{a_1+a_2}{2}\right) \tag{211}$$

In summary, the velocity and displacement are given by equations (206) and (211) for a given value of accelerations and initial conditions. This forms the basis of the numerical integration of a set of acceleration records to obtain displacements and velocities.

3.21.1 Non-Linear Soil Displacement Curve

Clayey and Sandy soils exhibits non-linear load-displacement response when the applied load exceeds its ultimate load capacity. A typical load-displacement curve is shown in Figure 3-17.

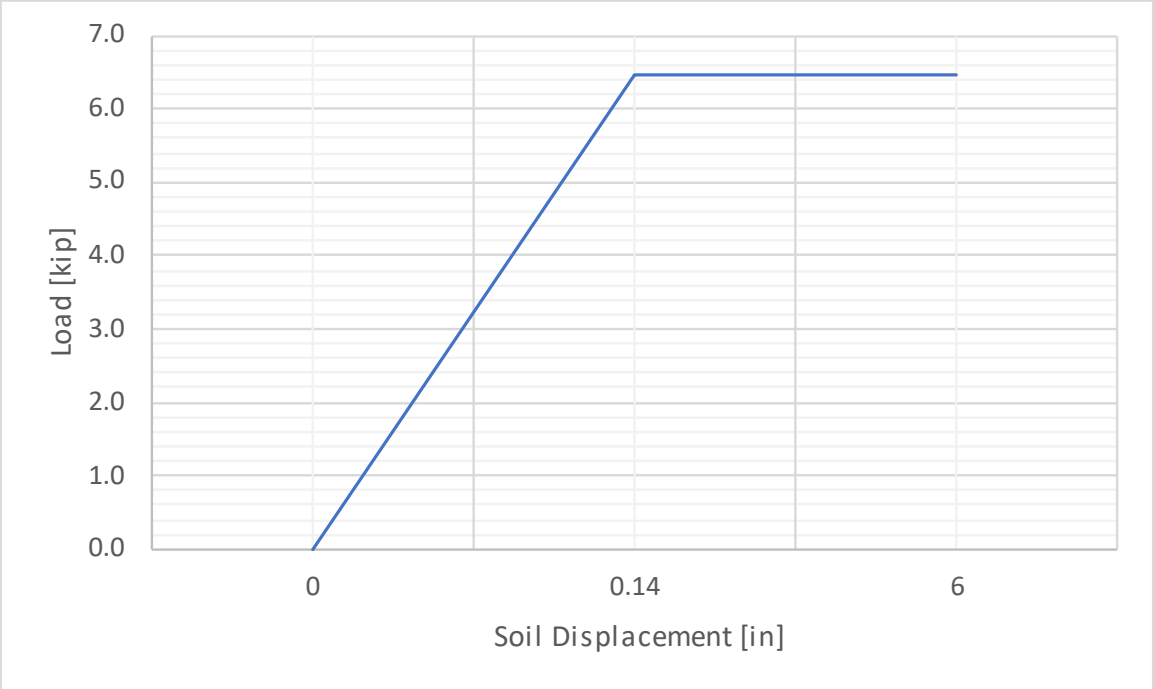

Figure 3-17. Aassumed Non-Linear Soil Load Displacement Curve

3.22 Tuned Mass Damper (TMD)

This section presents a proposed Tuned Mass Damper (TMD) solution to mitigate the effect of the resonance on poles subject to dynamic wind forces at resonance frequencies. The Tuned Mass Damper consists of a steel rod with a spherical steel ball attached to the top of the steel rod. The Tuned Mass Damper is mounted securely on top of the wood pole.

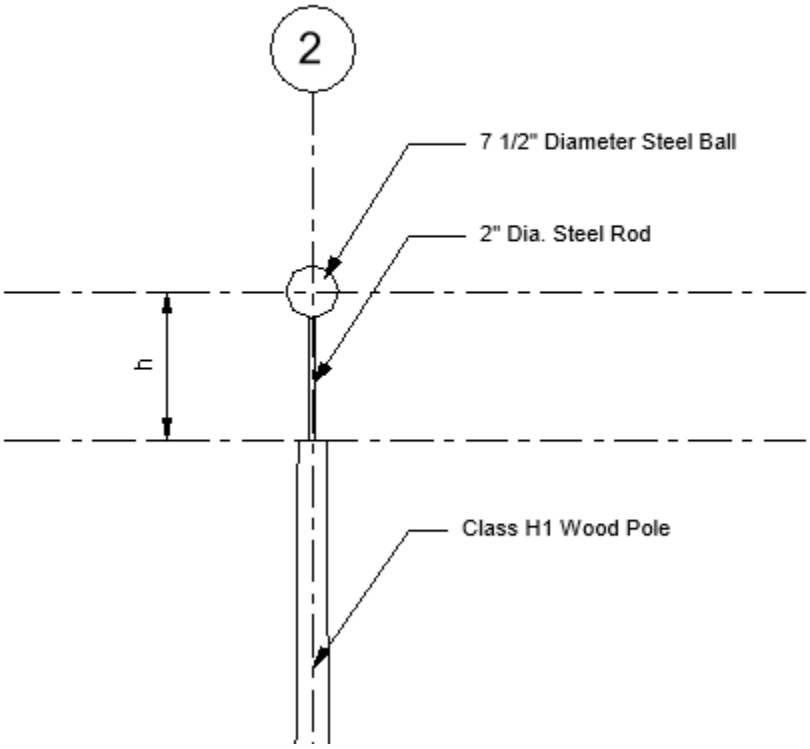

Figure 3-18. Sketch of TMD on Class H1 Wood Pole

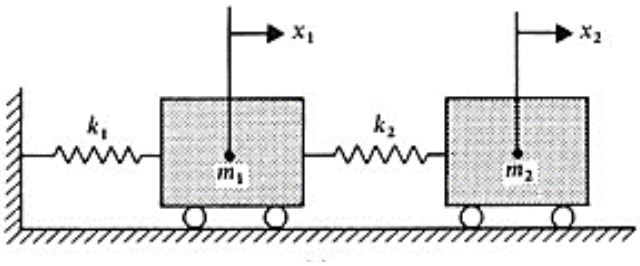

Figure 3-19. Two Degree of Freedom TMD system

In Figure 3-19, $m_1$is the effective mass of the pole, m_2 is the mass of the Tuned mass damper.

The pole and TMD can be modeled as a lumped mass-spring system, as shown in Figure 3-18 and Figure 3-19

The spring-mass system is represented by equation (212)

$$[m]\{\ddot{u}\} + [k]\{u\} = 0 \tag{212}$$

For a 2-Degree of freedom mass-spring system, the equations are written in a matrix form as shown in equation (213) below.

$$\begin{bmatrix} m_1 & 0 \\ 0 & m_2 \end{bmatrix} + \begin{bmatrix} k_1 + k_2 & -k_2 \\ -k_2 & k_2 \end{bmatrix} = \begin{bmatrix} 0 \\ 0 \end{bmatrix} \tag{213}$$

Let, $\frac{m_2}{m_1} = m_r$, where m_r is the ratio of mass of Tuned Mass Damper to effective mass of the pole, or the mass ratio.

Let, $\frac{k_2}{k_1}$ =ρ, where ρ is the ratio of stiffness of Tuned Mass Damper to stiffness of the pole or the stiffness ratio.

Substituting the expressions $\frac{m_2}{m_1} = m_r$, and $\frac{k_2}{k_1}$ =ρ, into (213), we get

$$\begin{bmatrix} m_1 & 0 \\ 0 & m_1.m_r \end{bmatrix} + \begin{bmatrix} k_1 + k_1.\rho & -k_1.\rho \\ -k_1.\rho & k_1.\rho \end{bmatrix} = \begin{bmatrix} 0 \\ 0 \end{bmatrix} \tag{214}$$

$$\mathrm{m}_1\begin{bmatrix}1 & 0\\ 0 & \mathrm{m}_r\end{bmatrix}+\mathrm{k}_1\begin{bmatrix}(1+\rho) & -\rho\\ -\rho & \rho\end{bmatrix}=\begin{bmatrix}0\\ 0\end{bmatrix}$$

Simplifying the above equation, we get

$$\begin{bmatrix}1 & 0\\ 0 & m_r\end{bmatrix}+\frac{k_1}{m_1}\begin{bmatrix}(1+\rho) & -\rho\\ -\rho & \rho\end{bmatrix}=\begin{bmatrix}0\\ 0\end{bmatrix}$$

k_1 is given by the expression

$$k_1 = m_1.\omega_1^2$$

where ω_1 is the effective circular natural frequency, and m_1 is the effective mass of the pole.

$$\begin{bmatrix}1 & 0\\ 0 & m_r\end{bmatrix}+\omega_1^2.\begin{bmatrix}(1+\rho) & -\rho\\ -\rho & \rho\end{bmatrix}=\begin{bmatrix}0\\ 0\end{bmatrix} \quad (215)$$

Equation (215) is the equation of motion for a two degree of freedom spring mass damper. The equation is solved for the eigen values, and vectors for a given effective mass, and stiffness ratio, and natural frequency.

CHAPTER IV

4 DISCUSSION OF RESULTS

The results from experimental and theoretical analysis are discussed in this section. A summary of the test results for the natural frequencies of the test poles presented in section 4.1, followed by comparison of the dynamic properties of the test pole with theoretical computations. The mechanical properties of the test pole species, Young's Modulus, unit weight, and bending stress obtained experimentally are presented shown in section 2.7, and 2.3.6.

In section 4.3, the natural frequency response for a class H1 pole embedded in sandy, clayey and rock is discussed. The ground and pole tip displacement response of the wood utility poles subject to static wind loads, and non-linear soil stiffness are discussed in section 4.4, and 4.5. Potential pole failures due to excessive ground, and pole tip displacements, including pole breakage from bending are presented.

The cable mass ratio affects the natural frequency of the pole system. A detailed discuss on the effect of the cable mass ratio of the test poles, and the class H1 pole is discussed in section 4.7, and 4.10.

Resonace in cantilever pole structures occur the frequency of wind matches the natural frequency of the pole. The results of the resonance displacement amplification for poles embedded in sandy and clayey soils are discussed in section 4.9. Mitigation of large displacement amplifications using a Tuned Mass Damper is discussed in section 4.11.

4.1 Dynamics Response to Initial Static Pull

The results from experimental data together with the natural periods, frequencies, and damping ratios for the test specimens are shown in Table 2-7, Table 2-8, and Table 2-9. Table 4-1 shows the summary of the mean dynamic properties of the test specimens.

Table 4-1: Experimentally Computed Dynamic Response

Test Specimen	Test Number	Damping Ratio [%]	Period [sec]	Natural Frequency [Hz]
TSP1	1	2.87	0.047	21.21
	2	1.02	0.046	21.61
TSP2	1	1.07	0.047	21.36
Average		1.64	0.047	21.39

The average natural period and frequencies of the test poles are 0.47s and 21.39Hz, while the average damping ratio is 1.64%.

4.2 Dynamic Response from Analysis

Table 4-2 shows the periods, and natural frequencies obtained using a MATLAB code, analytical solution, and SAP2000 program for a 4’ 0” test specimen.

Table 4-2: Computed Natural Periods and Frequencies

		Fundamental Period [sec]			Fundamental Frequency [Hz]		
S. NO	No. of Element	FEM Analysis Using MATLAB Code (Consistent Mass and Stiffness)	Analytical Solution	FEM Analysis Using SAP2000 (Lumped Mass, and Stiffness)	FEM Analysis Using MATLAB Code (Consistent Mass and Stiffness)	Analytical Solution	FEM Analysis Using MATLAB Code (Consistent Mass and Stiffness)
1	4	0.0341	0.0395	0.0444	29.336	25.340	29.525
2	10	0.0338	0.0395	0.0343	29.565	25.340	29.141
3	25	0.0338	0.0395	0.0342	29.602	25.340	29.268
4	50	0.0338	0.0395	0.0429	29.608	25.340	29.286
5	100	0.0338	0.0395	0.0341	29.609	25.340	29.290

The period and frequency obtained from an analytical solution are based on the average diameter of the test pole. The MATLAB code was written using consistent mass and stiffness matrices. SAP2000 program results are based on lumped mass and stiffness matrix. The number of elements selected are 4, 10, 25, 50, and 100 to compare the MATLAB code and SAP2000 results.

Results from the FEA analysis using consistent mass and stiffness agreed well with the SAP2000 Lumped Mass analysis. However, the natural period and frequency from the analytical solution is 14.4% less than the results from the FEM analysis. An average pole diameter was used to determine the cross-sectional properties of the test specimen for the analytical solution. In contrast, the actual diameter at the nodes was used for the FEM analysis. Both MATLAB code and SAP2000 program utilize FEM analysis.

The experimentally obtained natural frequency for the test specimen and FEM analysis are 21.39Hz, and 29.9Hz. The experimentally obtained natural frequency of the test specimens was 28.5% lower than the theoretical values.

The natural frequencies and periods obtained using the Consistent Mass and Lumped Mass are the same for all practical purposes if a sufficient number of elements are chosen. Hence, either one of the methods would yield similar results.

4.3 Frequency Response of Class H1 Tapered Pole Embedded in Foundation Soils

The response of a class H1 pole embedded in three (3) soil types is discussed in this section. The results are then compared to a class H1 pole with a fixed base to further understand the differences in their responses. The three types of soil considered in this study are sandy soil, clayey soil, and rock. The dimensions of a class H1 wood pole is listed in Appendix F, Section 0. The tip and base diameter of the class H1 pole are 8.7 inches and 14.2 inches, respectively. A 35-foot pole height was chosen with a 25-foot projection above the ground level. The embedment depth was varied from 10ft to 1ft, in 6” decrements, to capture the dynamic response.

The assumed soil spring constants for the considered soils are shown in Table 4-3, Table 4-4, and Table 4-5. In these tables, $A_{E,Z}$, is the elastic modulus of soil as a function of depth, $E_{s,z}$ is the soil elastic modulus at the specified depths, k_h is the lateral spring value (in X- and Y- directions) at the specified depths, and k_z is the vertical spring values (skin friction). These assumed soil parameters are based on the publication “Modelling of Soil Behavior With Simple Springs” by Bohnhoff [17]. The Young’s Modulus of 660 psi/ft and 3930 psi for Sandy and Clayey soils is used in this study. The site-specific Young’s

Modulus of the soil can be obtained from a geotechnical investigation; however, the above values were chosen for this study. The end bearing capacity at the bottom of the pole is also shown in soil properties tables. The additional vertical stiffness at the bottom of the pole is additive to the nodal spring value.

Table 4-3: Soil Spring Constants for Sandy Soil

	The density of Sandy Soil = 110pcf					
S. No	Embedment Depth [ft]	$A_{E,Z}$ [psi]	Es,z [ksi]	k_h [kip/in]	k_z [kip/in]	End Bearing Capacity [kips]
	0	660	0.00	0.01	0.01	-
2	0.5	660	0.33	3.96	0.01	-
3	1	660	0.66	7.92	0.04	-
4	1.5	660	0.99	11.88	0.08	0.130
5	2	660	1.32	15.84	0.15	0.173
6	2.5	660	1.65	19.80	0.23	0.216
7	1	660	1.98	23.76	0.33	0.259
8	3.5	660	2.31	27.72	0.44	0.302
9	4	660	2.64	31.68	0.58	0.346
10	4.5	660	2.97	35.64	0.74	0.389
11	5	660	3.30	39.60	0.91	0.432
12	5.5	660	3.63	43.56	1.10	0.475
13	6	660	3.96	47.52	1.31	0.518
14	6.5	660	4.29	51.48	1.53	0.562
15	7	660	4.62	55.44	1.78	0.605
16	7.5	660	4.95	59.40	2.04	0.648
17	8	660	5.28	63.36	2.32	0.691
18	8.5	660	5.61	67.32	2.62	0.734
19	9	660	5.94	71.28	2.94	0.778
20	9.5	660	6.27	75.24	3.28	0.821
21	10	660	6.60	79.20	3.63	0.864

Table 4-4: Soil Spring Constants for Clayey Soil

	The density of Clayey Soil = 90 pcf					
S. No	Height, [ft]	$A_{E,Z}$ [psi]	$E_{s,z}$ [ksi]	k_h [kip/in]	k_z, [kip/in]	End Bearing Capacity [kips]
1	0	3920	0.00	0.1	0.10	-
2	0.5	3920	1.96	23.52	0.01	-
3	1	3920	1.96	23.52	0.03	-
4	1.5	3920	1.96	23.52	0.07	0.106
5	2	3920	1.96	23.52	0.12	0.141
6	2.5	3920	1.96	23.52	0.19	0.177
7	3	3920	1.96	23.52	0.27	0.212
8	3.5	3920	1.96	23.52	0.36	0.247
9	4	3920	1.96	23.52	0.48	0.283
10	4.5	3920	1.96	23.52	0.60	0.318
11	5	3920	1.96	23.52	0.74	0.353
12	5.5	3920	1.96	23.52	0.90	0.389
13	6	3920	1.96	23.52	1.07	0.424
14	6.5	3920	1.96	23.52	1.25	0.459
15	7	3920	1.96	23.52	1.46	0.495
16	7.5	3920	1.96	23.52	1.67	0.530
17	8	3920	1.96	23.52	1.90	0.565
18	8.5	3920	1.96	23.52	2.15	0.601
19	9	3920	1.96	23.52	2.41	0.636
20	9.5	3920	1.96	23.52	2.68	0.672
21	10	3920	1.96	23.52	2.97	0.707

Table 4-5: Soil Spring Constants for Rock

	Density of Rock = 140pcf					
S. No	Height, [ft]	$A_{E,Z}$ [psi]	$E_{s,z}$ [ksi]	k_h [kip/in]	k_z, [kip/in]	End Bearing Capacity [kips]
1	0	29000	0.00	0	0	-
2	0.5	29000	14.50	174.0	0.14	-
3	1	29000	14.50	174.0	0.55	-
4	1.5	29000	14.50	174.0	1.24	3.927
5	2	29000	14.50	174.0	2.21	3.927
6	2.5	29000	14.50	174.0	3.46	3.927
7	3	29000	14.50	174.0	4.99	3.927
8	3.5	29000	14.50	174.0	6.79	3.927
9	4	29000	14.50	174.0	8.87	3.927
10	4.5	29000	14.50	174.0	11.22	3.927
11	5	29000	14.50	174.0	13.86	3.927
12	5.5	29000	14.50	174.0	16.77	3.927
13	6	29000	14.50	174.0	19.96	3.927
14	6.5	29000	14.50	174.0	23.42	3.927
15	7	29000	14.50	174.0	27.16	3.927
16	7.5	29000	14.50	174.0	31.18	3.927
17	8	29000	14.50	174.0	35.48	3.927
18	8.5	29000	14.50	174.0	40.06	3.927
19	9	29000	14.50	174.0	44.91	3.927
20	9.5	29000	14.50	174.0	50.04	3.927
21	10	29000	14.50	174.0	55.44	3.927

The analysis is performed for the three soil types by varying the embedment depths. The effect of reduction in the soil spring values in the presence of moisture is considered by reducing the soil spring values by 15%, 30%, 50%, and 75%.

The analysis model consisted of 75 elements equally spaced at 6”. SAP2000 was used to perform the modal analysis.

The analysis results were tabulated and compared with the fixed base condition. The dynamic response of the Class H1 pole is then plotted for various depths, together with the responses for various percentages of soil stiffness reduction for comparison. These graphs are shown in Figure 4-1, Figure 4-2, Figure 4-3, Figure 4-5 and Figure 4-6

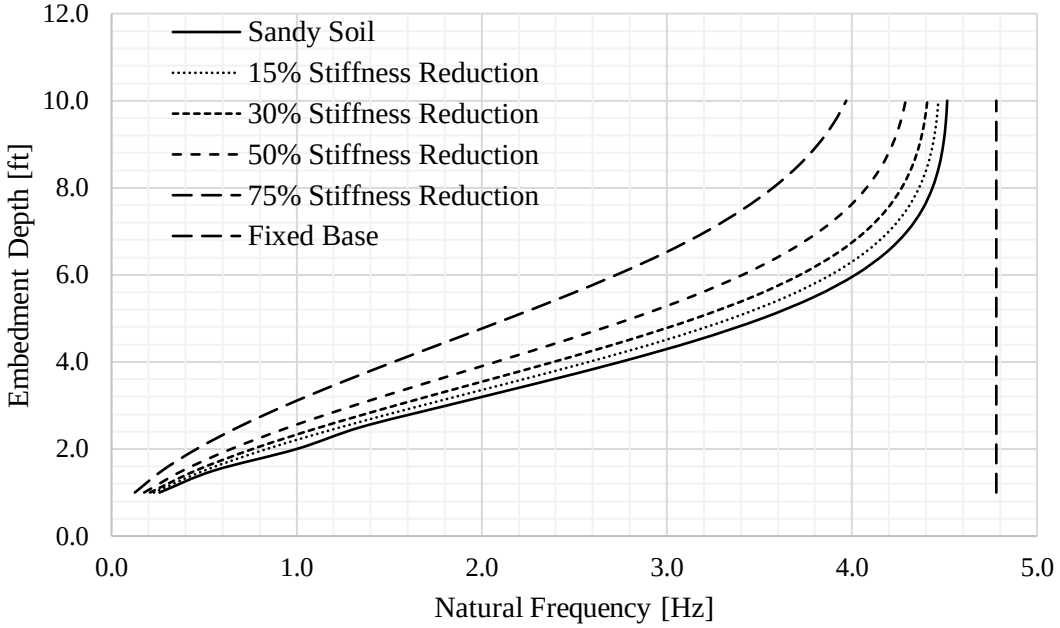

Figure 4-1:. Natural Frequency Response Vs. Embedment Depth [ft] for Sandy Soil

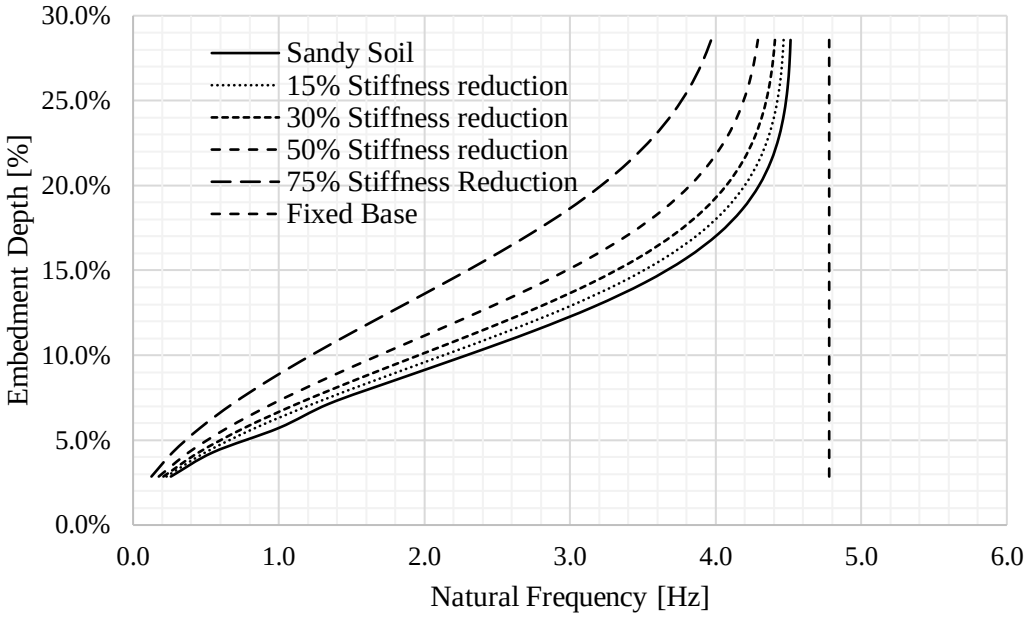

Figure 4-2. Natural Frequency Vs. Percentage Embedment for Sandy Soil

Figure 4-1, and Figure 4-2 show the graph for response frequency vs embedment depths for Sandy Soil. The frequency response below 10% embedment appears to be linear. The curves seem to be non-linear above 10% embedment. The response frequencies for 10% and 15% embedment depths are 2.29Hz and 3.7Hz, respectively. These values represent a 61.69% increase in the natural frequency and a significant increase for a 5% increase in the embedment depth for the assumed standard sandy soil.

The dashed vertical line represents the natural frequency of the class H1 pole with a fixed base of nearly 4.8Hz. The natural frequency graph for the class H1 pole trends vertically for embedment depths greater than 20% and approaches a constant value of 4.6Hz.

The reduction in the soil stiffness reduces the natural frequencies, especially for embedment depths lower than 20%. The 15% embedment depth seems to be the transition point from a linear to non-linear natural frequency response and a practical guide for embedment depths in sandy soils.

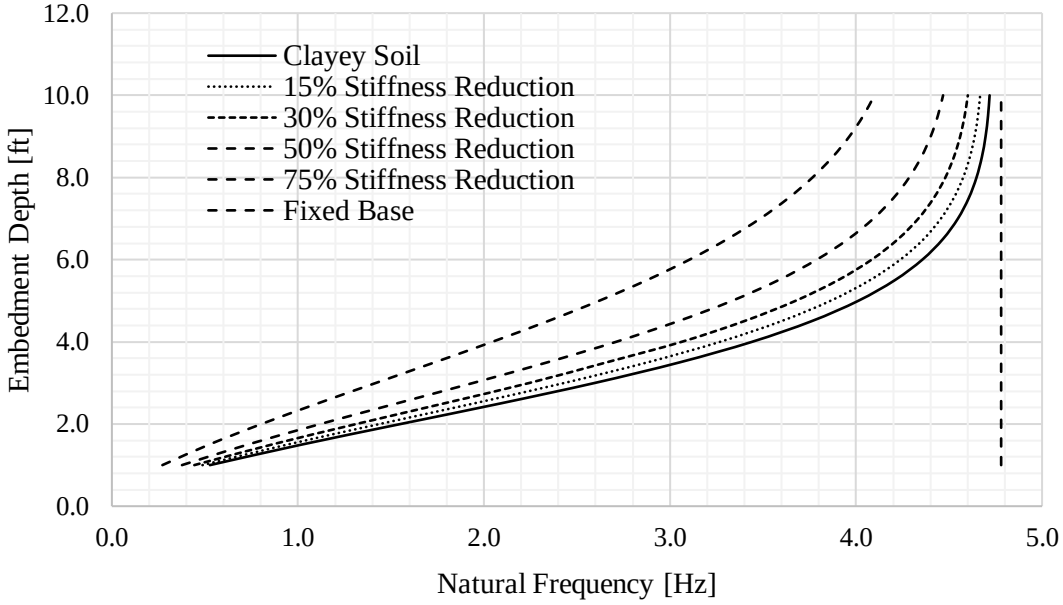

Figure 4-3. Natural Frequency Vs. Embedment Depth [ft] For Clayey Soil

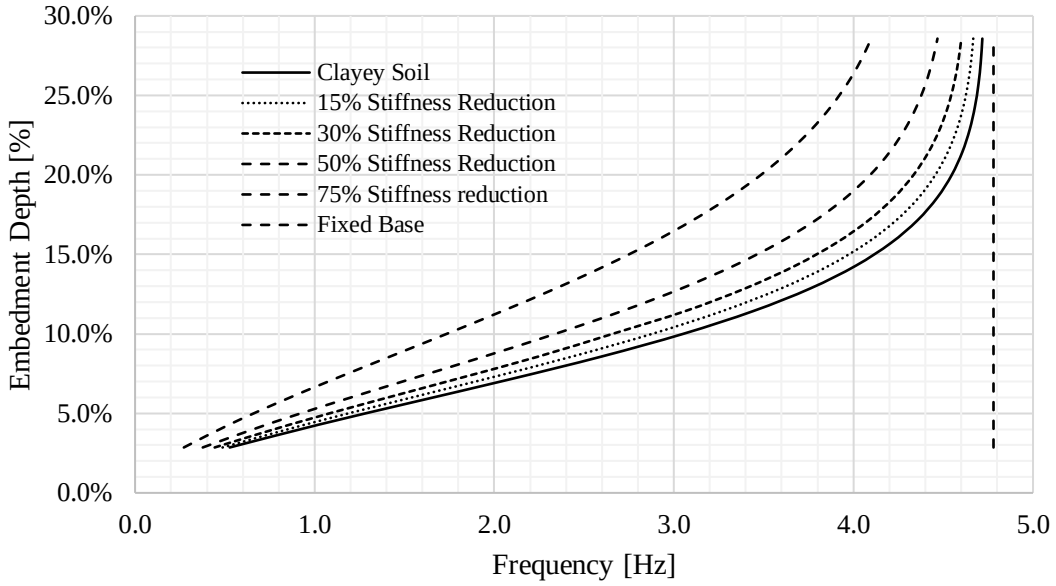

Figure 4-4. Natural Frequency Vs. Embedment Depth [%] For Clayey Soil

Figure 4-3 and Figure 4-4 show the graph for Response Frequency vs. embedment depths for clayey soil. The response frequencies for 15%, 30%, 50%, and 75% reduced soil stiffness also show the effect on the reduced soil stiffness.

The 12.5% embedment depth seems to be where the natural frequency response graph transitions from linear to non-linear. The response frequencies for 10% and 15% embedment are 3.052Hz and 4.2Hz, respectively. These values represent a 37.9% increase in the response frequency for a 5% increase in the embedment depth.

The natural frequency response for clayey soil approaches a constant value of 4.6Hz beyond 20% embedment depths.

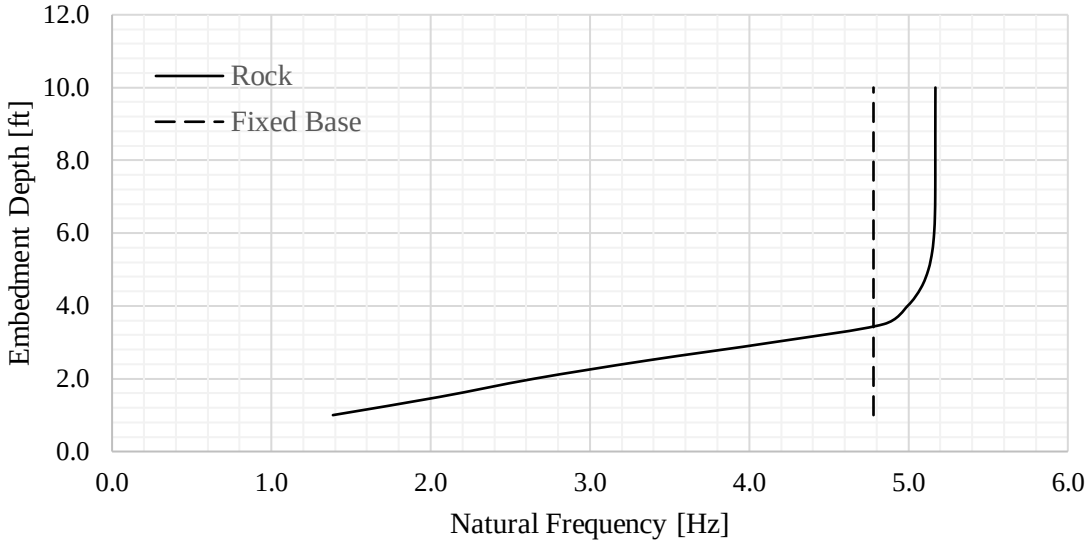

Figure 4-5. Natural Frequency Vs. Embedment Depth for Rock

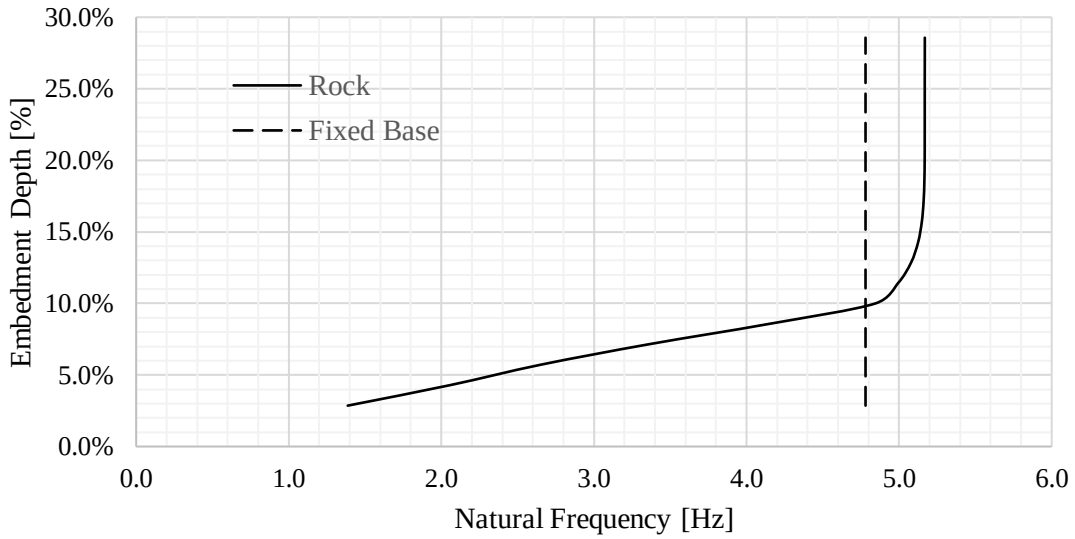

Figure 4-6. Natural Frequency Vs. Percentage Embedment [%] For Rock.

Figure 4-5, and Figure 4-6 show the Response Frequency vs. embedment depth for rock. It can be observed that the response frequencies do not significantly change above 10% embedment depths. Also, moisture does not affect the stiffness properties of rock. The dashed vertical line is the natural frequency response h for a class H1 pole with a fixed base. The natural frequencies are larger for embedment depths greater than 10% than the fixed base. The diameter of the class H1 pole at the fixed base is 12.56 inches. The diameter of the pole base at 10% and 25% embedment depths is 12.94 inches and 13.71 inches, respectively. The stiffness increases with the pole's diameter, hence the larger natural frequency beyond 10% embedment depths.

A 10% embedment depth for rock seems to be the optimal depth limit for practical purposes.

4.4 Ground and Pole Tip Displacement of Class H1 Pole Embedded in Clayey Soil and Subjected to Static Wind Loads.

This section discusses the ground displacement response of the class H1 wood pole with a 100 ft cable subjected to various wind speeds. A non-linear response of the soil is considered. The cable effects of the are also considered in the study. A sketch showing the ½” diameter, 100 ft cable, class H1 wood pole, and non-linear springs is shown in Figure 4-7.

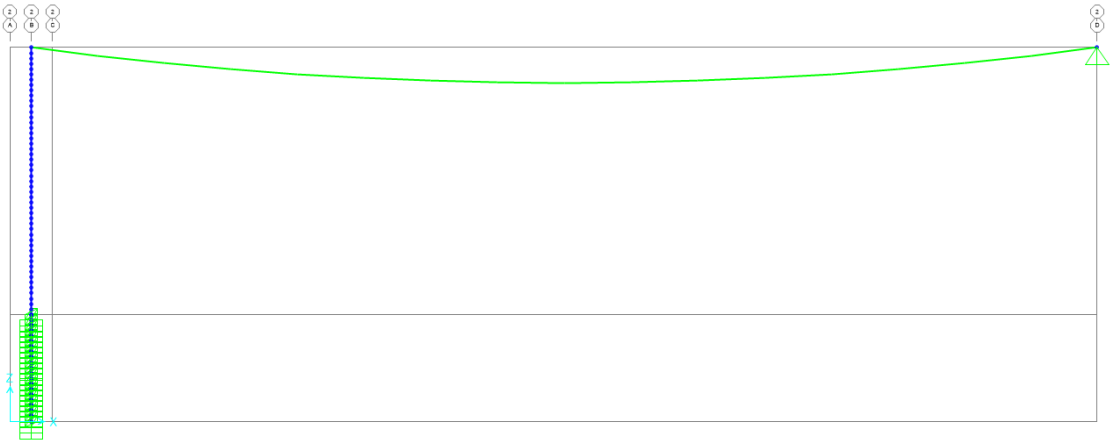

Figure 4-7. Sketch of Soils Springs, Cable, and Wood Pole

The soil spring constants are computed based on the methods proposed by Bohnhoff [17]. The Young's Modulus for clayey of 3920 psi and 660 psi/ft for sand are used. Young's Modulus for clayey soils remains constant over the depth of the soil; however, it increases with depth for sandy soils.

Table 4-6 shows a typical ultimate load and corresponding displacements for Clayey soils.

Table 4-6: Soil Spring Constants and Displacements for Clayey Soil

z [ft]	E_{sz} [psi]	K_h [kip/in]	K_z [kip/in]	F_{ult} [kip]	d_u [in]	d_{umax} [in]
0	1960	0	0	0	0	0
0.5	1960	23.52	0.007	2.21	0.09	0.28
1	1960	23.52	0.030	2.25	0.10	0.29
1.5	1960	23.52	0.067	2.30	0.10	0.29
2	1960	23.52	0.119	2.34	0.10	0.30
2.5	1960	23.52	0.186	2.39	0.10	0.30
3	1960	23.52	0.267	2.43	0.10	0.31
3.5	1960	23.52	0.364	2.48	0.11	0.32
4	1960	23.52	0.475	2.52	0.11	0.32
4.5	1960	23.52	0.601	2.57	0.11	0.33
5	1960	23.52	0.743	2.61	0.11	0.33
5.5	1960	23.52	0.898	2.66	0.11	0.34
6	1960	23.52	1.069	2.70	0.11	0.34
6.5	1960	23.52	1.255	2.75	0.12	0.35
7	1960	23.52	1.455	2.79	0.12	0.36
7.5	1960	23.52	1.671	2.84	0.12	0.36
8	1960	23.52	1.901	2.88	0.12	0.37
8.5	1960	23.52	2.146	2.93	0.12	0.37
9	1960	23.52	2.406	2.97	0.13	0.38
9.5	1960	23.52	2.680	3.02	0.13	0.38
10	1960	23.52	2.970	3.06	0.13	0.39

A plot of the ultimate lateral load capacity vs. embedment depth for clayey soils is shown in Figure 4-8. The ultimate load capacity is bilinear due to the varying cross section of the pole.

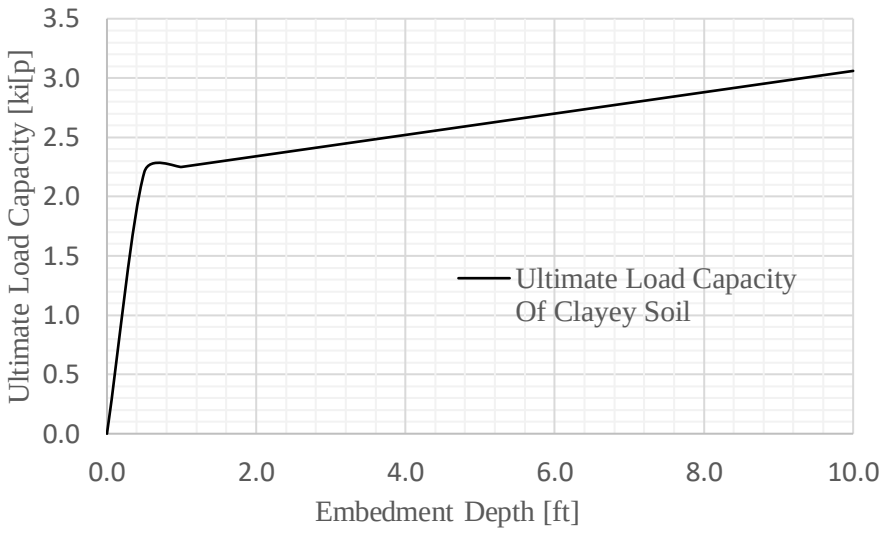

Figure 4-8. Ultimate Load Capacity Vs. Depth for Clayey Soil Soils

The analysis for the ground and pole tip displacements are done using the SAP2000 program.

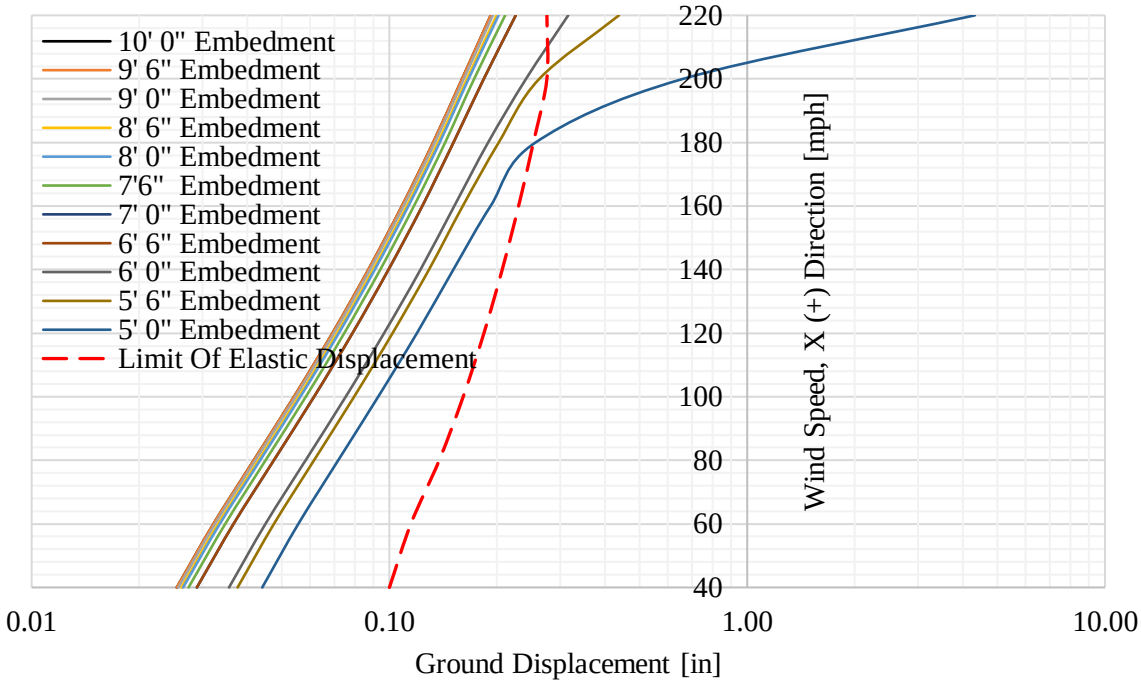

Figure 4-9. Ground Displacement for Static Wind Load Various Embedment Depth

The ground displacement for various positive wind speeds in the X-direction and embedment depths is shown in Figure 4-9. The horizontal axis is plotted on a logarithmic scale to visualize the displacement response better. In a dashed line, the line for elastic displacement for clayey soil is also shown to demarcate the elastic and non-linear displacements for various wind speeds in the positive X-directions. Displacements to the right of the elastic curve indicate that the ground displacements are non-linear, while displacements on the left side of the elastic curve mean that the ground displacements are elastic.

For 5’ 0” embedment depth, **Error! Reference source not found.**1” and 4.5” ground displacement are observed at 205 mph and 220 mph, respectively. A 5’ 0” embedment depth is about 16.6% of the total pole length (30’ 0” in this case).

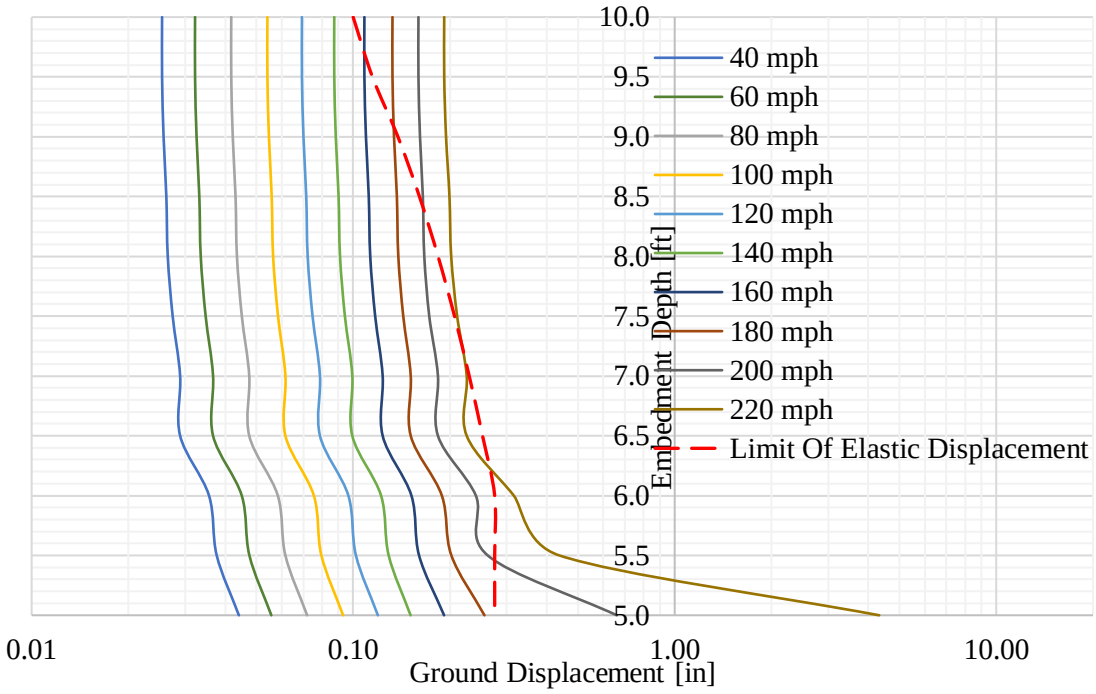

Figure 4-10. Ground Displacements Vs. Embedment Depth for Various Wind Speeds

Figure 4-10 is plotted for ground displacement vs. embedment depths for various wind speeds. The horizontal axis is plotted in a logarithmic scale to visualize the displacement response better.

Ground displacements remain elastic up to 140mph for depths from 5’ 0” to 10’ 0”. Excessive ground displacements can be seen from wind speeds of 200 mph and 220 mph for less than 6’ 0” embedment. Wind speeds higher than 160 mph will induce permanent ground displacements in clayey soils. The embedment depth for 220 mph with 5’ 0” embedment will see ground displacements of 4.5” or more. Typically, ground displacements are limited to less than 1”. Hence, a minimum of 5’ 6” embedment (18% of the total length of the pole) shall be provided to limit the ground displacement to less than 1 inch.

As discussed in previous sections, the cable tension increases non-linearly and provides a restraint at the top of the pole. The increase in the cable tension is shown in Figure 3-5 and Table 3-1. This indicates that excessive ground displacement is unlikely for clayey soils subject to (-) X-direction winds.

The ground displacement response for wind in the Y-direction is shown in Figure 4-11. The 100 ft cable element will transmit wind load and cable tension at the top of the wood pole. The displacement at the top of the pole will have X- and Y- components. The resultant of the X-and displacements is used to compute the resultant displacements.

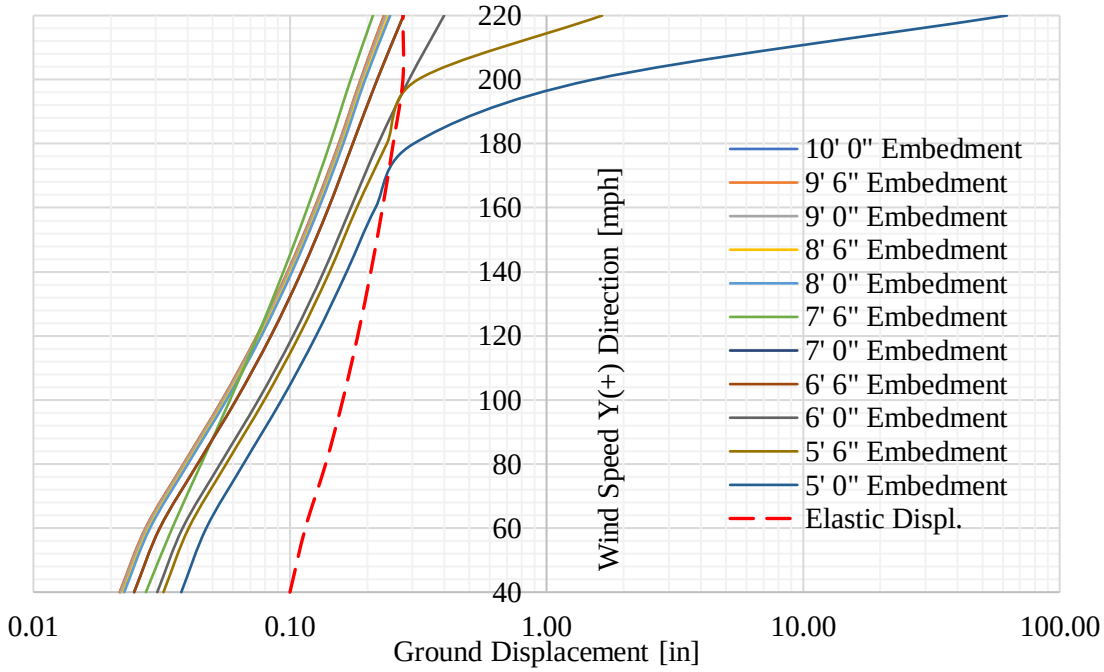

Figure 4-11. Resultant Ground Displacement Vs. Wind Speed

The resultant ground displacements for 6’ 0” and greater embedment depths are less than 1” but are permanent as they are larger than 0.1 inch., the elastic displacement limit for clayey soil. A permanent displacement of about 1.75” occurs for a 5’ 6”

embedment depth and 220 mph wind speed. There will be imminent collapse of the class H1 wood pole for 5’ 0” embedment and subjected to 220 mph wind pressure. The additional wind load from the cable contributes to the collapse of the pole from a theoretical ground displacement of about 61”.

From the above discussion, it can be concluded that the collapse of a class H1 wood pole due to excessive ground displacement would be in the Y-direction. In other words, the wood pole collapse would occur, due to excessive ground displacement, in the perpendicular direction of the cable for winds speeds greater than 150 mph.

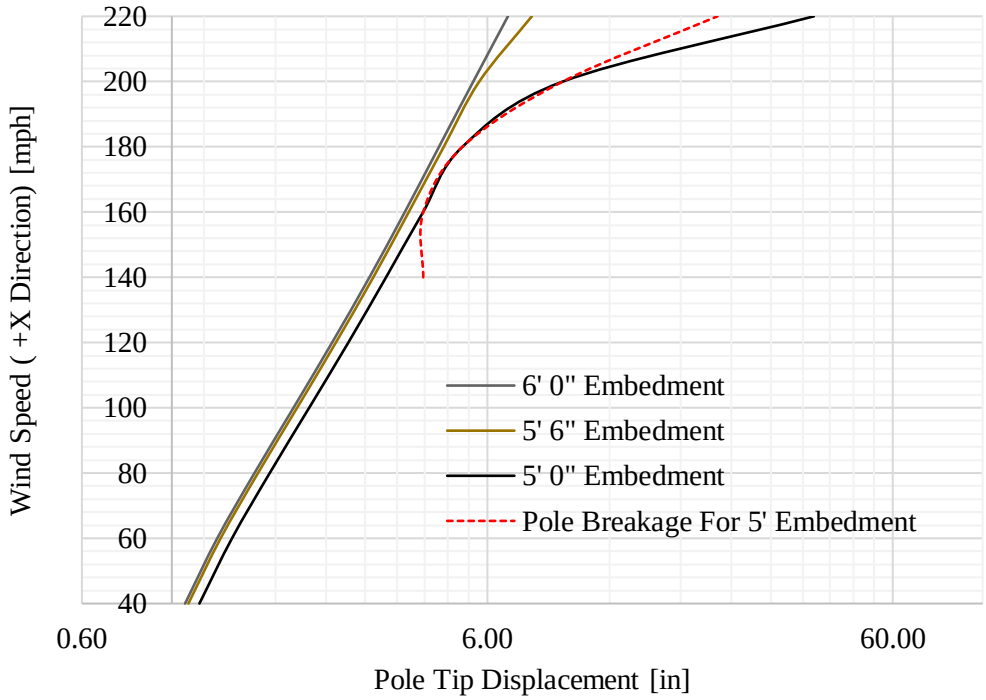

Figure 4-12. Pole Tip Displacement Vs. Wind Speed

Figure 4-12 shows the pole tip displacements for 5’ 0”, 6’ 0” and 6’ 6” embedment depths in clayey soils for wind speeds from 40 to 220 mph in the positive X-direction. The red

dashed line is the pole breakage displacement for 5’ 0” embedment depth. Pole breakage will occur in the class H1 pole embedded 5’ 0” in clayey soils at a wind speed of about 160 mph. However, poles with 5’ 6” and greater embedment depths will not suffer any breakage. The displacements for depths 6’ 6” and larger are not shown in Figure 4-12 since no breakage will occur. The graph portion to the right of the red dashed line is irrelevant since pole failure would have already happened.

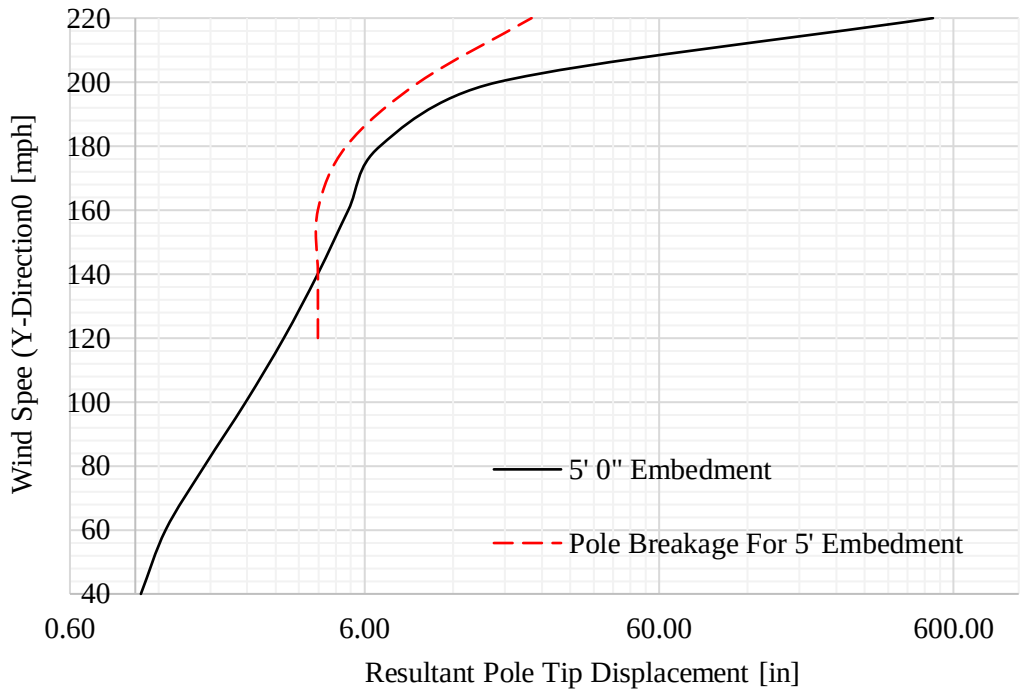

Figure 4-13. Pole Tip Displacement Vs. Wind Speed (Y-Direction) for 5’ 0” Embedment

Figure 4-13 is the graph for pole tip displacements Vs. Wind speed in the Y-direction with 5’ 0” embedment in clayey soils. The pole breakage will likely occur at 140 mph for the 5’ 0” embedment depth. The portion of the displacement graph to the right of the pole breakage displacement line is irrelevant since the pole would have failed at 140 mph.

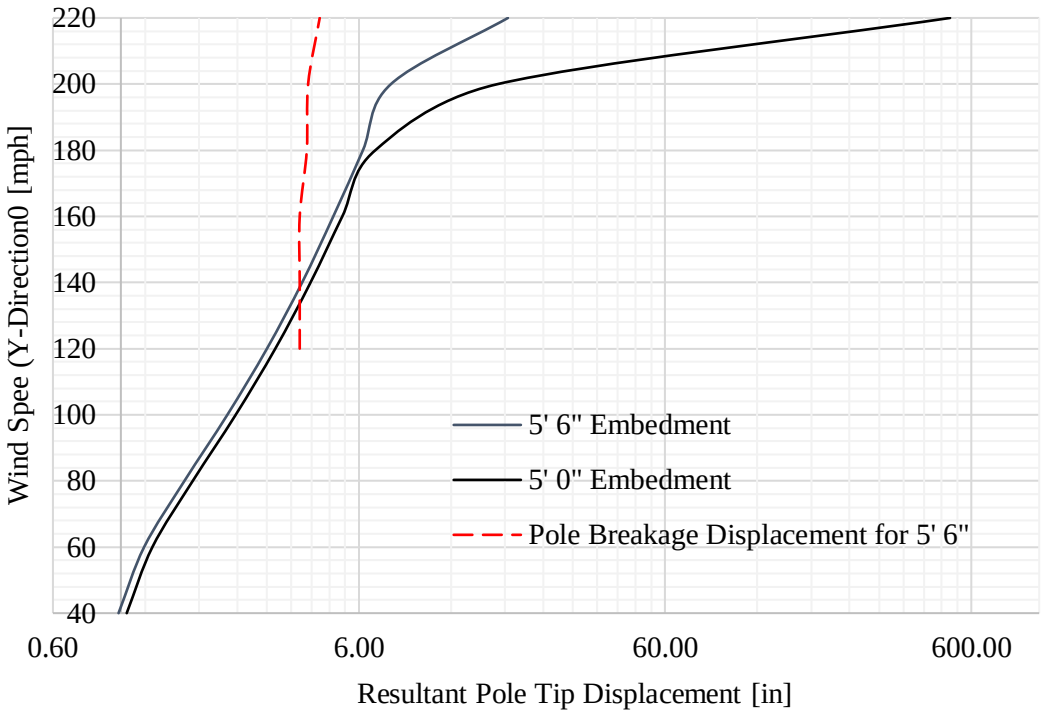

Figure 4-14. Pole Tip Displacement Vs Windspeed (Y-Direction)

Figure 4-14 shows pole tip displacements Vs. wind speeds perpendicular to the plane of the cable for poles with 5’ 0” and 5’ 6” embedment depths. The pole breakage occurs at about 150 mph for both the poles. These graphs also show the pole breakage displacements in a dashed line. The pole breakage displacement to the right of the dashed line is non-applicable. Pole tip displacements decrease with a decrease in embedment depths.

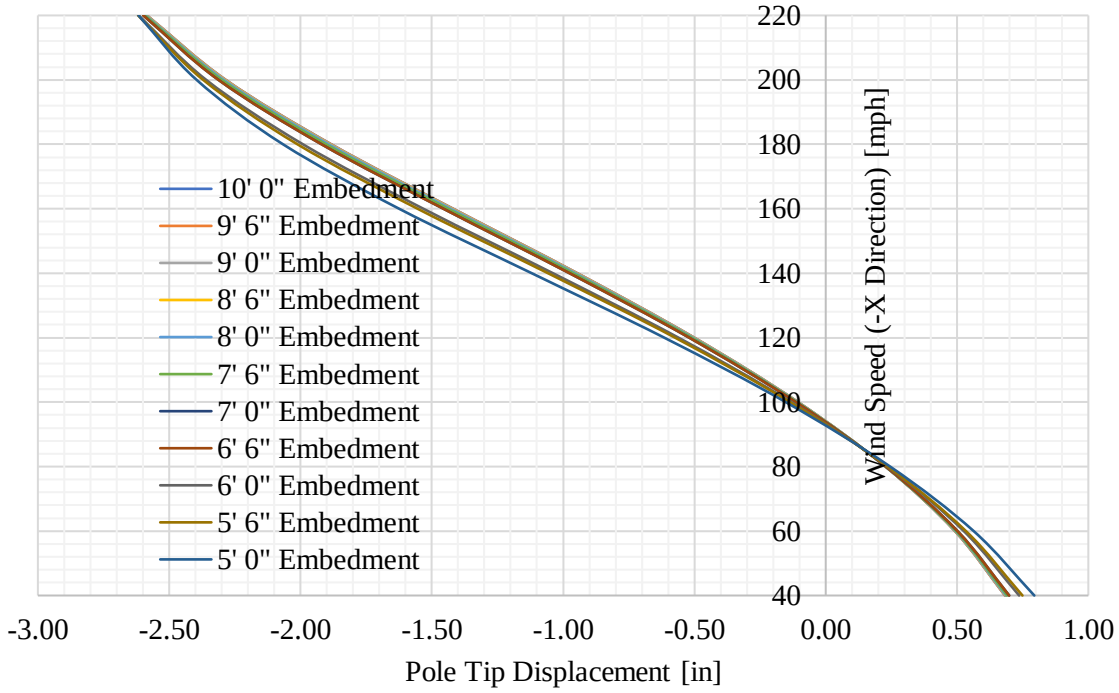

Figure 4-15. Wood Pole Tip Displacement Vs. Static Wind Speeds (-ve X-Direction)

Figure 4-15 is a graph for pole tip displacements for various wind speeds in the negative X-direction and embedment depths. Pole tip displacements in the negative X-directions are significantly smaller than the +ve X-and Y-direction winds. These displacements are also considerably smaller than the breakage displacements, and hence, it is unlikely that pole breakage will occur for winds in the positive X-direction.

4.5 Ground and Pole Tip Displacement of Class H1 Pole Embedded in Sandy Soil and Subjected to Static Wind Loads.

This section studies the ground and pole tip displacement characteristics of a class wood H1 pole embedded in sandy soils. The soil is modeled as non-linear springs to

understand the ground displacement failures. The theoretical load displacement values for sandy soils are shown in Table 4-6.

Table 4-6: Soil Spring Constants and Displacement for Sandy Soil

Z [ft]	$E_{s,z}$ [psi/ft]	K_h [kip/in]	K_z [kip/in]	F_{ult} [kip]	d_u [in]	d_{umax} [in]
0	0	0	0	0	0	0
0.5	330	3.96	0.009	0.304	0.077	0.231
1	660	7.92	0.036	0.609	0.077	0.231
1.5	990	11.88	0.082	0.913	0.077	0.231
2	1320	15.84	0.145	1.218	0.077	0.231
2.5	1650	19.8	0.227	1.522	0.077	0.231
3	1980	23.76	0.327	1.827	0.077	0.231
3.5	2310	27.72	0.445	2.131	0.077	0.231
4	2640	31.68	0.581	2.436	0.077	0.231
4.5	2970	35.64	0.735	2.740	0.077	0.231
5	3300	39.6	0.908	3.044	0.077	0.231
5.5	3630	43.56	1.098	3.349	0.077	0.231
6	3960	47.52	1.307	3.653	0.077	0.231
6.5	4290	51.48	1.534	3.958	0.077	0.231
7	4620	55.44	1.779	4.262	0.077	0.231
7.5	4950	59.4	2.042	4.567	0.077	0.231
8	5280	63.36	2.323	4.871	0.077	0.231
8.5	5610	67.32	2.623	5.175	0.077	0.231
9	5940	71.28	2.940	5.480	0.077	0.231
9.5	6270	75.24	3.276	5.784	0.077	0.231
10	6600	79.2	3.630	6.089	0.077	0.231

The non-linear load displacement values are used to model the soil behavior in the SAP2000 program. The variation of ultimate lateral capacity with embedment depths for sandy soils is shown in Figure 4-16.

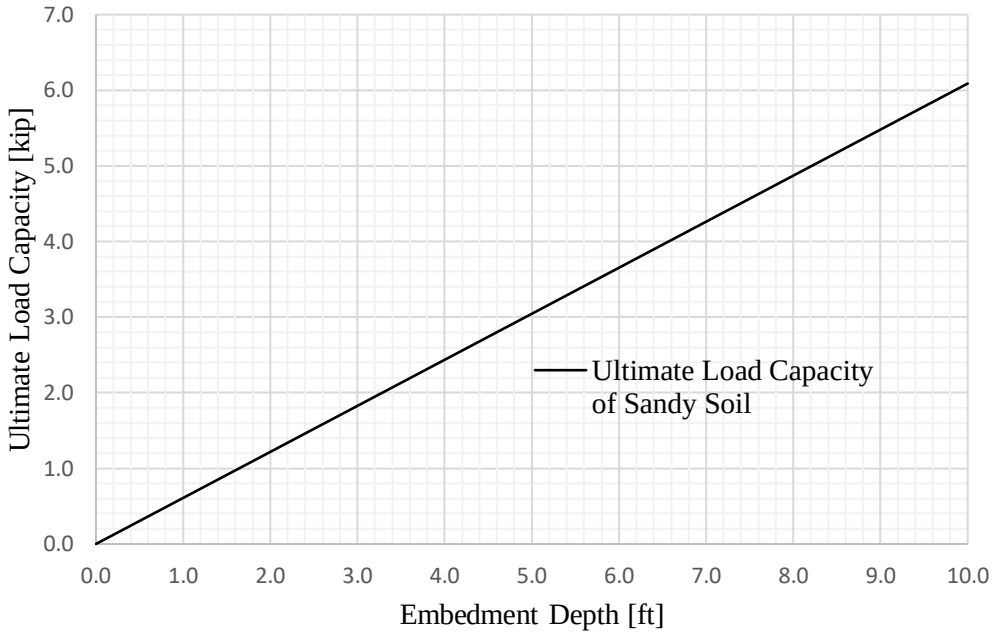

Figure 4-16. Ultimate Load Capacity vs Embedment for Sandy Soil

The ground displacements obtained from analysis are shown in Figure 4-17, Figure 4-18, and Figure 4-19. The elastic displacements are also plotted to differentiate the elastic and non-linear ground displacements. The elastic displacement is independent of depth for Sandy Soils.

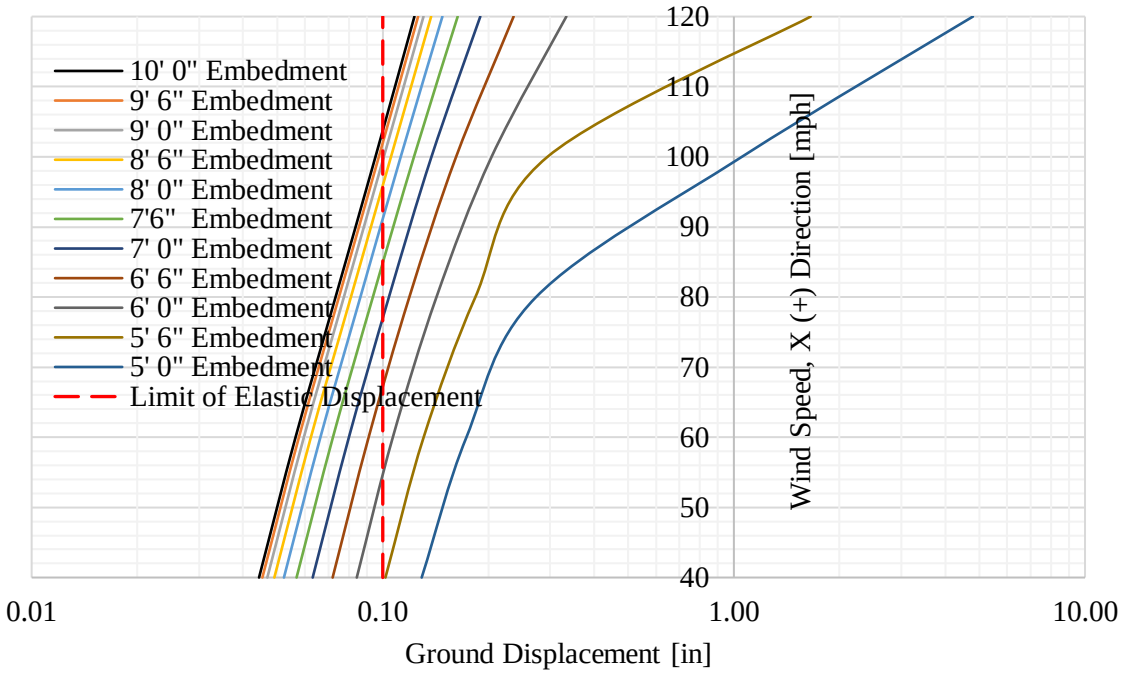

Figure 4-17. Ground Displacement Vs. Windspeed (+ve X) for Various Embedment Depth

Figure 4-17 is plotted on a logarithmic scale along the X-axis to show the ground displacements more clearly.

The analysis was performed for wind speeds up to 120 mph since solution convergence could not be achieved for displacements for 5’ 0”, 5’ 6”, and 6’ 6” embedment depths. For poles with embedment depths of 5’ 0”, and 5’ 6”, 1” permanent displacements occurred at 100 mph, and 115mph.

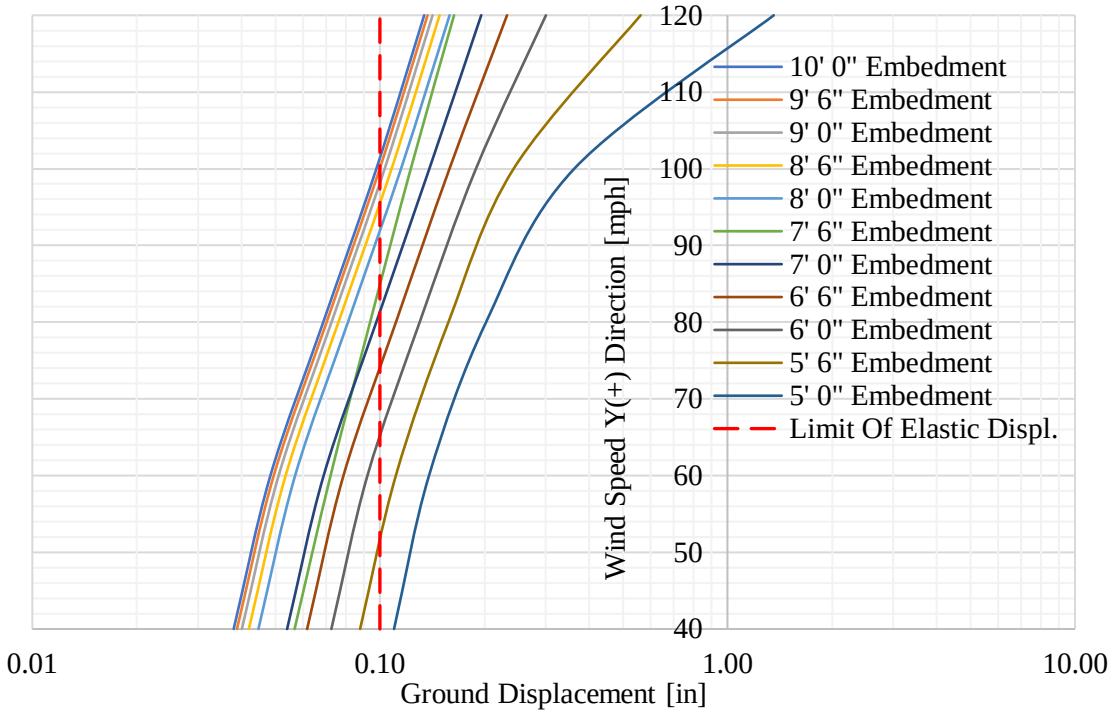

Figure 4-18. Ground Displacement Vs Wind Speed (+ve Y) for Various Embedment Depth

Figure 4-18 shows a plot of Ground displacement for various wind speeds in the Y-direction and embedment depths. A permanent ground displacement of 1” occurs for 115 mph wind in the +ve Y-direction and 5’ 6” embedment depth. Poles with embedment depths of 5’ 0” (16.7%) and 5’ 6” (18.4%) appear to have large ground displacements at lower wind speeds. Embedment depths must be increased for higher wind speeds to limit the permanent ground displacements.

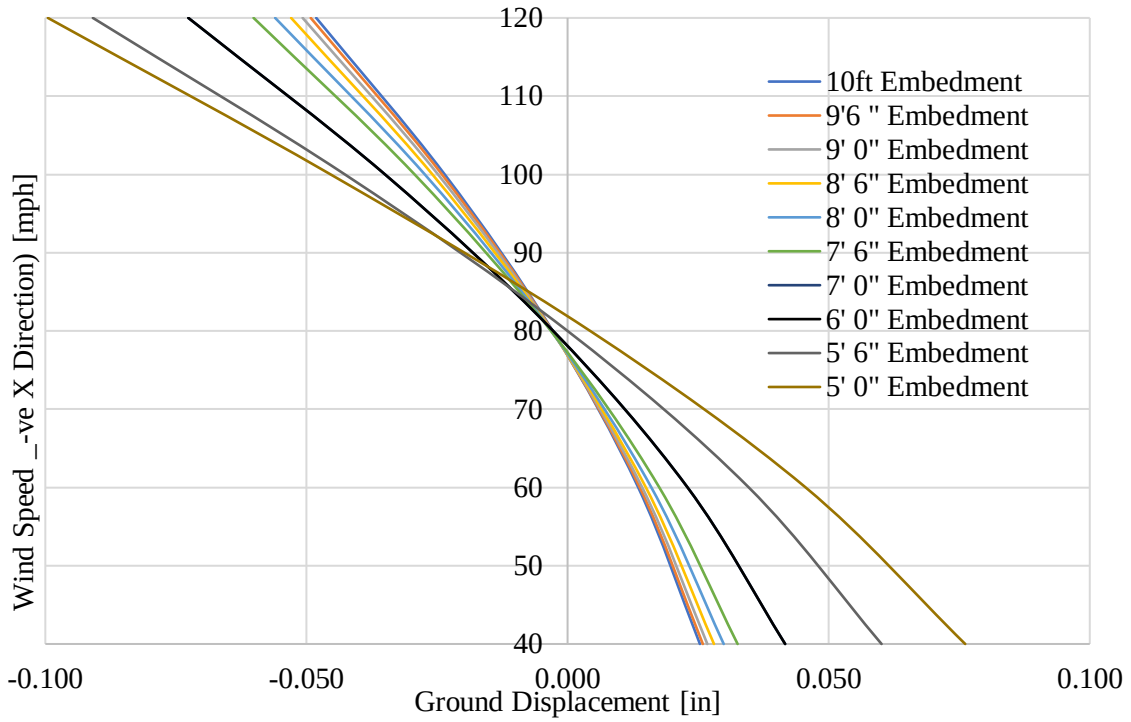

Figure 4-19. Ground Displacement Vs. Wind Speed (-ve X) Direction

Figure 4-19 is a graph for ground displacement for various wind speeds in the -ve X-direction and embedment depths. The ground displacements are significantly smaller when compared to +ve, X-, and Y-direction winds. Increased cable force with displacement restrains ground displacements in the -ve X-directions.

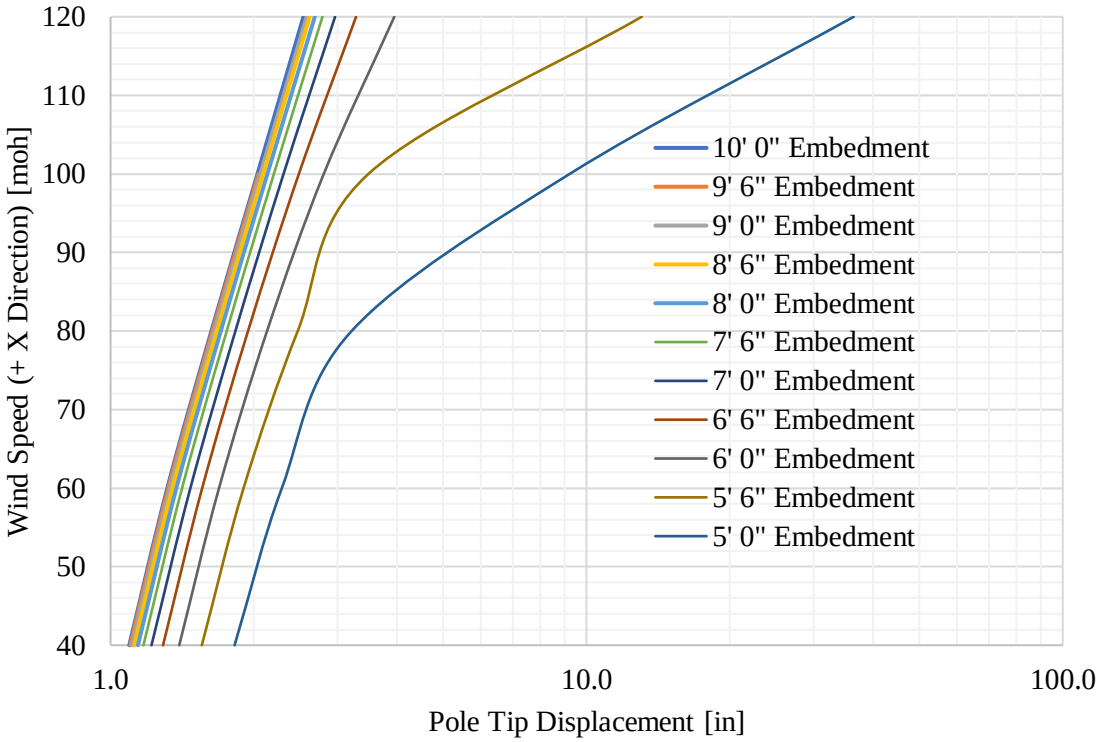

Figure 4-20. Pole Tip Displacement Vs. Wind Speed (+ve X-Direction)

Figure 4-20 shows the graph of Pole Tip displacement for various positive X-direction wind speeds for various embedment depths in the soil. The maximum displacement at the pole tip is 36.39 inches, and a bending moment of 9.73 ft-kip at the base is less than the breakage moment for 120 mph wind. The breakage bending moment is 18.91 ft-kip for the class H1 wood pole. It is unlikely that pole breakage will occur when the wind is in the negative X direction.

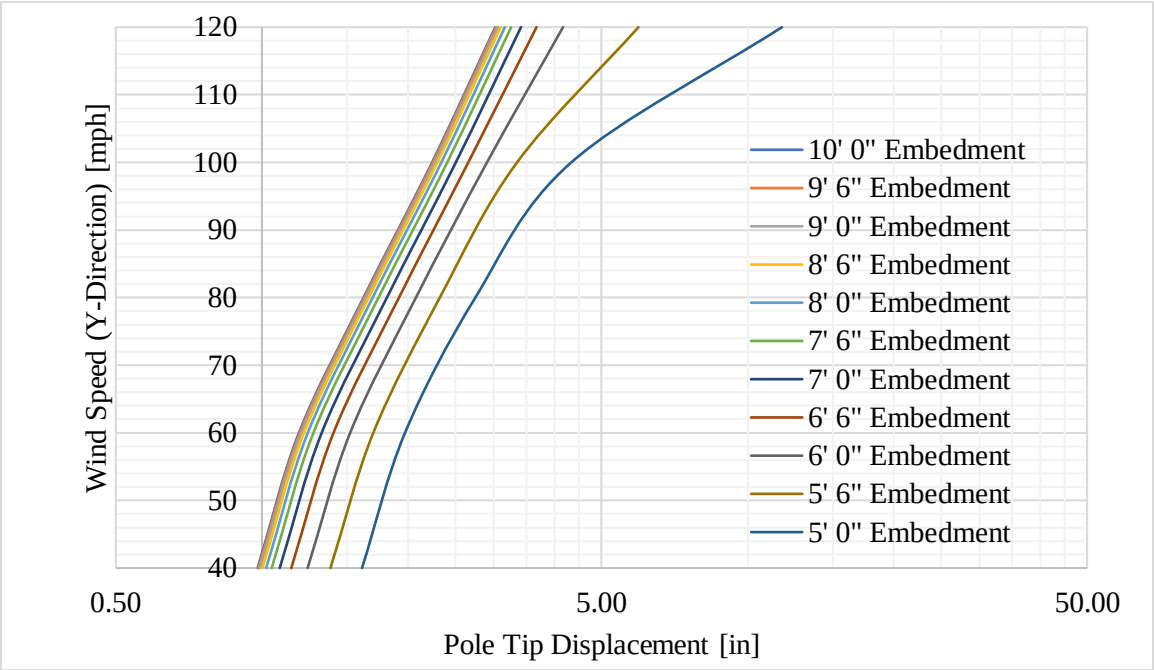

Figure 4-21. Pole Tip Displacement Vs. Wind Speed (Y-Direction)

Figure 4-21 is a graph for Pole Tip displacement for various positive Y-direction wind speeds and embedment depths. The cable tension provides restraining forces at the top of the poles, hence higher resistance to wind forces. The maximum displacement for wind in the Y-direction is 11.76 inches. It is unlikely that breakage will occur in the Class H1 pole embedded in sandy soils up to 120 mph.

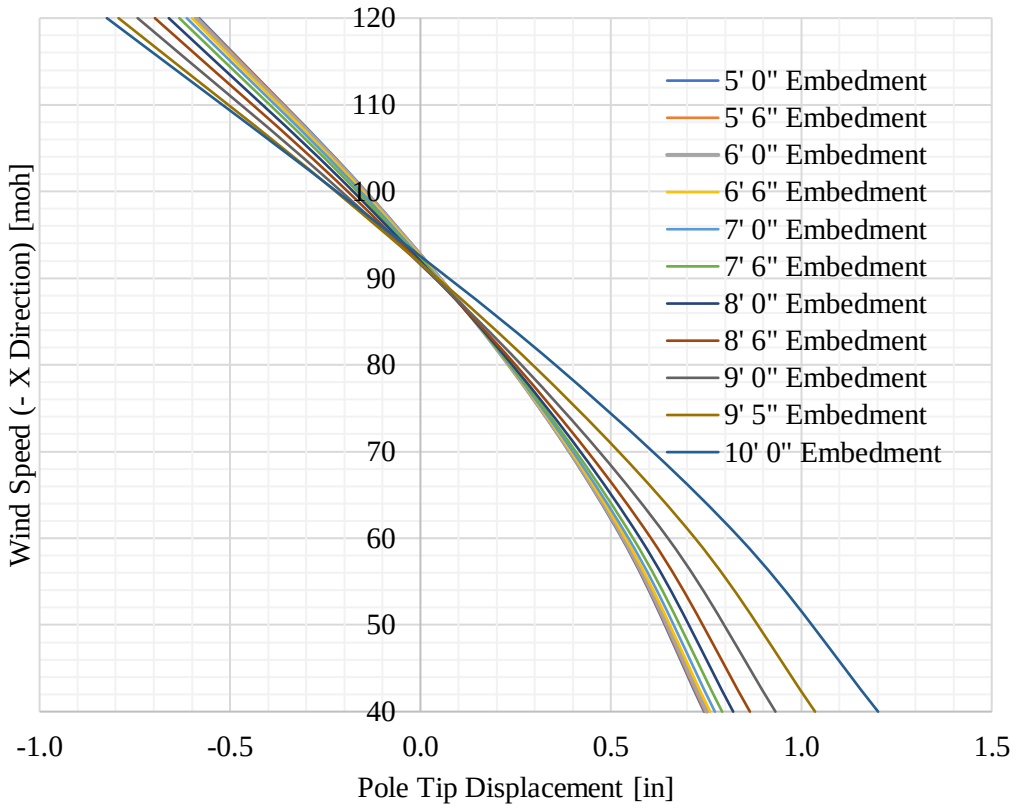

Figure 4-22. Displacement Vs. Wind Speed (-ve X-Direction)

Figure 4-22 is a graph for Pole Tip displacement and various negative X-direction Wind Speeds and embedment depths. The displacement is significantly smaller when compared to the positive X- and Y-direction wind.

4.6 Prediction of Pole Breakage Locations

In this section, the breakage points along the height of the pole are studied. The breakage height is calculated using the experimentally obtained bending stress, pole diameter, and wind loads based on ASCE 7-16. The bending stress for the test pole is 2214 psi. The corresponding bending stress at breakage is 18.92 ft-kip.

A relationship between wind speed and pole tip displacement at the time of pole breakage is shown in Figure 4-23.

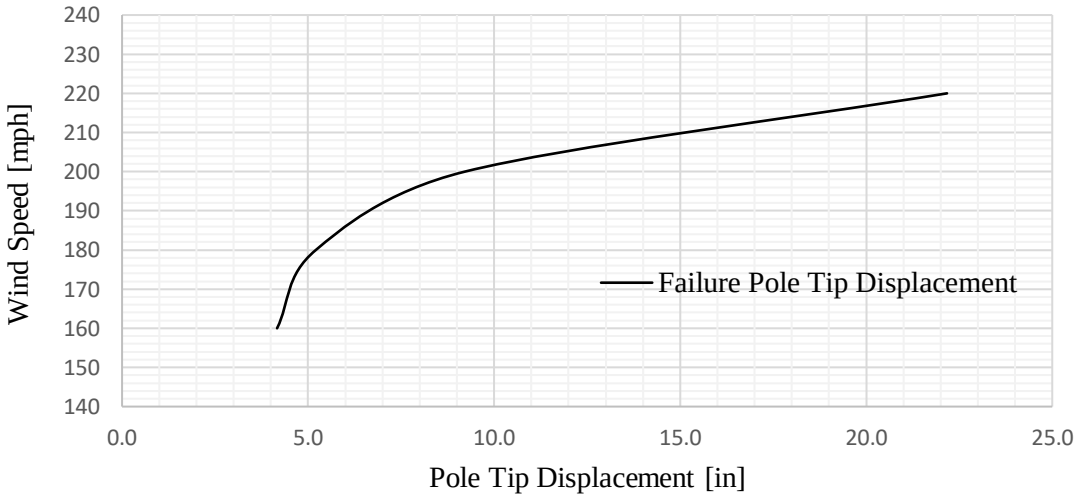

Figure 4-23. Graph of Wind Speed Vs. Pole Failure Displacement for 5’ 0” Embedment Depth in Clayey Soil

For the class H1 wood pole, it’s unlikely that the pole breakage through bending will occur for wind speeds less than 160 mph. The breakage point will likely happen closer

to the ground at 160 mph and higher elevations from the ground level for higher speeds. The breakage point is approximately 7 ft from the ground level for 220 mph speed.

The breakage of the poles can happen when a high-speed wind of more than 160 mph is in the positive X or Y direction. Breakage is unlikely in the -ve X directions, and the tip and ground displacements are smaller than the +ve X- or Y-directions.

The analysis was for sandy soils with wind speeds up to 120 mph because the solution did not converge for 5’ 0” and 5’ 6” embedment depths. The bending moment at the ground level for 120 mph is 9.73 ft-kip, less than the pole breakage moment of 18.91 ft-kip. Hence, it is unlikely that any pole breakage will occur in the pole embedded in sandy soils with wind speeds up to 120 mph.

4.7 Effect of Cable Mass Ratio

The effect of the cable mass ratio on the dynamic response of the test poles is discussed in this section. A 5’ 0” tall test pole was selected for this study. The physical properties of the test pole are shown in Table 2-1 and Table 2-2. The dynamic analysis was performed using SAP2000, and the results are shown in Table 4-7. The effect of the mass ratio on the natural frequency response is shown in Figure 4-24.

Table 4-7: Dynamic Response of 5ft Test Pole with varying span and mass ratios

S. No	Span of Cable [ft]	Weight of Cable [lbf]	Mass Ratio	Period [s]	Natural Frequency [Hz]
1	25	5.09	1.52	0.984	1.016
2	24	4.88	1.46	0.953	1.049
3	23	4.68	1.40	0.922	1.084
4	22	4.47	1.33	0.892	1.121
5	21	4.27	1.27	0.862	1.161
6	20	4.07	1.21	0.863	1.202
7	19	3.86	1.15	0.802	1.247
8	18	3.66	1.09	0.772	1.295
9	17	3.45	1.03	0.743	1.346
10	16	3.25	0.97	0.713	1.402
11	15	3.05	0.91	0.686	1.458
12	14	2.84	0.85	0.655	1.527
13	13	2.64	0.79	0.626	1.599
14	12	2.44	0.73	0.596	1.678
15	11	2.23	0.67	0.566	1.766
16	10	2.03	0.61	0.536	1.866
17	9	1.83	0.55	0.505	1.981
18	8	1.62	0.48	0.473	2.114
19	7	1.42	0.42	0.439	2.276
20	6	1.22	0.36	0.405	2.466
21	5	1.01	0.30	0.369	2.713
22	4	0.81	0.24	0.329	3.044
23	3	0.61	0.18	0.284	3.524
24	2	0.41	0.12	0.231	4.325
25	1	0.20	0.06	0.163	6.124
26	0.5	0.10	0.03	0.115	8.663
27	0.25	0.05	0.02	0.082	12.247

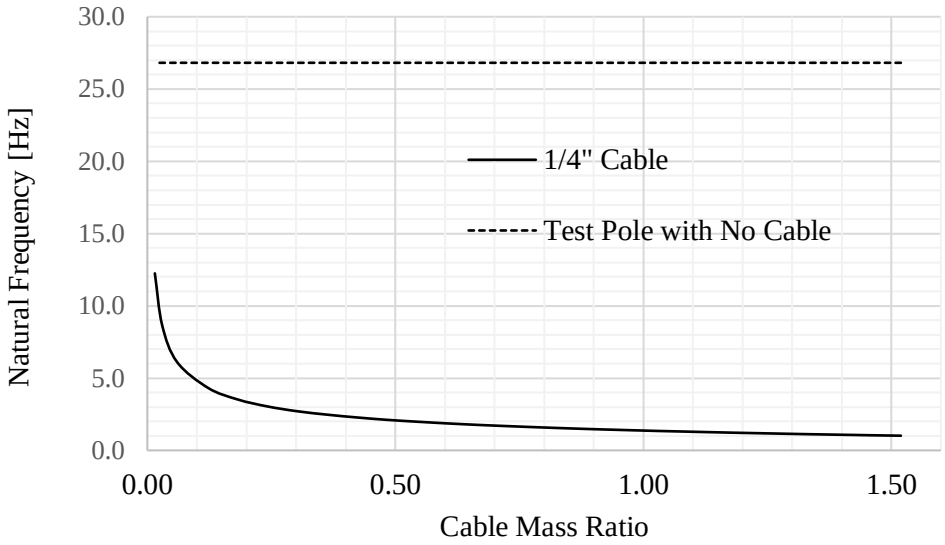

Figure 4-24. Graph of Cable Mass Ratio Vs. Response Natural Frequency

The effect of the cable mass ratio on the natural system frequency is shown in Figure 4-24. The influence of the cable mass ratio on the natural frequency is negligible below 5%. The natural frequency reduction above 5% cable mass ratio follows an exponential curve. This curve is consistent and similar to the cable's non-linear load-displacement curve. The natural frequency of the test pole with no cable is 26.816Hz, shown in a dashed line in the figure.

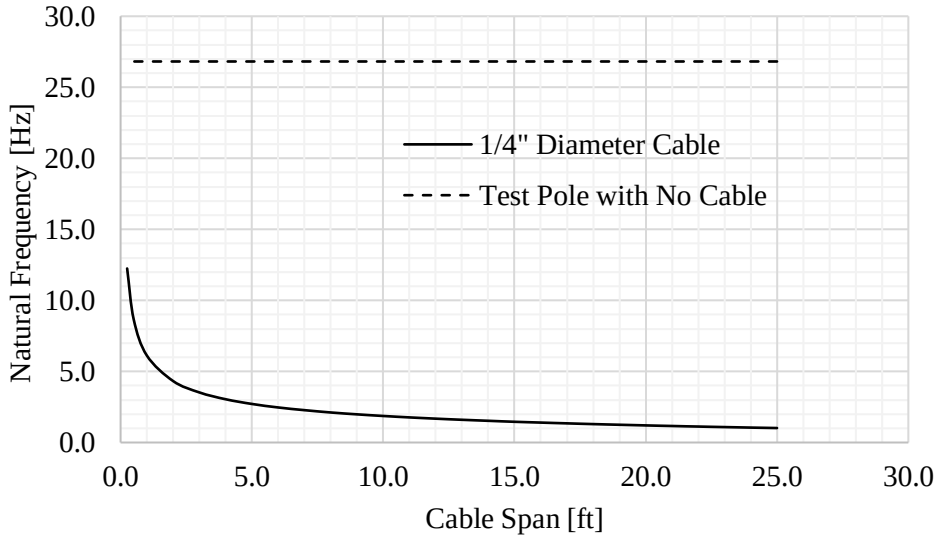

Figure 4-25. Natural Frequency Vs. Cable Span

Figure 4-25 shows the effect of the cable span on the system's natural frequency. The relationship appears to be similar to the cable mass ratio since the span of the cable and mass are coupled.

4.8 Frequency Response of 5 ft Test Pole

This section presents the results of the dynamic response of a 1/5th scale, 5' 0" tall cantilever test pole embedded in clayey, sandy soils and rock. The properties of the pole are per Table 2-1. The simulation was done using SAP2000 for various embedment depths. The frequency responses are shown in Table 4-8.

The response frequency and period of a 5 ft cantilever assuming a fixed base are 25.939 Hz and 0.039 s, respectively.

Table 4-8: Response Period and Frequencies for 5ft Test Pole

		Sandy Soil		Clayey Soil		Rock	
Embedment Depth [in]	Embedment Depth [%]	Frequency [Hz]	Period [sec]	Frequency [Hz]	Period [sec]	Frequency [Hz]	Period [sec]
3	4.2%	-	-	-	-	14.762	0.067
4.00	5.6%	5.876	0.150	9.695	0.103	19.054	0.052
5.00	6.9%	8.464	0.118	12.703	0.079	21.549	0.046
6.00	8.3%	11.149	0.090	15.306	0.065	22.895	0.044
7.00	9.7%	13.698	0.073	17.405	0.057	23.604	0.042
8.00	11.1%	15.923	0.063	19.010	0.053	23.970	0.042
9.00	12.5%	17.721	0.056	20.192	0.050	24.154	0.041
10.00	13.9%	19.085	0.052	21.039	0.048	24.240	0.041
11.00	15.3%	20.070	0.050	21.636	0.046	24.277	0.041
12.00	16.7%	20.753	0.048	22.050	0.045	24.290	0.041

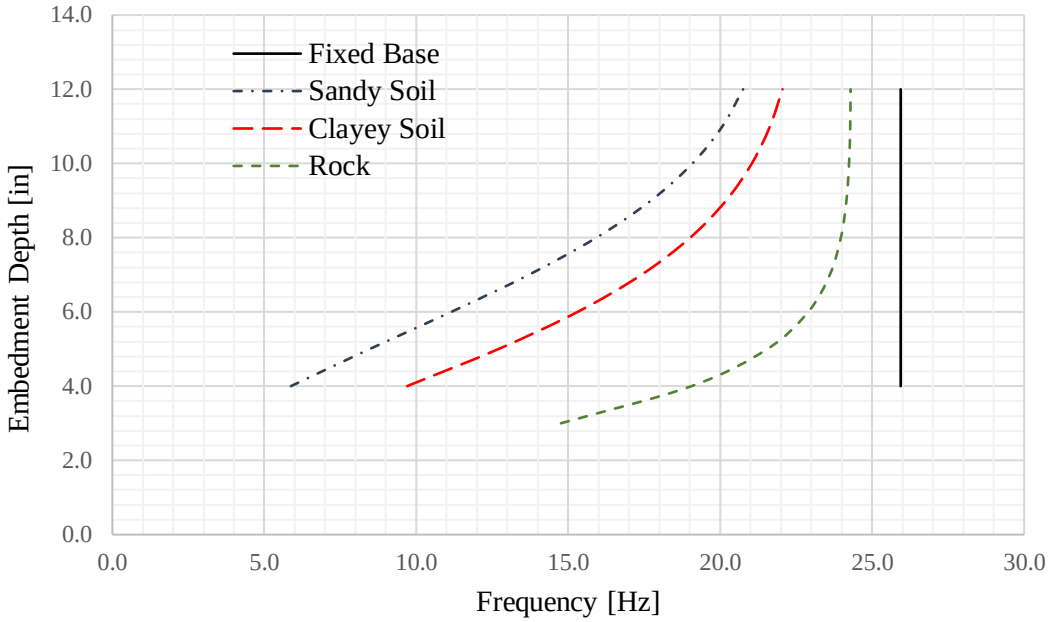

Figure 4-26. Response Frequency Vs Embedment Depth [in] for 5 ft Test Pole

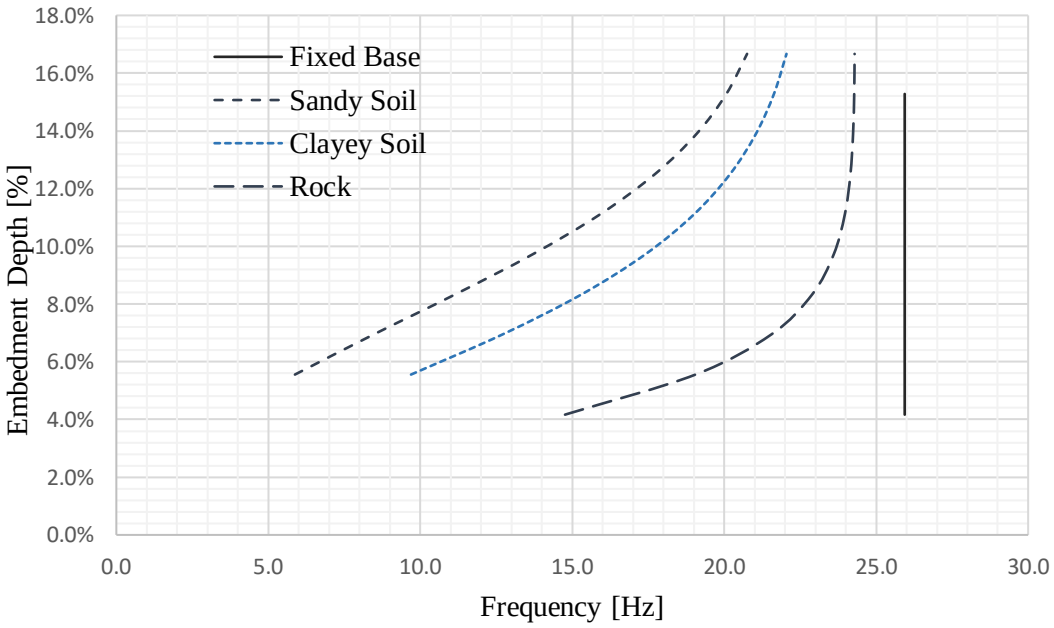

Figure 4-27. Response Frequency Vs. Embedment Depth [%] for 5 ft Test Pole

Figure 4-27 and Figure 4-28 are graphs for the natural response frequency as a function of embedment depths for the test poles. As with the class H1 wood pole, the 5 ft test pole shows a similar frequency response.

There is no significant increase in the natural frequency response for rock beyond 10% embedment depth. The response frequencies are significantly lower for sandy and clayey soils when compared to rock. There is a 46.5% and 24% increase in the response frequencies for a 5% increase in embedment depths from 10% to 15%.

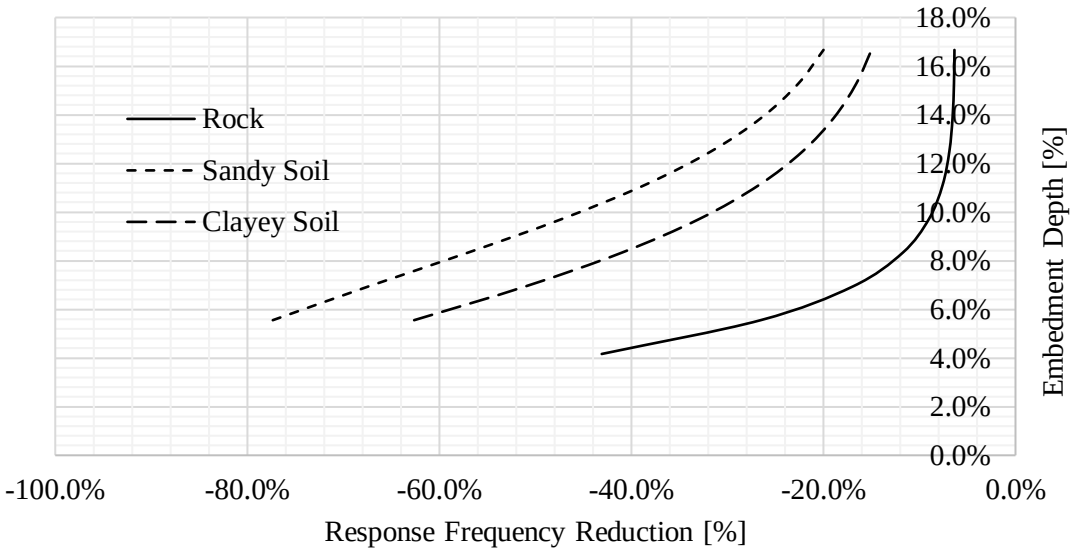

Figure 4-28. Response Frequency Deviation from Fixed Base Condition for 5 ft Test Pole

Figure 4-28 shows the natural frequency reduction for the 5-foot-tall test pole embedded in sandy, clayey, and rock relative to a fixed base. The response frequency

reduction for rock is negligible for embedment depths greater than 10%. The reduction is 47.5% and 32.9% for Sandy and clayey soils, respectively, corresponding to 10% embedment depths. The deviations are 22.6% and 16.6% for sandy and clayey soils, respectively, corresponding to 15% embedment depth.

The scaled-down test model exhibits similar dynamic response characteristics compared to the class H1 pole.

4.9 Dynamic Response of Class H1 Pole Subject to Dynamic Time History Wind Load Embedded in Clayey and Sandy Soil.

The dynamic response of the class H1 wood pole with 100 ft cable embedded in clayey and sandy soils subjected to dynamic time history wind load is presented in this section. The frequency of the wind time history is set to the fundamental system frequency. A resonant condition occurs when the ratio of the forcing function's frequencies and the pole's natural frequency equals one.

Table 4-9: Nodal Wind Loads on Class H1 Wood Pole

Nodal Wind Load [lbf]										
Height [ft]	5mph [lbf]	10mph [lbf]	15mph [lbf]	20mph [lbf]	25mph [lbf]	30mph [lbf]	40mph [lbf]	60mph [lbf]	80mph [lbf]	100mph [lbf]
0	0.39	1.57	3.54	6.29	9.83	14.16	25.17	56.63	100.68	157.31
1	0.78	3.11	6.99	12.43	19.42	27.97	49.72	111.87	198.88	310.76
2	0.77	3.07	6.91	12.28	19.18	27.62	49.10	110.48	196.41	306.89
3	0.76	3.03	6.82	12.12	18.94	27.27	48.48	109.09	193.94	303.02
4	0.75	2.99	6.73	11.97	18.70	26.92	47.87	107.70	191.46	299.16
5	0.74	2.95	6.64	11.81	18.46	26.58	47.25	106.31	188.99	295.29
6	0.73	2.91	6.56	11.66	18.21	26.23	46.63	104.91	186.51	291.43
7	0.72	2.88	6.47	11.50	17.97	25.88	46.01	103.52	184.04	287.56
8	0.71	2.84	6.38	11.35	17.73	25.53	45.39	102.13	181.57	283.70
9	0.70	2.80	6.30	11.19	17.50	25.18	44.77	100.74	179.09	279.83
10	0.69	2.76	6.21	11.04	17.25	24.84	44.15	99.35	176.62	275.96
11	0.68	2.72	6.12	10.88	17.16	24.49	43.54	97.96	174.14	272.10
12	0.67	2.68	6.04	10.73	16.77	24.14	42.92	96.56	171.67	268.23
13	0.66	2.64	5.95	10.57	16.52	23.79	42.30	95.17	169.20	264.37
14	0.65	2.61	5.86	10.42	16.28	23.45	41.68	93.78	166.72	260.50
15	0.64	2.57	5.77	10.27	16.04	23.10	41.06	92.39	164.25	256.64
16	0.64	2.56	5.75	10.22	15.98	23.01	40.90	92.02	163.60	255.62
17	0.64	2.54	5.72	10.18	15.909	22.89	40.70	91.58	162.80	254.38
18	0.63	2.53	5.69	10.12	15.81	22.76	40.47	91.06	161.88	252.93
19	0.63	2.51	5.65	10.05	15.71	22.62	40.21	90.47	160.83	251.30
20	0.62	2.49	5.61	9.98	15.59	22.45	39.92	89.81	159.67	249.48
21	0.62	2.48	5.57	9.90	15.47	22.28	39.60	89.10	158.41	247.51
22	0.61	2.45	5.52	9.82	15.34	22.09	39.26	88.34	157.05	245.39
23	0.61	2.43	5.47	9.73	15.20	21.88	38.90	87.53	155.60	243.13
24	0.60	2.41	5.42	9.63	15.05	21.67	38.52	86.67	154.07	240.74
25	0.60	2.38	5.36	9.53	14.89	21.44	38.12	85.76	152.47	238.23
Base Reaction	17.2	68.9	155.1	275.7	430.70	620.2	1102.6	2480.9	4410.5	6891.5

Table 4-9Table 4-9 shows the nodal wind loads based on ASCE -7 16. The wind load varies over the height of the pole. The 0 ft height in Table 4-9 represents the ground level. The nodal wind loads were only calculated for up to 100 mph. Generally, resonance occurs when low-speed winds with frequencies matching the natural frequencies of structures act on structures. It is common in tall cantilever-type structures like cantilever Utility poles, light poles, and industrial chimneys.

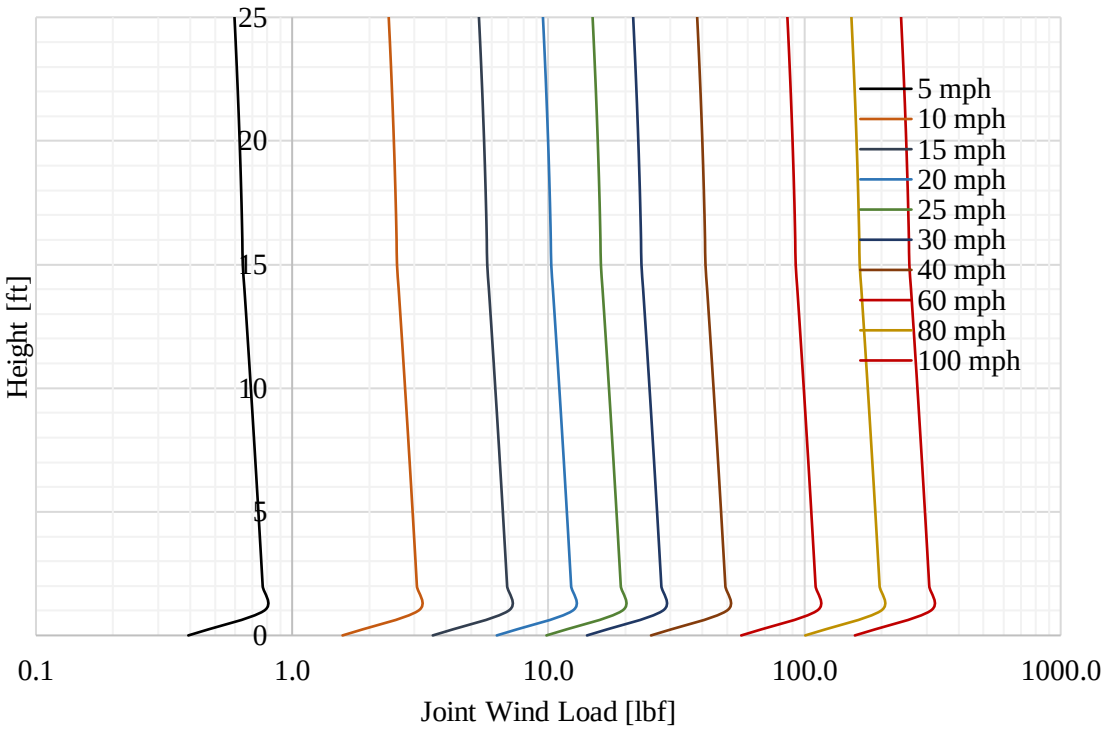

Figure 4-29. Nodal Wind Loads on Class H1 Wood Pole

The nodal wind loads, shown in Table 4-9, are plotted in a logarithmic scale along the X-axis, as shown in Figure 4-29. The non-uniform variation of wind load along the

height is due to the tapered cross-section of the wood pole and varying wind pressure coefficients.

The dynamic analysis was performed using SAP2000, and the dynamic amplification was computed for class H1 poles with 10’ 0”, 7’ 6”, and 5’ 0” embedment depths with wind speeds from 5 mph to 100 mph.

Table 4-10: Embedment Depths and Natural Frequencies

Embedment Depth		Length of Class H1 Pole [ft]	Natural Frequency [Hz]	
[ft]	Percentage Of Length of Pole		Clayey Soil	Sandy Soil
3	10.7%	28.00	-	-
4	13.8%	29.00	-	-
5	16.7%	30.00	3.70	3.34
7.5	23.1%	32.50	4.26	4.06
10	28.6%	35.00	4.37	4.19

Table 4-10 shows the natural frequencies of the class H1 pole for various embedment depths. The frequencies shown in the table above will used as the input frequencies of the wind time history forcing function.

The assumed wind load time history function is shown in Figure 4-30. A cosine function is selected since the maximum amplitude is obtained at t=0s.

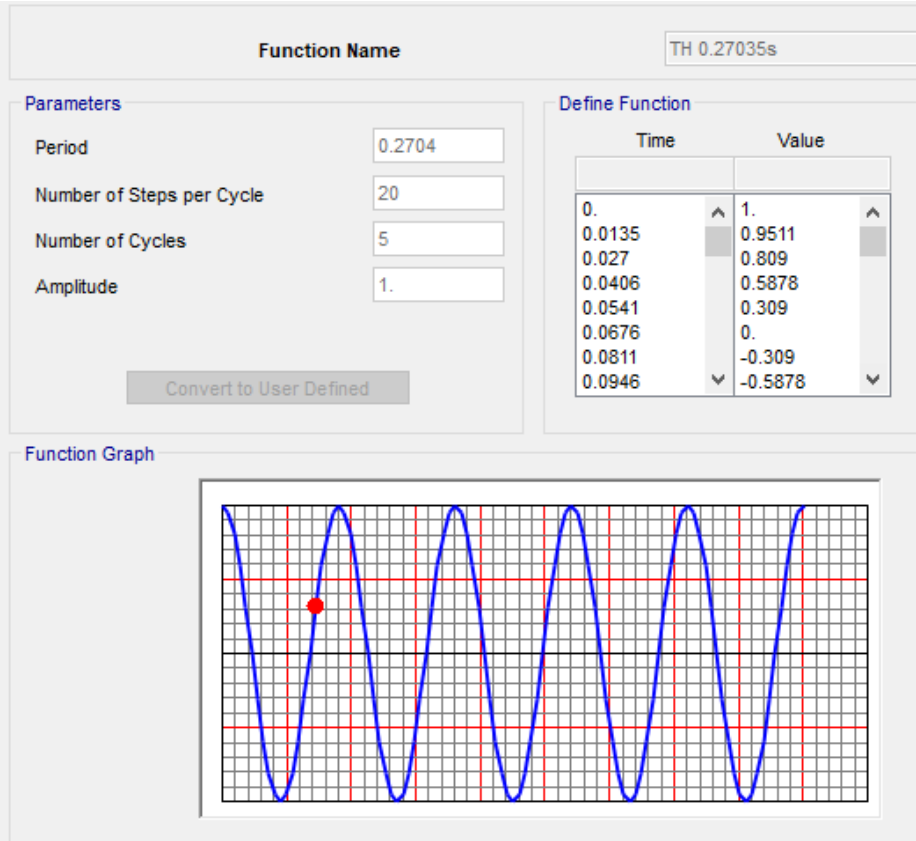

Figure 4-30. Wind Time History Cosine Function

The dynamic time history analysis was performed using SAP 2000 software by varying the amplitudes and frequencies for each wind speed and embedment depth.

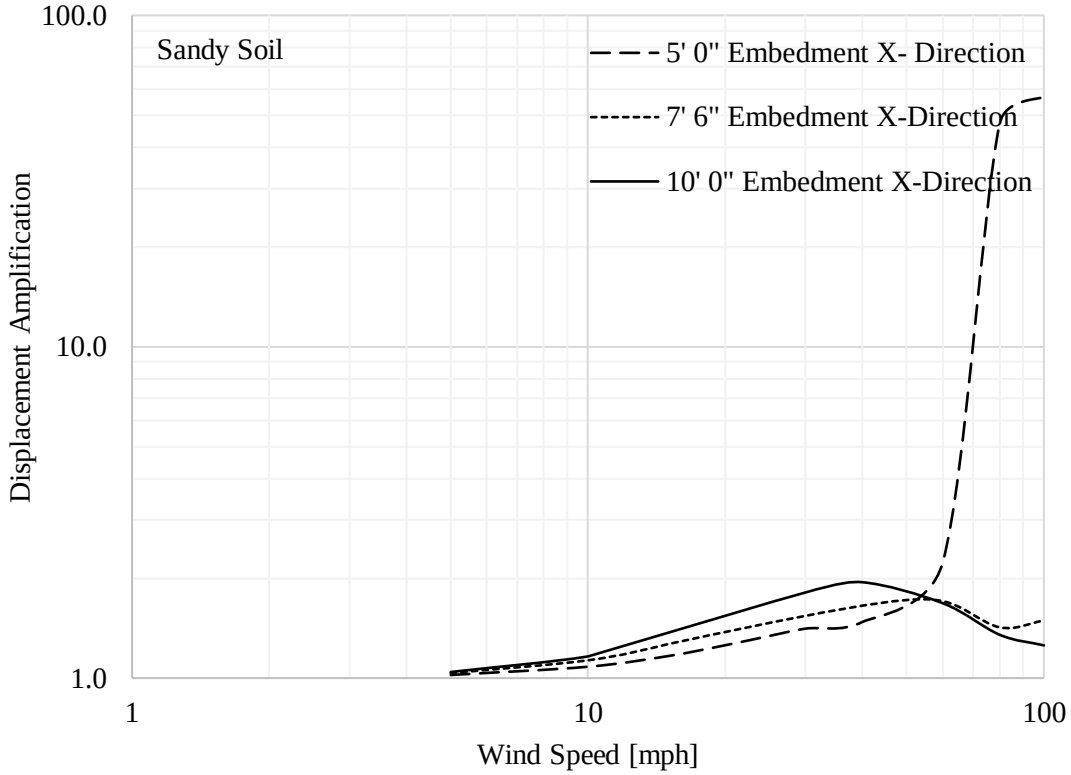

Figure 4-31. Displacement Amplification (X-Direction) in Sandy Soil for Class H1 Poles

The results of the dynamic response for sandy soil are shown in Figure 4-31 for wind in the X-direction and Figure 4-32 for wind and Y-direction, respectively.

Figure 4-31 shows the displacement amplification for wind in the X-direction along the horizontal axis and displacement amplification in the vertical axis. A peak amplification factor of 2 occurs at about 38 mph for an embedment depth of 10’ 0”. However, there is no visible peak for the 7’ 6’ and 5’ 0’ embedment depths below 50 mph wind speed. A significant displacement amplification occurs at about 75 mph for a 5’ 0” embedment depth, which will result in the pole breakage.

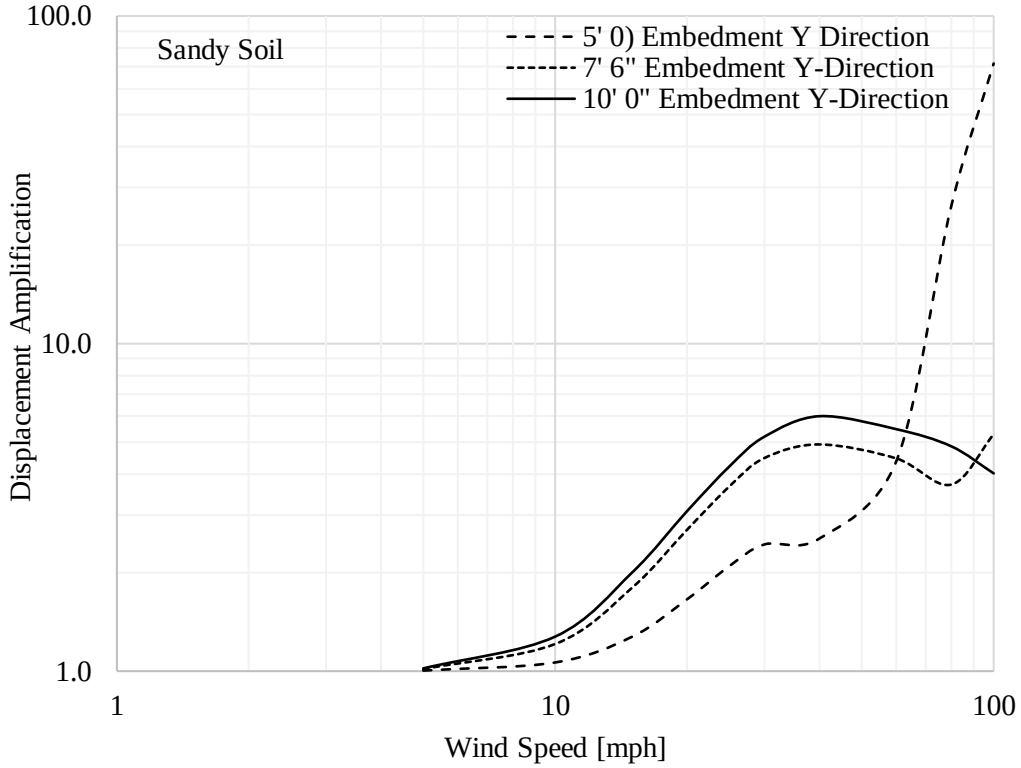

Figure 4-32. Displacement Amplification (Y-Direction) in Sandy Soils for Class H1 Poles

A 2.5 amplification for 5’ 0” embedment (16.67% Embedment) occurs at about 30 mph wind in the Y-direction. The corresponding amplification factors of 2 and 6.0 occur at about 38 mph and 40mph for 7’ 6” (23.1% Embedment) and 10’ 0” (28.6% Embedment) embedment depths. The amplification factor is smaller for smaller embedment depths. For smaller embedment depths, the maximum displacement amplitude seems to occur at lower wind speeds for winds perpendicular to the cable, the Y-direction in this case. The X-axis is assumed to be the parallel axis along the cable's longitudinal axis.

In the 5’ 0” embedment depth case, there is an initial displacement amplification of about 2.0 at about 30 mph. However, there is imminent collapse or breakage beyond 50 mph.

Figure 4-33 and Figure 4-34 are graphs for clayey soil for 5’ 0”, 7’ 6”, and 10’ 0” embedment depths for wind speeds from 5 mph to 100 mph. The graphs are plotted for X- and Y-wind directions.

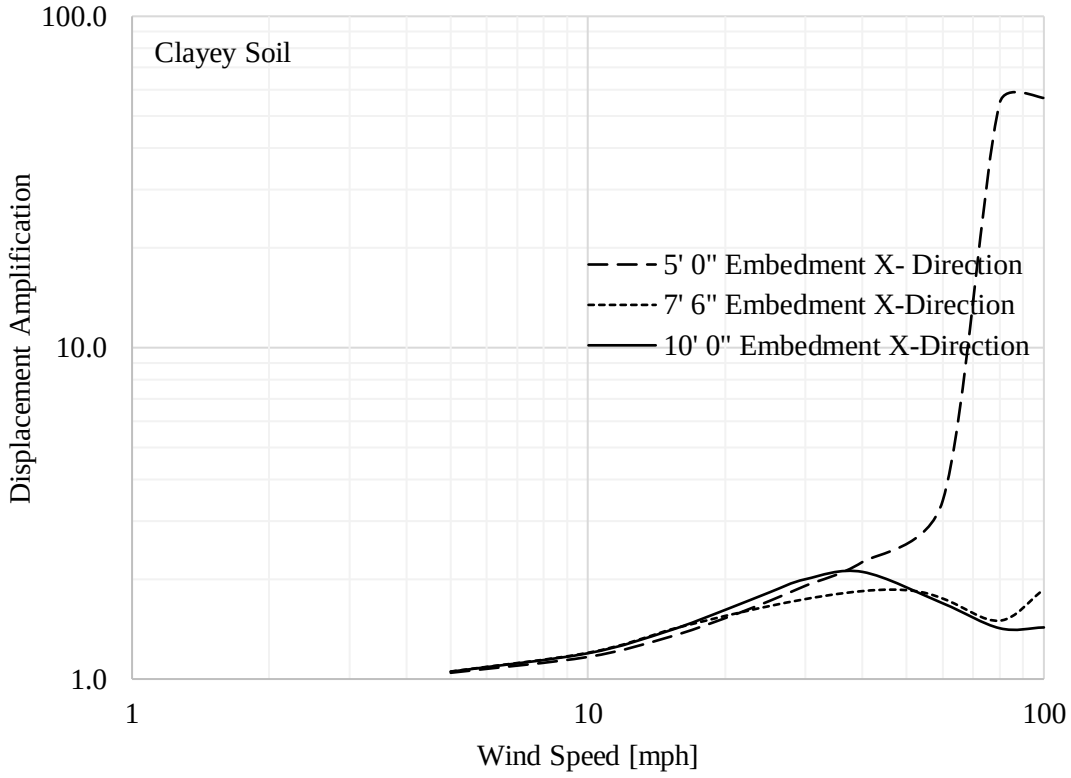

Figure 4-33. Displacement Amplification (X-Direction) in Clayey Soils

For 7’ 6’ (23.1%) and 10’ 0” (28.6%) embedment depths, the displacement amplification of 5.8 and 6.5 occurs at about 38 mph. There are two peaks for 5’ 0”

embedment depth. The first peak had 4.2 displacement amplification, and the second peak had 4.4 at 28 mph and 58 mph.

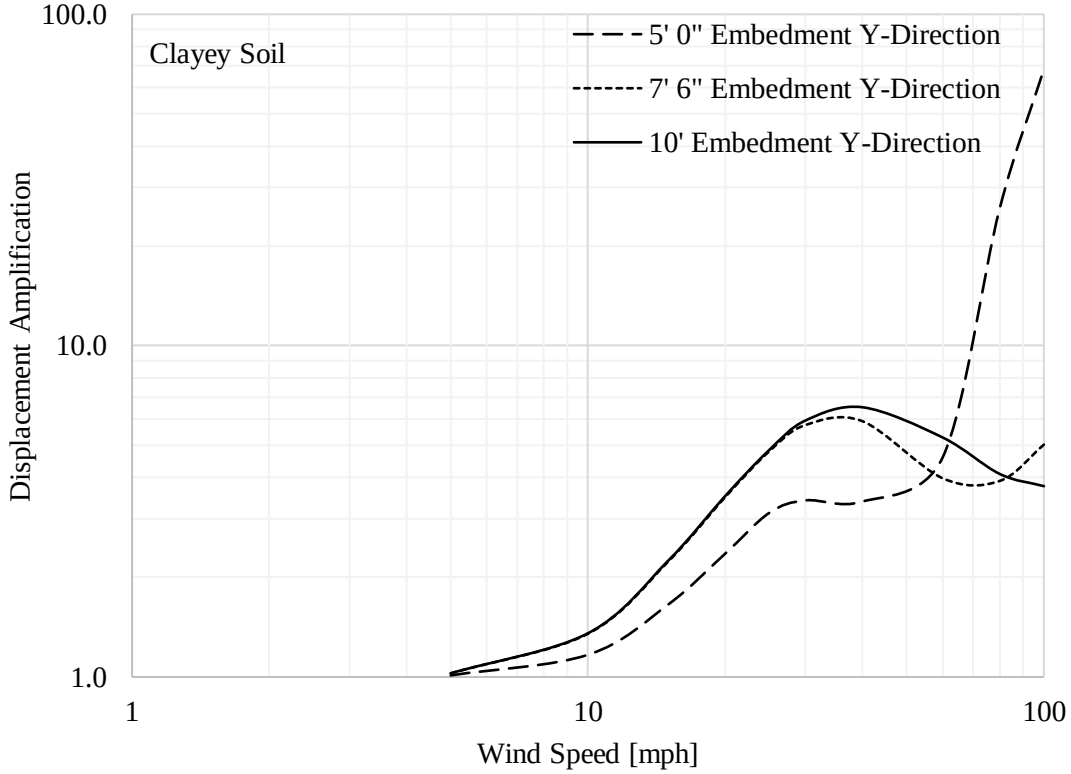

Figure 4-34. Displacement Amplification (Y-Direction) in Clayey Soils

There is a displacement amplification of 1.5 at about 38mph wind speed for 7’ 6” and 10’ 0” embedment depths for the X-direction wind. However, there is a significant displacement amplification of 6.3 at about 35mph.

For the 5’ 0” (16.5%) embedment depth of a class H1 wood pole, the maximum dynamic displacement amplification occurs at about 28 mph. There is imminent pole breakage of collapse beyond 50 mph.

Also, for 7’ 6” (23.1%) and 10’ 0” (28.6%) embedment depths, the maximum dynamic displacement amplifications occur at about 38 mph.

4.10 Cable Mass Ratio for Class H1 Pole with Cable

In this section, the cable mass ratio is reviewed, as well as its influence on the dynamic response of the class H1 wood pole. The cable used for this study is ½” diameter and 100 ft span.

Table 4-11: Cable Mass Ratio Vs Embedment Depths

S. NO	Embedment Depth [ft]	Weight of Wood Pole [kip]	Weight of Cable [kip]	Mass Ratio
1	10	0.90	0.067	7.46%
2	9.5	0.88	0.067	7.61%
3	9	0.86	0.067	7.78%
4	8.5	0.84	0.067	7.95%
5	8	0.83	0.067	8.12%
6	7.5	0.81	0.067	8.30%
7	7	0.79	0.067	8.48%
8	6.5	0.77	0.067	8.68%
9	6	0.76	0.067	8.87%
10	5.5	0.74	0.067	9.08%
11	5	0.72	0.067	9.29%

The cable mass ratios are shown in Table 4-11. In this table, the cable mass ratio varies with depth since the height above the ground level is constant. The maximum cable mass ratio is 9.29%. The effect of the cable mass ratio on the natural frequency is discussed in Section 4.7. A graph showing the effect of cable mass ratio on the natural frequency is

shown in Figure 4-25. A cable mass ratio less than 10% will have a minimal effect on the natural frequencies.

4.11 Proposed Tuned Mass Damper to Mitigate Resonance Vibration

This section proposes a Tuned Mass Damper to mitigate the resonance and displacement amplification in poles sensitive to resonance frequency dynamic wind forces.

The class H1 pole and the Tuned Mass Damper (TMD) are modeled as a two-degrees of freedom spring-mass system, as discussed in Section 3.22.

A sketch of the TMD is shown in Figure 4-35. The TMD consists of a 2” diameter steel rod (ASTM A36) and a 7 ½” diameter steel ball attached to the top of the steel rod.

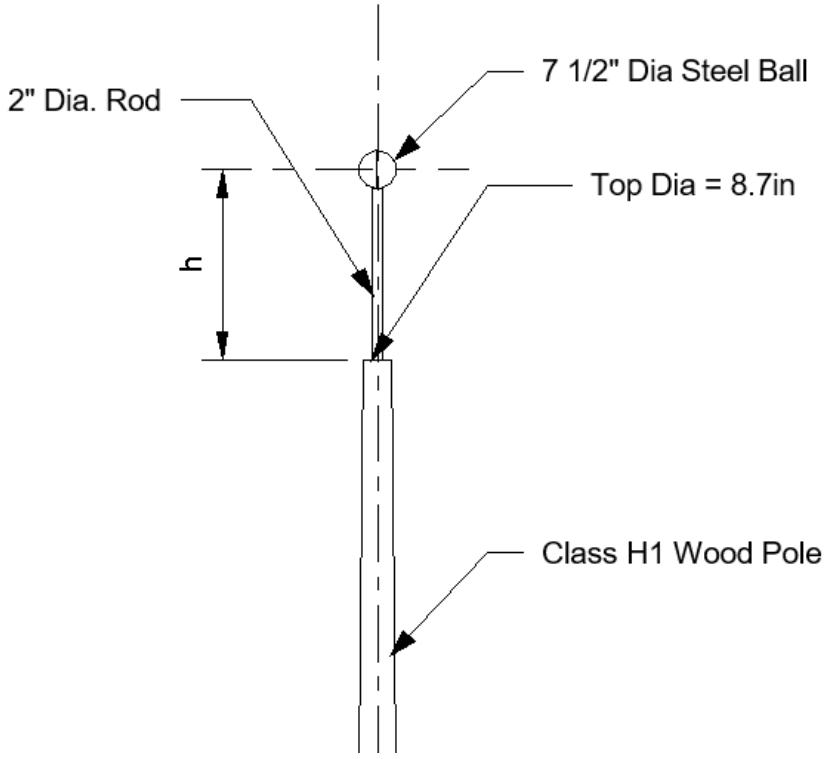

Figure 4-35. Sketch of Tuned Mass Damper

4.11.1 Dynamic Response of Class H1 Pole with TMD in Clayey Soils

The natural periods and frequencies of class H1 wood poles embedded in clayey soils are shown in Table 4-12. A designer can select a suitable mass and stiffness ratio to tune the system frequency to a desired level.

A typical natural frequency response of the wood pole with TMD is shown in Figure 4-36 for a 5’ 0” embedment depth. The graph is plotted on a logarithmic X-axis to visualize better the effect of the TMD mass and stiffness ratios. The resultant frequency response of the TMD is stable after a frequency ratio of 1.0 and remains relatively constant. However, the natural frequency of the pole continues to increase exponentially with the increase of the frequency ratio.

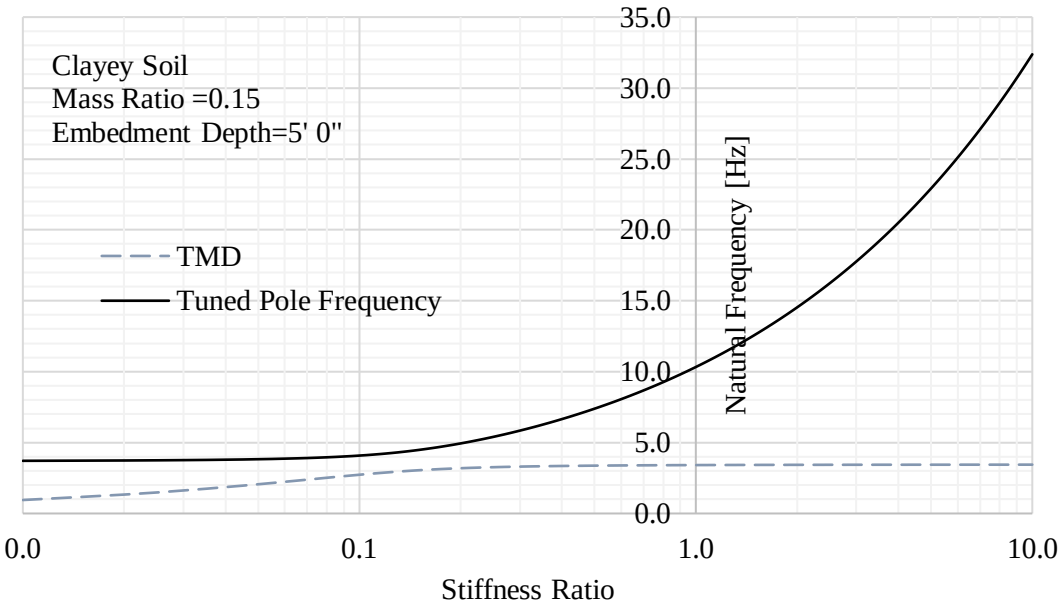

Figure 4-36. Natural Frequency Response of Pole with TMD for Clayey Soils

Table 4-12 shows the dynamic properties of the Class H1 pole embedded in clayey soils for various depths.

Table 4-12: Dynamic Properties of Class H1 Pole Embedded in Clayey Soils

S. NO	Embedment Depth [ft]	Period [sec]	Natural Frequency of Pole [Hz]	Model Mass Participation Ratio	ω [rad/s]	stiffness [k/in]
1	10	0.2286	4.3738	0.41	27.45	0.714
2	9.5	0.2293	4.3604	0.42	27.40	0.712
3	9	0.23	4.3475	0.43	27.32	0.708
4	8.5	0.231	4.3282	0.44	27.19	0.703
5	8	0.2326	4.2999	0.45	27.02	0.696
6	7.5	0.2348	4.2598	0.46	26.77	0.686
7	7	0.2379	4.2033	0.47	26.41	0.672
8	6.5	0.2424	4.1256	0.49	25.92	0.652
9	6	0.2488	4.0200	0.50	25.26	0.625
10	5.5	0.2578	3.8788	0.52	24.37	0.589
11	5	0.2708	3.6932	0.54	23.20	0.542

These natural frequencies need to be tuned to a higher frequency to mitigate the large displacement amplifications and prevent pole failures by installing a TMD at the top of the pole. A mass and stiffness ratio of 0.15 and 10, respectively, was used for this study.

Table 4-13 shows the dynamic analysis results for the TMD on the Class H1 Pole. The table also shows the weight, diameter, and height of the TMD rod or support. A stiffness ratio of 10 was used to determine the sizes of the TMD. The diameter of the TMD for a mass ratio of 0.15 is approximately 7 ½” in this example.

Table 4-13: Tuned Frequencies of Class H1 Pole Embedded in Clayey Soils

S. NO	Embedment Depth [ft]	Tuned Natural Frequency of Pole [Hz]	Tuned Natural Frequency of Damper [Hz]	Weight Of TMD [lbf]	Diameter Of TMD Rod [in]	Height of TMD Rod [in]
1	10	38.29	4.07	54.91	2	33.7
2	9.5	38.29	4.07	54.91	2	33.7
3	9	38.10	4.05	55.00	2	33.8
4	8.5	37.92	4.03	55.11	2	33.9
5	8	37.68	4.01	55.28	2	34
6	7.5	37.33	3.97	55.50	2	34.2
7	7	36.83	3.92	55.87	2	34.4
8	6.5	36.15	3.84	56.26	2	34.7
9	6	35.22	3.74	56.82	2	35.2
10	5.5	33.98	3.61	57.51	2	35.9
11	5	32.38	3.44	58.30	2	36.9

The effective increase in the tuned natural period and frequency of the class H1 pole is shown as a ratio of the natural frequency of the pole in Table 4-14. With a mass and frequency ratio of 0.15 and 10, the natural frequency increases by an average ratio of 8.86. The increase in the natural frequency of the pole due to the TMD is nearly a factor of 9.

Table 4-14: Frequency Increase Ratio for Class H1 Pole Embedded in Clayey Soils

S. NO	Embedment Depth [ft]	Natural Frequency Increase Ratio
1	10.0	8.75
2	9.5	8.78
3	9.0	8.76
4	8.5	8.76
5	8.0	8.76
6	7.5	8.76
7	7.0	8.76
8	6.5	8.76
9	6.0	8.76
10	5.5	8.76
11	5.0	8.77
Average		8.76

4.11.2 Dynamic Response of Class H1 Pole Embedded in Sandy Soils

The dynamic properties of a class H1 wood pole embedded in sandy soils are shown in Table 4-15. These values are used to calculate the tuned frequency response of the pole and TMD. The result of the analysis is shown in Table 4-16.

The frequency response graph for the TMD system for sandy soils is similar to clayey soil, as shown in Figure 4-37. As in the case of clayey soils, the frequency response of the TMD is stable beyond a frequency ratio of 1.0. However, the natural frequency response of the pole continues to increase as the frequency ratio of the TMD increases.

Error! Reference source not found.

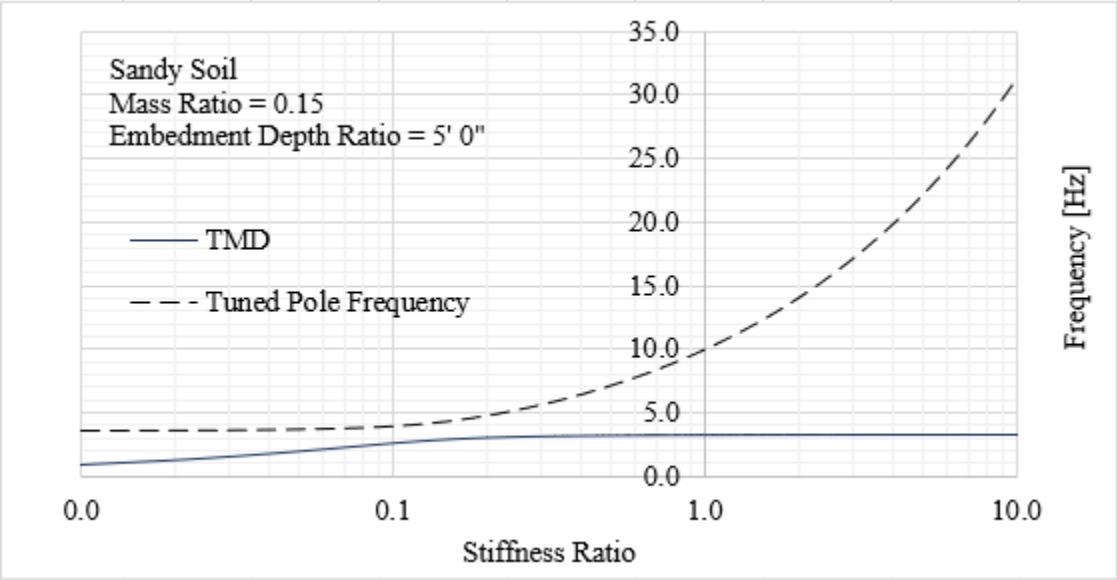

Figure 4-37. Frequency Response of Pole and Tuned Mass Damper

Since the natural frequency of the TMD remains constant beyond a frequency ratio of 0.2, it is valuable design information to tune the pole's natural frequency and the mass damper to a desired level without affecting the natural frequency of the TMD.

Table 4-15: Dynamic Properties of Class H1 Pole Embedded in Sandy Soils

S. NO	Embedment Depth [ft]	Period [sec]	Natural Frequency of Pole [Hz]	Modal Mass Participation Ratio	Modal Mass [kip-s^2/in]	ω [rad/s]	stiffness [k/in]
1	10	0.24	4.18	0.43	0.0009898	26.29	0.684
2	9.5	0.24	4.18	0.44	0.0009911	26.25	0.683
3	9	0.24	4.16	0.45	0.0009920	26.17	0.679
4	8.5	0.24	4.14	0.46	0.0009950	26.09	0.677
5	8	0.24	4.11	0.47	0.0010035	25.81	0.668
6	7.5	0.25	4.06	0.48	0.0010058	25.48	0.653
7	7	0.25	3.98	0.50	0.0010157	24.99	0.634
8	6.5	0.26	3.87	0.51	0.0010270	24.29	0.606
9	6	0.27	3.71	0.53	0.0010421	23.31	0.566
10	5.5	0.29	3.50	0.55	0.0010593	22.01	0.513
11	5	0.31	3.23	0.58	0.0010772	20.32	0.445

Table 4-16: Tuned Frequencies of Class H1 Pole Embedded in Sandy Soils

S. NO	Embedment Depth [ft]	Tuned Natural Frequency of Pole [Hz]	Tuned Natural Frequency of Damper [Hz]	Weight Of TMD [lbf]	Diameter Of TMD Rod [in]	Height of TMD Rod [in]
1	10.0	36.66	3.90	57.4	2	34.2
2	9.5	36.61	3.89	57.4	2	34.2
3	9.0	36.49	3.88	57.4	2	34.3
4	8.5	36.38	3.87	58.2	2	34.5
5	8.0	36.21	3.85	58.3	2	34.3
6	7.5	35.54	3.78	58.3	2	34.7
7	7.0	34.85	3.70	58.9	2	35.1
8	6.5	33.88	3.60	59.5	2	35.6
9	6.0	32.51	3.46	60.4	2	36.4
10	5.5	30.69	3.26	61.4	2	37.6
11	5.0	28.35	3.01	62.4	2	39.5
Average		34.4	3.7	59.0	-	35.5

The relative increase ratio of the pole frequency is shown in Table 4-17. The average increase in the natural frequency of the pole due to the TMD is approximately 8.76. or nearly 9.

Table 4-17: Frequency Increase Ratio for Class H1 Pole Embedded in Sandy Soils

S. NO	Embedment Depth [ft]	Natural Frequency Increase
1	10.0	8.76
2	9.5	8.76
3	9.0	8.76
4	8.5	8.78
5	8.0	8.82
6	7.5	8.76
7	7.0	8.76
8	6.5	8.77
9	6.0	8.76
10	5.5	8.76
11	5.0	8.76
	Average	8.77

The increase in the natural frequency appears to be the same for both sandy and clayey soils, also independent of the depth of embedment depth.

CHAPTER V

5 CONCLUSIONS AND FUTURE RESEARCH

5.1 Conclusions

Based on the soil-structure interaction study of wood utility poles both with and without cables, the following conclusions are drawn:

1 The natural frequency response of the test wood poles predicted by the finite element analysis agreed well with that observed experimentally.

2 The theoretical models formulated predict the critical wind speeds and embedment depths beyond which catastrophic pole rupture and excessive ground displacements occur.

3 The natural frequency of the wood pole decreases almost exponentially with an increase in the cable mass to the wood pole mass ratio.

4 A six-fold displacement amplification occurs at the tip of the Class H1 pole at a wind speed of 40 mph perpendicular to the plane of the cable and 30 mph along the plane of the cable in both sandy and clayey foundation soils.

5 A nine-fold increase in the natural frequency was achieved when a tuned mass damper with mass and stiffness ratios of 0.15 and 10 was mounted at the top of the Class H1 pole embedded in sandy and clayey foundation soils.

6 The tapered wood test pole exhibited a bending-type breakage at its mid-height, followed by a longitudinal laminar separation of the wood fibers.

7 No Class H1 wood pole breakage occurs when the wind speed is less than 160 mph in the plane of the cable for clayey soils, provided the embedment depth is greater than or equal to 5’ 6”.

8 No Pole breakage will occur for all embedment depths in sandy soils for wind speeds up to 120 mph and all embedment depths considered for sandy soils.

9 A non-linear relationship between the wind speed and pole breakage location above the ground level is observed.

10 The analysis shows that the higher the wind speed, the higher the breakage point from the ground level.

The study shows that the soil stiffness, presence of cables, and frequency of the wind speeds influence the natural frequency response of the wood pole. In addition, a tuned mass damper provides an effective method to mitigate the effects of resonance by increasing the natural frequency of the Class H1 wood pole. Based on the dynamic analysis presented, the catastrophic utility pole breakage and excessive foundation soil deformations can be predicted and prevented.

5.2 Future Research

The damping ratio of the soil has a considerable effect on the dynamic response of a Soil-Structure system, which needs further investigation. Additional studies can include partial saturation of the soil. Increased moisture content or age of wood utility poles can affect the physical properties of the pole. Further investigation of the dynamic properties of wood utility poles with varying moisture contents, including the age of the poles, would provide insight into the life cycle performance of the wood utility poles.

6 REFERENCES

[1] M. D. B. Brent Baker, "Are Wood Poles Getting Weaker?," Electrical Transmission and Substation Structres, 2009.

[2] National Electric Safety Code, Standard IEEE, 2007.

[3] H. Hussein, "Effectiveness of Suspended Lead Dampers in Steel Buildings Effectiveness of Suspended Lead Dampers in Steel Buildings Under Localized Lateral Impact and Vertical Pulsating Load Under Localized Lateral Impact and Vertical Pulsating Load," 2022.

[4] H. Hussein and Z. Razzaq, "CFRP Retrofitting Schemes for Prestressed Concrete Box Beams for Highway Bridges," Global Journal of Researches in Engineering, vol. 17, 01/15 2017.

[5] H. Hussein and Z. Razzaq, "Prestressed Concrete Inverted Tee Beams with CFRP for Building Structures," Global Journal of Researches in Engineering, vol. 17, 07/15 2017.

[6] F. H. F. Elizabeth Calvert, "A review of Current Wind Load Provisions for Tansmission Pole Structures," ASCE, 2000.

[7] B. Lacoursiere, "Steel utility poles: advantages and applications," in 1999 Rural Electric Power Conference (Cat. No. 99CH36302), 1999: IEEE, pp. B2/1-B212.

[8] a. J. W. W. A. B. Peabody, "Buckling of Wood Power Poles Using Finite Elements," Journal Of Structural Engineering, 1983.

[9] N. D. Farhang Ostadan, Jose M. Roesset, "Estimating Total System Damping for SoilStructure Interaction Systems," presented at the Estimating Total System Damping for SoilStructure Interaction Systems, Menlo Park, California, USA, 2004.

[10] L. Kemper, "ASCE Guide for Design of Substation Structures," Lifeline Earthquake Engineering in a Multihazard Environment, no. 262, 2009.

[11] Wood Pole Structures for Electrical Transmission Lines: Recommended Practice for Design and Use, ASCE 2019.

[12] T. N. Bowmer, "National Electric Safety Code (NESC) Update," 2021.

[13] A. Shafieezadeh, U. P. Onyewuchi, M. M. Begovic, and R. DesRoches, "Age-dependent fragility models of utility wood poles in power distribution networks against extreme wind hazards," IEEE Transactions on Power Delivery, vol. 29, no. 1, pp. 131-139, 2013.

[14] D. M. Siringoringo, Y. Fujino, A. Nagasaki, and T. Matsubara, "Seismic performance evaluation of existing light poles on elevated highway bridges," Structure and Infrastructure Engineering, vol. 17, no. 5, pp. 649-663, 2021.

[15] Wood Utility Pole Design Values in the NESC, N. A. W. P. Council.

[16] Wood Pole Design Considerations, N. A. W. P. Council.

[17] D. R. Bohnhoff, "Modelling Soil Behavior With Simple Springs," Frame Building, 2014.

[18] D. M. Hossein Quarib, Phd, PE, "Analysis, Prediction, and Mitigation of Vortex Induxed Vibration in Substation Structures," Electrical Transmission and Substation Structures, 2015.

[19] P. Daryl Boggs, PE, "Challenges in Design and Mitigation of Wind-Induced Vibration for Slender Steel Pole Transmission Structures," Electrical Transmission and Substation Structures, 2018.
[20] P. Fred H. Kulhawy, Anwar Hirany, PE, "Foundation Engineering for Transmission Line Structures," presented at the ASCE, 2010.
[21] Wood Utility Pole Design Values in the NESC, N. A. W. P. Council, 2018.
[22] Guidelines for Electrical Transmission Line Structural Loading, ASCE, 2009.
[23] C. M. Sivapalan Gajan, "Improved Design of Embedment Depths for Transmission Pole Foundations Subject to Lateral Loading," ASCE, no. 2010, 2010.

APPENDIX

6.1 Appendix A: Drawing of Test Frame

A drawing of the experimental test frame is shown in this section. Figure 6-1 and Figure 6-2 show a plan and section view of the test frame. The test frame is fabricated using 2-1/2” x 2-1/2” x ¼” steel angles. The frame's base is provided with a ½” bolt hole to secure the base of the frame to the concrete floor if needed.

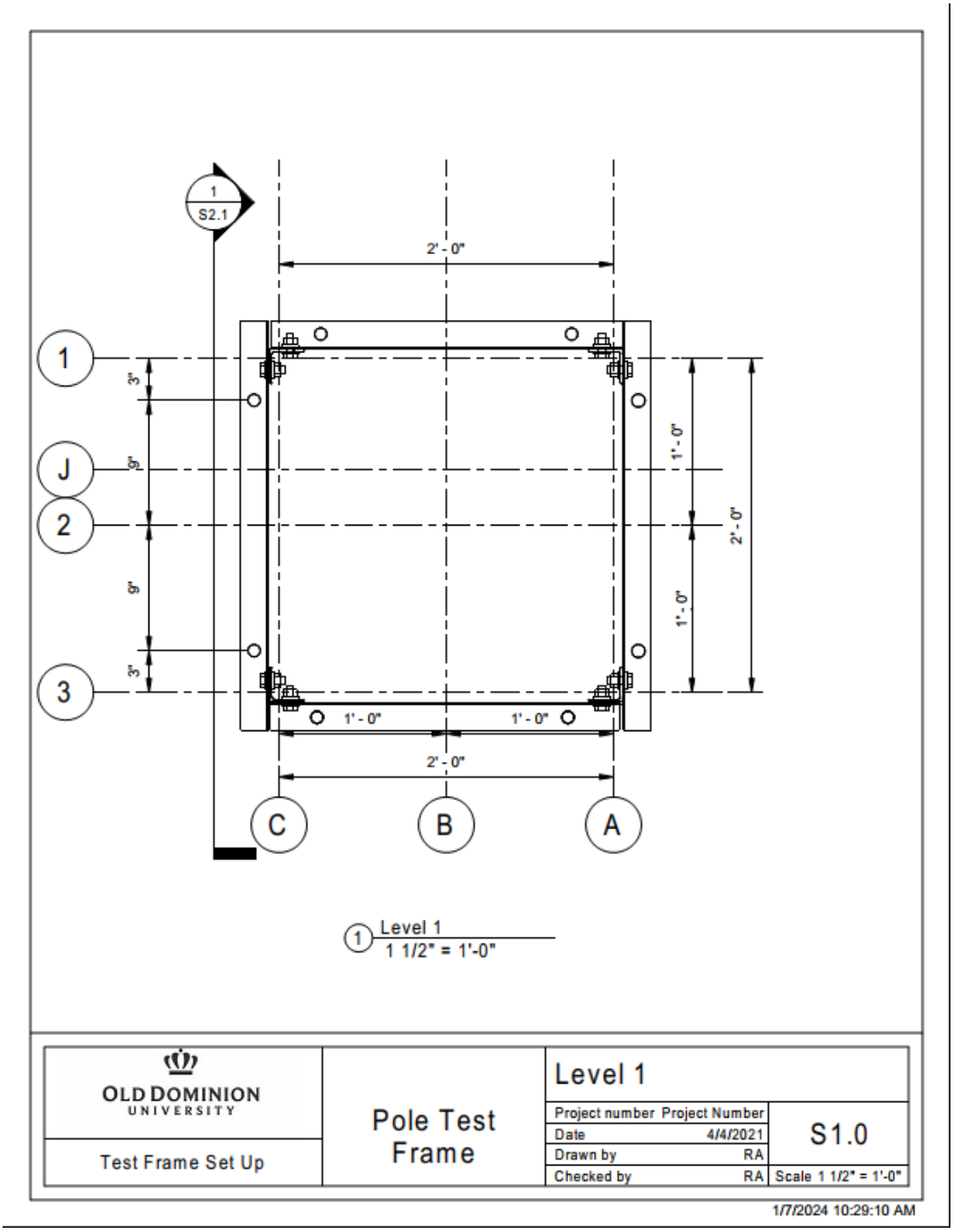

Figure 6-1. Plan View of Test Frame

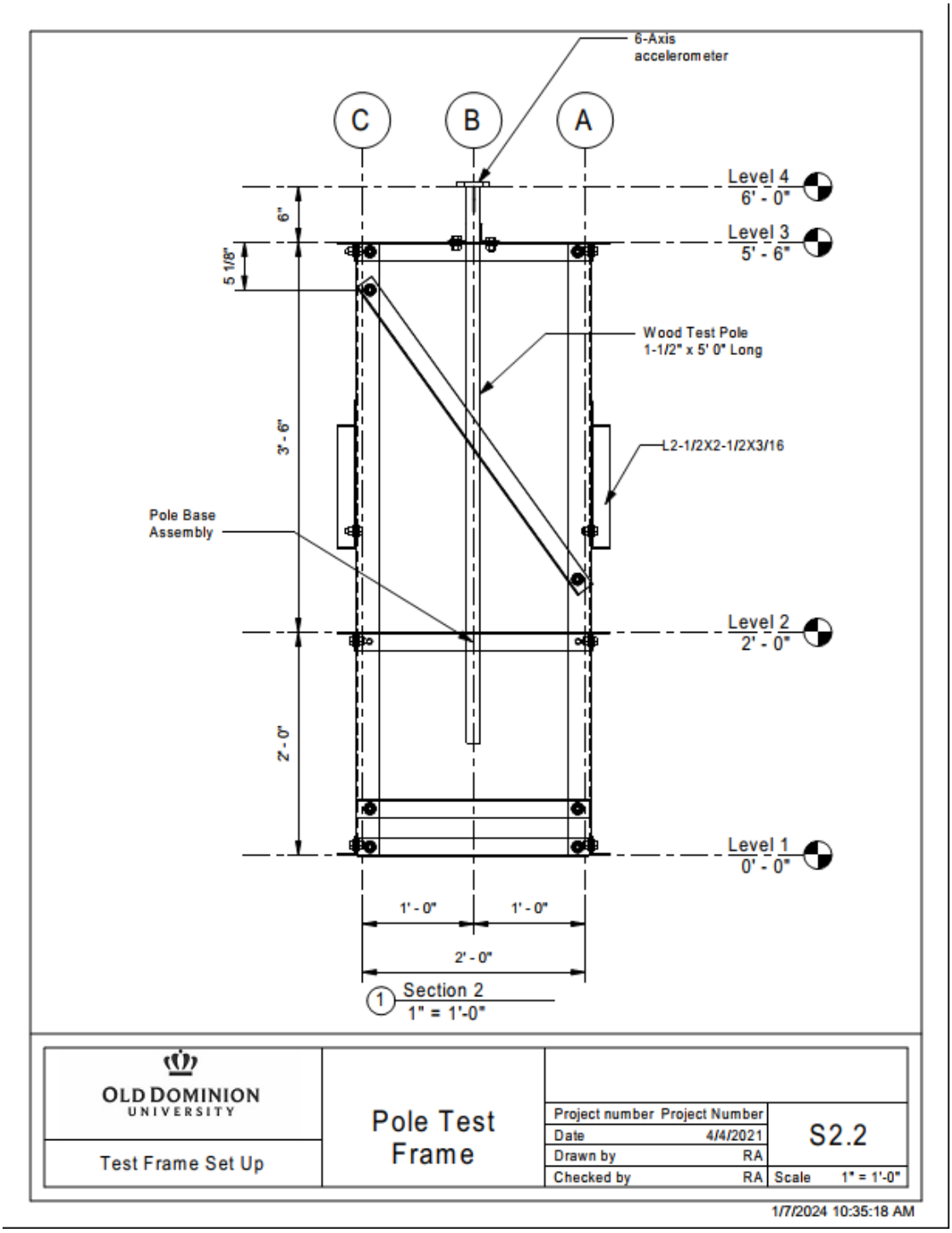

Figure 6-2. Section View of Test Frame.

6.2 Appendix B: Pictures of Test Frame Set-up

Figure 6-3. Picture of Test Frame

Figure 6-4. Test Frame with Cable and Digital Load Gage

Figure 6-5: 4' 0" Test Specimen and Base Connection

Figure 6-6: Digital Load Gag to Measure Cable Tension

Figure 6-7. 6' 0" Test Pole with Fixed Base Attachment

6.3 Appendix C. Picture of Test Pole Breakage

Details of the test pole breakage are presented in this section. Figure 6-8, Figure 6-9, and Figure 6-10, show pictures of the test pole breakage. The pole breakage initiated at the pole's base, extending roughly 26 inches.

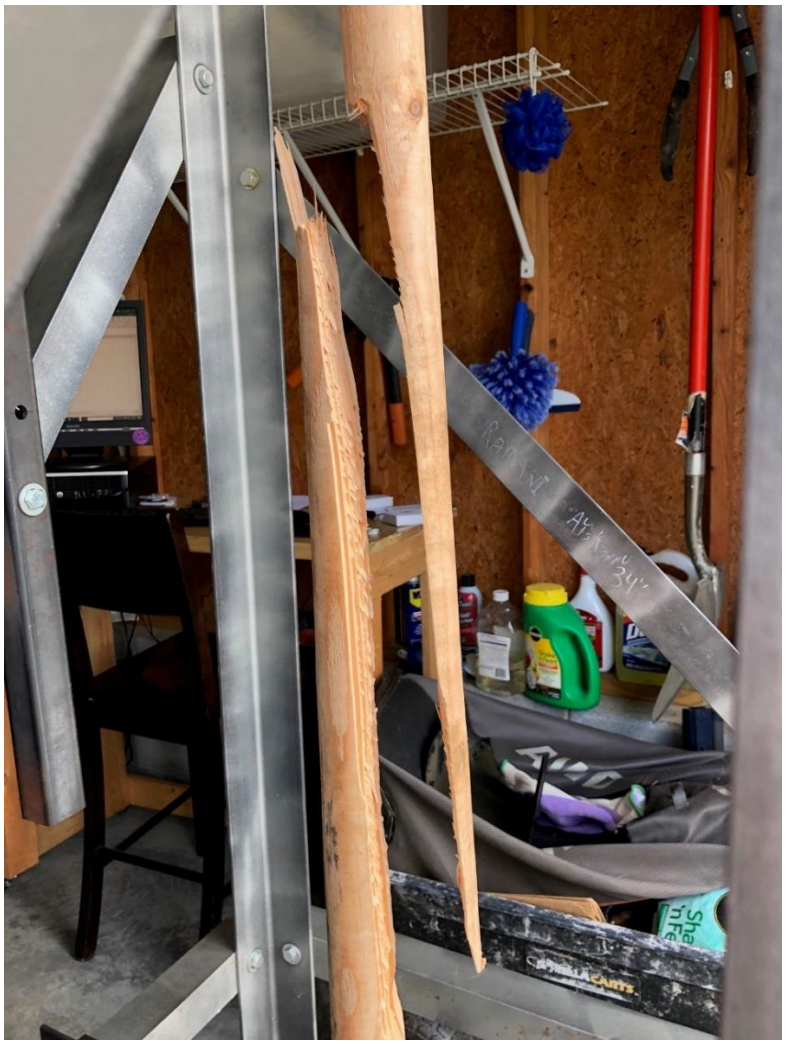

Figure 6-8. Test Pole Failure, Top and Bottom Sections

Figure 6-9: Test Pole Failure Profile

Figure 6-10. Test Pole Breakage Measurements

The tapered wood test pole exhibited a bending-type breakage at its mid-height, followed by a longitudinal laminar separation of the wood fibers.

6.4 Appendix C: Pictures of Ceder Wood Species.

Some pictures of the cedar Wood species are shown in this section.

Figure 6-11: Picture of Western Cedar Trees

Cedar trees grow in various parts of North America and worldwide. They can grow 100 feet or more. Common Cedarwood types are Western Red Cedar, Northern White

Cedar, Eastern Red Cedar, Alaskan Cedar, and Spanish Cedar Wood. The Western Red Cedar trees can grow up to 200 feet.

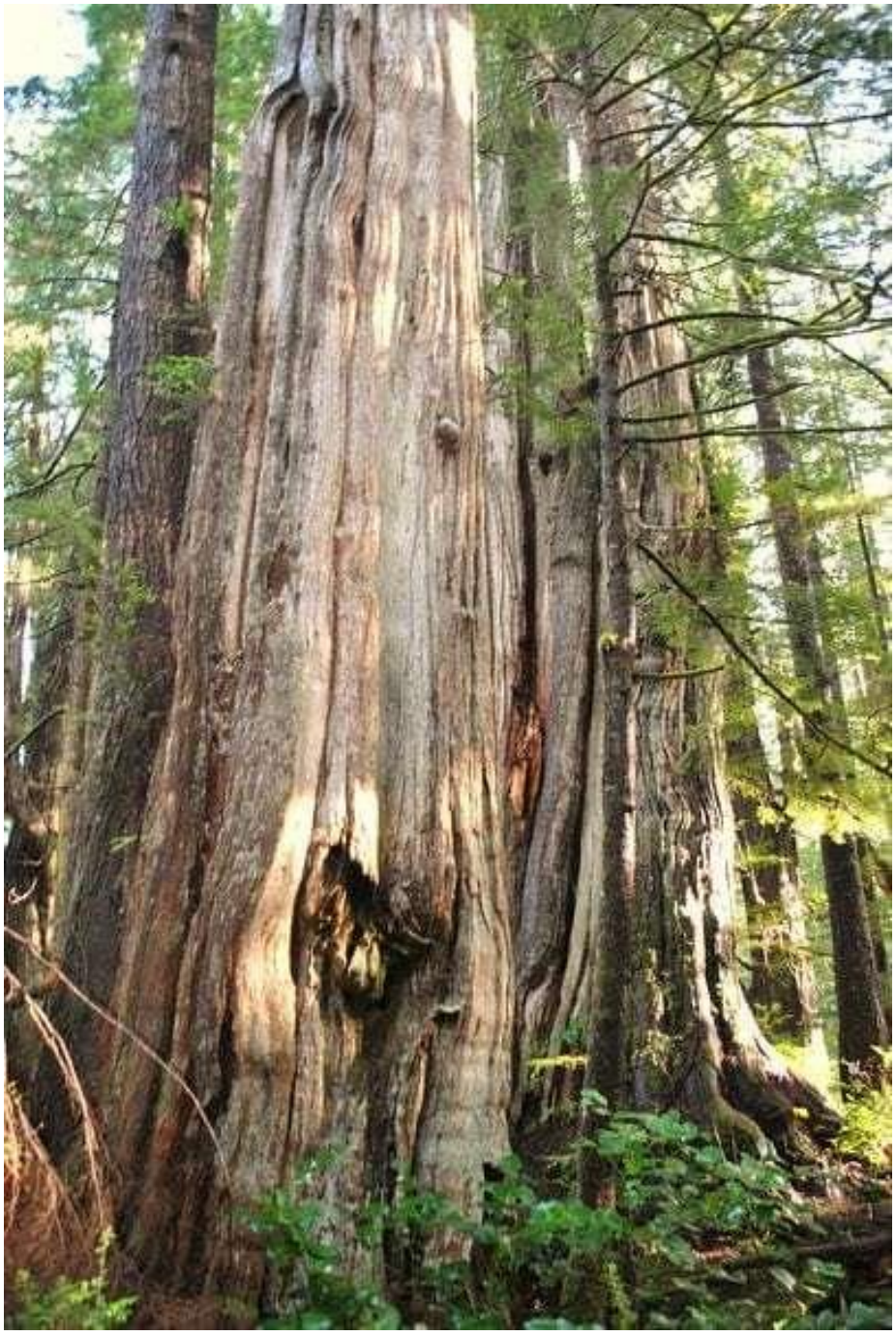

Figure 6-12: Picture of Western Cedar Trees

6.5 Appendix D: Accelerometer Information

This section provides information about the accelerometer used to measure the acceleration for the test program.

6.5.1 Accelerometer Specification

Manufacturer: WitMotion Shen Zhen Co., Ltd

Website: WitMotion (witmotion-sensor.com)

Model: WT61, WT931

Both accelerometers have the following specifications:

Specifications	
Chip	MPU6050
Voltage	3.3-5V
Current	＜10mA
Interface	Serial TTL/IIC communication
Output	3-axis acc+ gyro+angle
Gryo Range	±2000 deg/s
Acc Range	16g
Angle Range	X, Z axis: ±180° Y axis: ±90°
Accuracy	Static: 0.05° Dynamic 0.1°
Rate	9600 (baud rate) 20Hz output
Baud Rate	115200 (baud rate) 100Hz output

6.6 Appendix E: MATLAB code

A MATLAB code was developed to validate and compare from experimental, and SAP2000 analysis is shown in this section.

Utility Pole Analysis MATLAB Code

- The following MATLAB code performs dynamic analysis of Utility Poles.
- Finite Element Analysis is used to formulate the Mass and Stiffness Matrices
- The analysis is based on consistent mass and stiffness matrices.
- The accuracy is dependent of the number of elements selected.

6.6.1 Initialization

```
clc;
close;
clear;
format short;
```

6.6.2 Input Data

6.6.3 Joint Coordinates

Column 1 is Joint labels

Column 2 is X coordinate of Joint i, [ft]

Column 3 is Y coordinate of joint i, [ft]

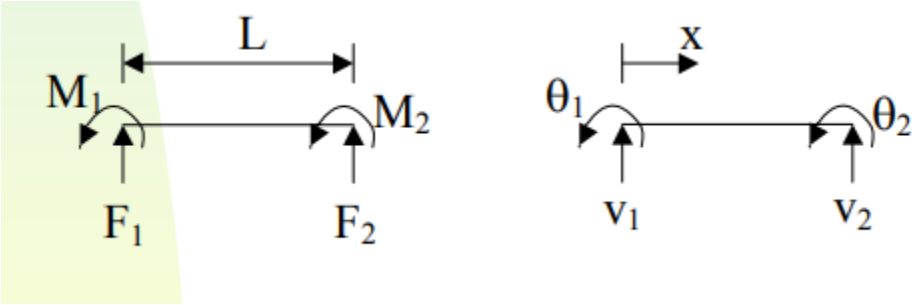

Figure 6-13: Element Nodal Displacements and Forces

6.6.4 Read Excel Data

The properties of the pole (length, number of nodes, coordinates, areas and Moment of Inertias are prepared in an excel spreadsheet and saved in the "MemberProperties.xlsx" file. This excel file is read into the program using the MATLAB code below.

```
opts = spreadsheetImportOptions("NumVariables", 9);


% Specify sheet and range
opts.Sheet = "Sheet1";
opts.DataRange = "A2:I200";   % Change I200 for large data.


% Specify column names and types
opts.VariableNames = ["JointNumber", "XCordinate", "YOrZCordinate",
"Var4", "MemberNumber", "i", "j", "AreaIn2", "Iin4"];
opts.SelectedVariableNames = ["JointNumber", "XCordinate",
"YOrZCordinate", "MemberNumber", "i", "j", "AreaIn2", "Iin4"];
opts.VariableTypes = ["double", "double", "double", "char", "double",
"double", "double", "double", "double"];


% Specify variable properties
opts = setvaropts(opts, "Var4", "WhitespaceRule", "preserve");
opts = setvaropts(opts, "Var4", "EmptyFieldRule", "auto");


% Import the data
MemberProperties =
readtable("C:\Users\AYAKR\Documents\MATLAB\Programs\Pole
Analysis\MemberProperties.xlsx", opts, "UseExcel", false);
```

```
JC=table2array(MemberProperties(:,1:3));
idx=isnan(JC(:,1));
JC=JC(~idx,:);


numJointsA=JC(end,1);
```

6.6.5 Member Properties

Column 1 is member number.

Column 2 is starting joint, j

Column 3 is ending joint, k

Column 4 is Cross-section area [in^2]

Column 5 is Moment of Inertia [in^2]

E=Young's Modulus of Pole [ksi]

```
MP=table2array(MemberProperties(1:(end-1),4:8));
idx=isnan(MP(:,1));
MP=MP(~idx,:);
E=2000;                  % Young's Modulus Of Material [ksi]
MatDen=34.5;             % Density Of Material [pcf]
MatDen=MatDen/(1000*12*12*12);           % Mass Density [kci]
```

6.6.6 Joint Restraints

uu - is the unrestrained joint displacements.

rr -is the restrained joint displacements.

U- is the Joint Labels

```
nj=size(JC);
numJoints=nj(1,1);
nm=size(MP);
numelements=nm(1,1);
```

```
DOF=numJoints*3;


uu=4:DOF;                                          % Unrestrained Joint
Displacements
rr=1:3;                                            % Restrained Joints
Displacements
U=1:DOF;
Dr=[0 0 0 0];


nuu=size(uu);                                      % Number of Joint
Displacements
nrr=size(rr);                                      % Number of Restrained
Displacements


Nuu=nuu(1,end);
Nrr=nrr(1,end);
Suurr=Nuu+Nrr;


if Suurr-DOF==0
   disp('Inputs Ok')
else
   disp('Check Input for uu and rr')


end
```

```
Inputs Ok
```

6.6.7 Joint Loads

```
JL=zeros(Nuu,1);                          % Joint Loads


% JL(4)=0;
JLuu=JL(Nuu,1);
Jrr=JL(rr,1);
```

6.6.8 Member Loads

6.6.9 Initial Conditional

```
u0(:,1)=zeros(Nuu,1);
v0(:,1)=zeros(Nuu,1);
u0(end,1)=0.1;
```

6.6.10 Mass and Stiffness Matrices

```
KG=zeros(DOF,DOF);
w=zeros(numelements,1);
m=zeros(numelements,1);
MG=zeros(DOF,DOF);
A=zeros(numelements,1);
I=zeros(numelements,1);
[KG, MG]=MASSandSTIFFNESS(MP,JC,numelements,MatDen,DOF,E);
MG;
KG;
Kuu=KG(uu,uu);
Kur=KG(uu,rr);
Kru=KG(rr,uu);
Krr=KG(rr,rr);
Muu=MG(uu,uu);
```

6.6.11 Compute Dynamic Properties

Periods and Natural frequencies are calculated in this section

```
[v,d]=eig(Kuu,Muu);
phi=v;
Mode1a=phi(1:3:end,1);
Mode2a=phi(1:3:end,2);
Mode3a=phi(1:3:end,3);
Mode4a=phi(1:3:end,4);
Mode1b=Mode1a(end,1);
Mode2b=Mode2a(end,1);
Mode3b=Mode3a(end,1);
Mode4b=Mode4a(end,1);
Mode1=phi(1:3:end,1)/Mode1b;
Mode2=phi(1:3:end,2)/Mode2b;
Mode3=phi(1:3:end,3)/Mode3b;
Mode4=phi(1:3:end,4)/Mode4b;
omega=diag(d);
```

```
omegan=sqrt(omega);
tn=2*pi./omegan;
Tn=tn(1:3:end);
Freq=real(1./Tn);
T0=Tn(1)
T0 = 0.0421
Fn=Freq(1)
Fn = 23.7254
```

6.6.12 Damping Matrix

The damping Matrix is computed based on Raleigh's damping.

```
Eksi1=5;                   % Damping Ratio for Frequency 1
Eksi2=5;                  % Damping Ratio for Frequency 2
Eksi1=(Eksi1/100);
Eksi2=(Eksi2/100);
omega1=omega(1,1);
omega2=omega(7,1);
AA=[1/omega1 omega1;
    1/omega2 omega2];
zn=(1/2)*inv(AA)*[Eksi1
             Eksi2];
alpha=zn(1);
beta=zn(2);
Cuu=Muu*alpha+Kuu*beta;
```

6.6.13 Mass Normalized Matrix

```
KNor=phi'*Kuu*phi;
MNor=phi'*Muu*phi;
CNor=phi'*Cuu*phi;
```

6.6.14 Plot Mode Shapes

```
yaxis=0:numelements;
figure()
Mode1=[0;Mode1];
Mode2=[0;Mode2];
Mode3=[0;Mode3];
Mode4=[0;Mode4];
subplot(1,4,1)
plot(Mode1,yaxis);
grid on;
```

```
grid minor;
xlim([-1.25 1.25]);


subplot(1,4,2);
plot(Mode2,yaxis);
grid on;
grid minor;
xlim([-1.25 1.25]);


subplot(1,4,3);
plot(Mode3,yaxis);
grid on;
grid minor;
xlim([-1.25 1.25]);


subplot(1,4,4);
plot(Mode4,yaxis);
grid on;
grid minor;
xlim([-1.25 1.25]);
```

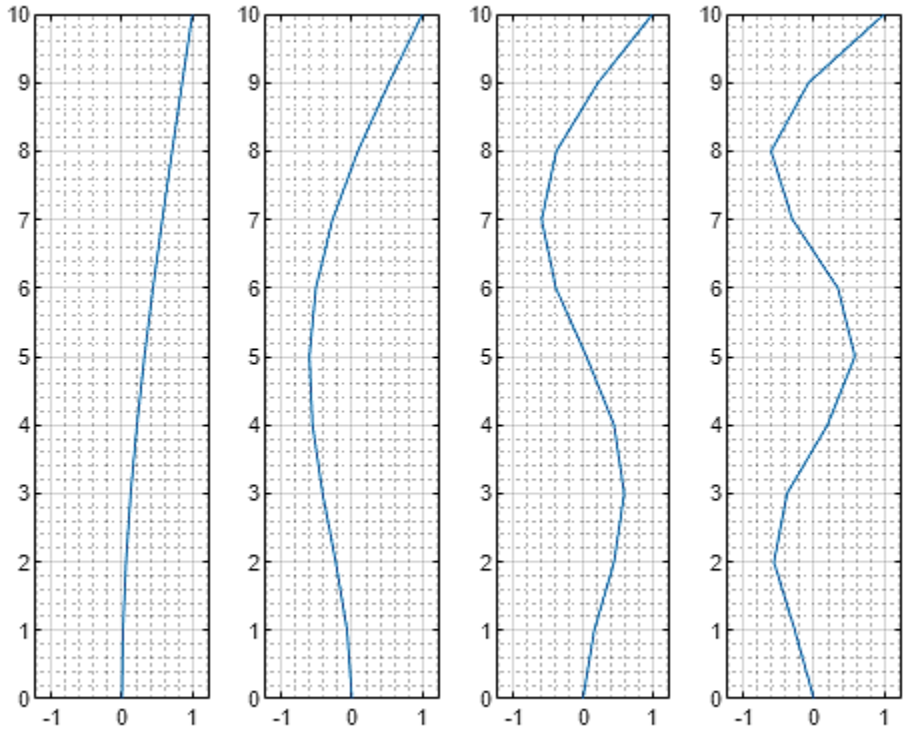

Figure 6-14: Mode Shapes

6.6.15 Plot Analysis Frame

```
figure()
for i=1:numelements
      n1=MP(i,2);
      n2=MP(i,3);
      x=[JC(n1,2) JC(n2,2)];
      y=[JC(n1,3) JC(n2,3)];
      plot(x,y,LineWidth=3)
      hold on;
end
grid on;
grid minor;
xmax=max(JC(:,2));
```

```
xmin=min(JC(:,2));
ymax=max(JC(:,3));
ymin=min(JC(:,3));
xlim([(xmin-0.5) (xmax+0.5)]);
ylim([(ymin),(ymax*1.05)]);
```

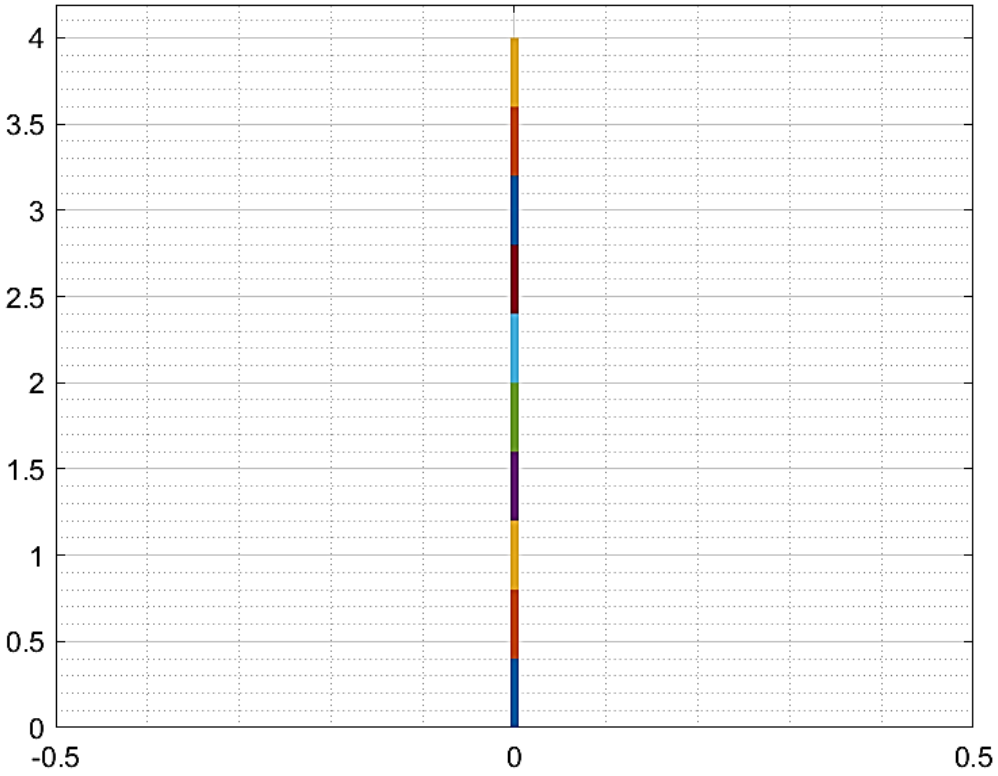

Figure 6-15: Plot of Elements

6.7 Appendix F: Utility Pole Classification and technical information

This section provides data on the pole sizes, classification and technical information of the wood utility poles.

Pole Sizes and Technical Information

Our poles are manufactured to meet minimum tip load and moment capacity equivalents of wood poles under NESC Grade B construction. We manufacture poles in Classes 1 through 3, from 30 feet to 95 feet and H Class poles in strength ratings to Class H10 and heights up to 95 feet. See tables below for pole information.

CLASS 3

Length (Ft.)	Part No.	Full Truck Qty (2 Pcs.)	Stand. Weight (Lbs.)	Tip Dia. (In.)	Base Dia. (In.)	Allow. Tip Load (Kips)	Ground Line Capacity (Kip-Ft.)	ANSI Embed Depth (Ft.)
30	C3030	42	650	6.0	11.3	1.95	43.9	5.5
35	C3053	42	786	6.0	11.9	1.95	52.7	6.0
40	C3040	41	980	6.0	12.8	1.95	64.2	6.0
45	C3045	35	1139	6.0	13.8	1.95	71.2	6.5
50	C3050	31	1310	6.0	14.4	1.95	80.0	7.0
55	C3055	26	1549	6.0	15.3	1.95	88.7	7.5
60	C3060	23 [15]	1737	6.0	16.3	1.95	97.5	8.0
65	C3065	19 [12]	1937	6.0	17.2	1.95	106.3	8.5
70	C3070	16 [12]	2232	6.0	17.8	1.95	115.1	9.0
75	C3075	15 [10]	2450	6.0	18.4	1.95	123.8	9.5
80	C3080	13 [10]	2680	6.0	19.4	1.95	132.6	10.0

CLASS 2

Length (Ft.)	Part No.	Full Truck Qty (2 Pcs.)	Stand. Weight (Lbs.)	Tip Dia. (In.)	Base Dia. (In.)	Allow. Tip Load (Kips)	Ground Line Capacity (Kip-Ft.)	ANSI Embed Depth (Ft.)
30	C2030	42	749	6.0	11.2	2.41	54.1	5.5
35	C2035	42	906	6.0	11.7	2.41	64.9	6.0
40	C2040	35	1137	6.0	12.7	2.41	77.0	6.0
45	C2045	30	1326	6.0	13.6	2.41	87.8	6.5
50	C2050	26	1530	6.0	14.6	2.41	98.6	7.0
55	C2055	22	1824	6.0	15.1	2.41	109.4	7.5
60	C2060	19 [15]	2055	6.0	16.0	2.41	120.3	8.0
65	C2065	16 [15]	2302	6.0	17.0	2.41	131.1	8.5
70	C2070	13 [12]	2665	6.0	17.5	2.41	141.9	9.0
75	C2075	12 [10]	2934	6.0	18.4	2.41	152.7	9.5
80	C2080	11 [10]	3218	6.0	19.4	2.41	163.5	10.0
85	C2085	10 [10]	3644	6.0	19.8	2.41	174.4	10.5
90	C2090	9 [8]	3939	6.0	20.8	2.41	185.2	11.0
95	C2095	8 [8]	4250	6.0	21.8	2.41	196.0	11.5

CLASS 1

Length (Ft.)	Part No.	Full Truck Qty (2 Pcs.)	Stand. Weight (Lbs.)	Tip Dia. (In.)	Base Dia. (In.)	Allow. Tip Load (Kips)	Ground Line Capacity (Kip-Ft.)	ANSI Embed Depth (Ft.)
30	C1030	42	896	6.0	11.4	2.93	65.8	5.5
35	C1035	37	1083	6.0	11.7	2.93	79.0	6.0
40	C1040	30	1351	6.0	12.7	2.93	93.6	6.0
45	C1045	25	1571	6.0	13.6	2.93	106.8	6.5
50	C1050	22	1808	6.0	14.6	2.93	119.9	7.0
55	C1055	19	2140	6.0	15.1	2.93	133.1	7.5
60	C1060	16 [15]	2400	6.0	16.0	2.93	146.3	8.0
65	C1065	13 [15]	2677	6.0	17.0	2.93	159.4	8.5
70	C1070	11 [12]	3087	6.0	17.5	2.93	172.6	9.0
75	C1075	10 [10]	3389	6.0	18.4	2.93	185.7	9.5
80	C1080	9 [10]	3708	6.0	19.4	2.93	198.9	10.0
85	C1085	8 [8]	4198	6.0	19.9	2.93	212.1	10.5
90	C1090	8 [8]	4540	6.0	20.9	2.93	225.2	11.0
95	C1095	7 [8]	4901	6.0	21.9	2.93	238.4	11.5

CLASS H1

Length (Ft.)	Part No.	Full Truck Qty (2 Pcs.)	Stand. Weight (Lbs.)	Tip Dia. (In.)	Base Dia. (In.)	Allow. Tip Load (Kips)	Ground Line Capacity (Kip-Ft.)	ANSI Embed Depth (Ft.)
30	H1030	36	1018	8.7	14.1	3.51	79.0	5.5
35	H1035	30	1204	8.7	14.5	3.51	94.8	6.0
40	H1040	25	1526	8.7	15.5	3.51	112.3	6.0
45	H1045	23	1763	8.7	16.5	3.51	128.1	6.5
50	H1050	20	2016	8.7	17.5	3.51	143.9	7.0
55	H1055	17	2380	8.7	17.9	3.51	159.7	7.5
60	H1060	15 [8]	2654	8.7	18.9	3.51	175.5	8.0
65	H1065	12 [8]	2943	8.7	19.9	3.51	191.3	8.5
70	H1070	10 [8]	3369	8.7	20.3	3.51	207.1	9.0
75	H1075	10 [8]	3672	8.7	21.3	3.51	222.9	9.5
80	H1080	9 [8]	3988	8.7	22.3	3.51	238.7	10.0
85	H1085	8 [8]	4487	8.7	22.7	3.51	254.5	10.5
90	H1090	7 [6]	4825	8.7	23.7	3.51	270.3	11.0
95	H1095	7 [6]	5177	8.7	24.7	3.51	286.1	11.5

CLASS H2

Length (Ft.)	Part No.	Full Truck Qty (2 Pcs.)	Stand. Weight (Lbs.)	Tip Dia. (In.)	Base Dia. (In.)	Allow. Tip Load (Kips)	Ground Line Capacity (Kip-Ft.)	ANSI Embed Depth (Ft.)
30	H2030	33	1200	8.7	14.2	4.16	93.6	5.5
35	H2035	28	1416	8.7	14.5	4.16	112.3	6.0
40	H2040	22	1777	8.7	15.5	4.16	133.1	6.0
45	H2045	19	2043	8.7	16.5	4.16	151.8	6.5
50	H2050	17	2328	8.7	17.5	4.16	170.6	7.0
55	H2055	14	2738	8.7	17.9	4.16	189.3	7.5
60	H2060	13 [8]	3047	8.7	18.9	4.16	208.0	8.0
65	H2065	10 [8]	3372	8.7	19.9	4.16	226.7	8.5
70	H2070	9 [8]	3864	8.7	20.3	4.16	245.4	9.0
75	H2075	8 [8]	4216	8.7	21.3	4.16	264.2	9.5
80	H2080	8 [8]	4583	8.7	22.3	4.16	282.9	10.0
85	H2085	7 [8]	5176	8.7	22.7	4.16	301.6	10.5
90	H2090	6 [6]	5579	8.7	23.7	4.16	320.3	11.0
95	H2095	6 [6]	6000	8.7	24.8	4.16	339.0	11.5

CLASS H3

Length (Ft.)	Part No.	Full Truck Qty (2 Pcs.)	Stand. Weight (Lbs.)	Tip Dia. (In.)	Base Dia. (In.)	Allow. Tip Load (Kips)	Ground Line Capacity (Kip-Ft.)	ANSI Embed Depth (Ft.)
30	H3030	30	1330	8.7	14.2	4.88	109.7	5.5
35	H3035	25	1570	8.7	14.5	4.88	131.6	6.0
40	H3040	20	1971	8.7	15.5	4.88	156.0	6.0
45	H3045	17	2267	8.7	16.5	4.88	177.9	6.5
50	H3050	15	2584	8.7	17.5	4.88	199.9	7.0
55	H3055	13	3039	8.7	17.9	4.88	221.8	7.5
60	H3060	12 [8]	3381	8.7	18.9	4.88	243.8	8.0
65	H3065	9 [8]	3743	8.7	19.9	4.88	265.7	8.5
70	H3070	8 [8]	4290	8.7	20.3	4.88	287.6	9.0
75	H3075	7 [8]	4680	8.7	21.3	4.88	309.6	9.5
80	H3080	7 [8]	5088	8.7	22.3	4.88	331.5	10.0
85	H3085	6 [8]	5734	8.7	22.7	4.88	353.4	10.5
90	H3090	5 [6]	6169	8.7	23.7	4.88	375.4	11.0
95	H3095	5 [6]	6624	8.7	24.8	4.88	397.3	11.5

CLASS H4

Length (Ft.)	Part No.	Full Truck Qty (2 Pcs.)	Stand. Weight (Lbs.)	Tip Dia. (In.)	Base Dia. (In.)	Allow. Tip Load (Kips)	Ground Line Capacity (Kip-Ft.)	ANSI Embed Depth (Ft.)
30	H4030	20	1506	11.4	16.9	5.66	127.2	5.5
35	H4035	20	1743	11.4	17.2	5.66	152.7	6.0
40	H4040	18	2210	11.4	18.2	5.66	181.0	6.0
45	H4045	16	2523	11.4	19.2	5.66	206.4	6.5
50	H4050	14	2855	11.4	20.3	5.66	231.9	7.0
55	H4055	12	3349	11.4	20.6	5.66	257.3	7.5
60	H4060	11 [8]	3704	11.4	21.7	5.66	282.8	8.0
65	H4065	9 [8]	4077	11.4	22.7	5.66	308.2	8.5
70	H4070	7 [6]	4674	11.4	23.1	5.66	333.6	9.0
75	H4075	7 [6]	5081	11.4	24.1	5.66	359.1	9.5
80	H4080	6 [6]	5506	11.4	25.1	5.66	384.5	10.0
85	H4085	5 [6]	6214	11.4	25.5	5.66	410.0	10.5
90	H4090	5 [6]	6676	11.4	26.5	5.66	435.4	11.0
95	H4095	5 [6]	7158	11.4	27.5	5.66	460.9	11.5

CLASS H5

Length (Ft.)	Part No.	Full Truck Qty (2 Pcs.)	Stand. Weight (Lbs.)	Tip Dia. (In.)	Base Dia. (In.)	Allow. Tip Load (Kips)	Ground Line Capacity (Kip-Ft.)	ANSI Embed Depth (Ft.)
30	H5030	20	1506	11.4	16.9	6.50	146.3	5.5
35	H5035	20	1743	11.4	17.2	6.50	175.5	6.0
40	H5040	18	2262	11.4	18.2	6.50	208.0	6.0
45	H5045	15	2609	11.4	19.2	6.50	237.3	6.5
50	H5050	13	2978	11.4	20.3	6.50	266.5	7.0
55	H5055	11	3527	11.4	20.6	6.50	295.8	7.5
60	H5060	10 [8]	3921	11.4	21.7	6.50	325.0	8.0
65	H5065	8 [8]	4335	11.4	22.7	6.50	354.3	8.5
70	H5070	7 [6]	5029	11.4	23.1	6.50	383.5	9.0
75	H5075	6 [6]	5501	11.4	24.1	6.50	412.8	9.5
80	H5080	6 [6]	5996	11.4	25.1	6.50	442.0	10.0
85	H5085	5 [6]	6817	11.4	25.5	6.50	471.3	10.5
90	H5090	5 [6]	7351	11.4	26.5	6.50	500.5	11.0
95	H5095	4 [5]	7909	11.4	27.5	6.50	529.8	11.5

CLASS H6

Length (Ft.)	Part No.	Full Truck Qty (2 Pcs.)	Stand. Weight (Lbs.)	Tip Dia. (In.)	Base Dia. (In.)	Allow. Tip Load (Kips)	Ground Line Capacity (Kip-Ft.)	ANSI Embed Depth (Ft.)
30	H6030	16	1616	14.0	19.5	7.41	166.7	5.5
35	H6035	16	1839	14.0	19.9	7.41	200.1	6.0
40	H6040	16	2419	14.0	20.9	7.41	237.1	6.0
45	H6045	14	2778	14.0	21.9	7.41	270.5	6.5
50	H6050	13	3097	14.0	22.3	7.41	303.8	7.0
55	H6055	10	3810	14.0	23.3	7.41	337.2	7.5
60	H6060	9 [6]	4254	14.0	24.3	7.41	370.5	8.0
65	H6065	7 [6]	4662	14.0	24.7	7.41	403.8	8.5
70	H6070	6 [6]	5426	14.0	25.7	7.41	437.2	9.0
75	H6075	6 [6]	5893	14.0	26.7	7.41	470.5	9.5
80	H6080	5 [6]	6387	14.0	27.1	7.41	503.9	10.0

CLASS H7 (8.39 KIPS)

Length (Ft.)	Part No.	Full Truck Qty (2 Pcs.)	Stand. Weight (Lbs.)	Tip Dia. (In.)	Base Dia. (In.)	Allow. Tip Load (Kips)	Ground Line Capacity (Kip-Ft.)	ANSI Embed Depth (Ft.)
30	H7030	16	1616	14.0	19.5	8.39	188.7	5.5
35	H7035	16	1839	14.0	19.9	8.39	226.4	6.0
40	H7040	16	2484	14.0	20.9	8.39	268.3	6.0
45	H7045	14	2883	14.0	21.9	8.39	306.1	6.5
50	H7050	12	3236	14.0	22.3	8.39	343.8	7.0
55	H7055	10	3949	14.0	23.3	8.39	381.5	7.5
60	H7060	9 [6]	4394	14.0	24.3	8.39	419.3	8.0
65	H7065	7 [6]	4802	14.0	24.7	8.39	457.0	8.5
70	H7070	6 [6]	5687	14.0	25.7	8.39	494.7	9.0
75	H7075	5 [6]	6227	14.0	26.7	8.39	532.4	9.5
80	H7080	5 [6]	6722	14.0	27.1	8.39	570.2	10.0

CLASS H8 (9.43 KIPS)

Length (Ft.)	Part No.	Full Truck Qty (2 Pcs.)	Stand. Weight (Lbs.)	Tip Dia. (In.)	Base Dia. (In.)	Allow. Tip Load (Kips)	Ground Line Capacity (Kip-Ft.)	ANSI Embed Depth (Ft.)
30	H8030	16	1711	14.0	19.5	9.43	212.1	5.5
35	H8035	16	1962	14.0	19.9	9.43	254.5	6.0
40	H8040	15	2655	14.0	20.9	9.43	301.6	6.0
45	H8045	13	3083	14.0	21.9	9.43	344.0	6.5
50	H8050	11	3464	14.0	22.3	9.43	386.4	7.0
55	H8055	9	4230	14.0	23.3	9.43	428.8	7.5
60	H8060	8 [6]	4708	14.0	24.3	9.43	471.3	8.0
65	H8065	7 [6]	5146	14.0	24.7	9.43	513.7	8.5
70	H8070	6 [6]	6032	14.0	25.7	9.43	556.1	9.0
75	H8075	5 [6]	6572	14.0	26.7	9.43	598.5	9.5
80	H8080	5 [6]	7066	14.0	27.1	9.43	640.9	10.0

CLASS H9 (10.53 KIPS)

Length (Ft.)	Part No.	Full Truck Qty (2 Pcs.)	Stand. Weight (Lbs.)	Tip Dia. (In.)	Base Dia. (In.)	Allow. Tip Load (Kips)	Ground Line Capacity (Kip-Ft.)	ANSI Embed Depth (Ft.)
30	H9030	16	2004	16.5	22.1	10.53	236.9	5.5
35	H9035	16	2265	16.5	22.4	10.53	284.3	6.0
40	H9040	13	3046	16.5	23.5	10.53	337.0	6.0
45	H9045	11	3493	16.5	24.5	10.53	384.3	6.5
50	H9050	9	4373	16.5	24.9	10.53	431.7	7.0
55	H9055	9	4530	16.5	25.9	10.53	479.1	7.5
60	H9060	8 [6]	5008	16.5	26.9	10.53	526.5	8.0
65	H9065	6 [6]	5492	16.5	27.6	10.53	573.9	8.5

7 VITA

Ramani Ayakannu received his B. Tech (Civil Engineering) degree from the National Institute of technology, Warangal, Andhra Pradesh, India 1983. He was a Civil Engineering lecturer at the Federal Institute of Technology, Kuala Lumpur, Malaysia. He lectured in Structural Steel Design, Reinforced Concrete Design, Structural Analysis, and engineering mathematics. He graduated from the South Dakota School of Mines and Technology, Rapid City, South Dakota 1988. He worked as a structural engineer on many projects, including schools, low and medium-rise buildings, parking garages, airplane hangars, garbage treatment plants, industrial projects, and electrical substations. He has also worked on many precast concrete buildings and parking structures. Ramani Ayakannu served in the IEEE 693 Recommended Practice for Seismic Design of Substation Structures. He has performed seismic qualification of Electrical equipment and support structures in Substations. He began his Ph.D. program in Spring 2015, majoring in structural engineering. This dissertation, titled DYNAMIC SOIL-STRUCTURE RESPONSE AND FAILURE OF WOOD UTILITY POLES UNDER HURRICANE-FORCE WIND AND NON-LINEAR CABLE LOADS, was completed in May 2024.

The author's current address is:

104 Olde State House Drive
Morrisville, NC 27560
Phone: 919-600-2587
Email: ramani.ayakannu@gmail.com